

EXPERIMENTAL
AND THEORETICAL
INVESTIGATION OF THE
ELECTRONIC STRUCTURES OF
FERROCENE-PEPTIDE
CONJUGATES

A Thesis Submitted to the College of
Graduate Studies and Research
In Partial Fulfillment of the Requirements
For the Master of Science
In the Department of Physics and Engineering Physics
University of Saskatchewan
Saskatoon

By

REGAN G. WILKS

Keywords: XAS, XES, absorption spectroscopy, emission spectroscopy, ferrocene, proline, peptide, electronic structure, density functional theory

© Copyright Regan George Wilks, July 2005. All rights reserved.

702001721855

PERMISSION TO USE

In presenting this thesis in partial fulfilment of the requirements for a Postgraduate degree from the University of Saskatchewan, I agree that the Libraries of this University may make it freely available for inspection. I further agree that permission for copying of this thesis in any manner, in whole or in part, for scholarly purposes may be granted by Dr. Alexander Moewes or, in his absence, by the Head of the Department or the Dean of the College in which my thesis work was done. It is understood that any copying, publication, or use of this thesis or parts thereof for financial gain shall not be allowed without my written permission. It is also understood that due recognition shall be given to me and to the University of Saskatchewan in any scholarly use which may be made of any material in my thesis.

Requests for permission to copy or to make other use of material in this thesis in whole or part should be addressed to:

Head of the Department of Physics and Engineering Physics
University of Saskatchewan
Saskatoon, Saskatchewan
S7N 5E2

ABSTRACT

A combined experimental and theoretical examination of the electronic structures of a number of modified helical peptides, specifically ferrocene-(proline)_x-benzyl ester (referred to as Fc-Pro_x-OBz), is presented. Soft X-ray absorption (XAS) and emission (XES) spectroscopy using synchrotron radiation are used to probe the unoccupied and occupied partial densities of electronic states, respectively. The identities of the final-state orbitals corresponding to all near-edge features in the XAS spectra of all elements in the molecules are determined by comparison with published results for other systems, as well as density functional theory (DFT) spectral simulations. Experimental evidence of the splitting of the Fc 3e_{2u} orbital due to the presence of a substituent is observed for the first time. The 3e_{2u} orbital is also found to contribute to a delocalized orbital that extends throughout the peptide, suggesting a possible electron transfer pathway. Analysis of the Fe 2p XAS spectrum leads to the reassignment of the origin of the prominent 711.4 eV resonance to transitions into hybridized orbitals involving Fe 4s levels and the σ* orbitals associated with the Fc C-H bonds. Previous studies incorrectly described this feature.

Comparison of the DFT-simulated ground-state DOS of Fc-Pro₂-OBz and Fc-Pro₃-OBz shows a major reorganization of the orbitals of the benzyl ester, which acts as the reduction centre in redox reactions. In Fc-Pro₃-OBz, the orbitals closely resemble those of a gaseous substituted benzene ring and were found at a lower energy than the equivalent orbitals of Fc-Pro₂-OBz. This shift is proposed as a possible explanation for the decrease in redox potential observed upon the addition of a third proline residue to the peptide.

ACKNOWLEDGEMENTS

The author gratefully acknowledges the guidance and support provided to him by Dr. Alexander Moewes, along with the other members of the 'Beamteam' research group. The contribution of the committee members is also greatly appreciated. This project was supported by funding from the National Science and Research Council (NSERC), and by the Saskatchewan Synchrotron Institute (SSI). A. Moewes is a Canada Research Chair. The Advanced Light Source at Lawrence Berkeley National Laboratory is supported by the U.S. Department of Energy (Contract No. DE-AC03-76SF00098).

TABLE OF CONTENTS

PERMISSION TO USE	i
ABSTRACT	ii
ACKNOWLEDGEMENTS	iii
LIST OF TABLES	vii
LIST OF FIGURES	viii
LIST OF ABBREVIATIONS	xii
1. INTRODUCTION	1
2. SYNCHROTRON LIGHT SOURCES.....	3
2.1. Bending Magnets	4
2.2. Undulator Insertion Devices.....	5
3. BEAMLINES.....	7
3.1. Beamline 8.0.1	7
3.1.1. The Monochromator.....	8
3.1.2. Focusing and Flux Measurement	10
3.1.3. Soft X-ray Fluorescence Endstation.....	10
3.2. Beamline 6.3.2.....	11
4. SOFT X-RAY SPECTROSCOPY	13
4.1. X-ray Absorption Spectroscopy (XAS)	17
4.1.1. Total Electron Yield (TEY)	19
4.1.2. Fluorescence Yield Measurements.....	20
4.2. X-ray Emission Spectroscopy (XES).....	24
5. DENSITY FUNCTIONAL THEORY	25
5.1. The Hohenberg-Kohn Theorems	26
5.2. The Kohn-Sham Method.....	29
5.2.1. The Universal Functional	30

5.2.2. The Kohn-Sham Equations.....	31
5.3. The Exchange Interaction.....	33
5.3.1. Origin of the Exchange Interaction.....	33
5.3.2. Approximations of the Exchange Interaction.....	36
5.4. Using the Kohn-Sham Framework.....	38
5.5. XAS Calculations.....	44
5.5.1. Parameters Used in Calculations.....	45
6. FERROCENE-PEPTIDE CONJUGATES.....	48
7. SAMPLE PREPARATION.....	52
8. CALIBRATION AND NORMALIZATION.....	53
9. EXPERIMENTAL AND THEORETICAL XAS SPECTRA.....	56
9.1. C 1s XAS Spectra.....	56
9.1.1. Experimental C 1s XAS Spectra.....	57
9.1.2. StoBe C 1s XAS Spectra.....	65
9.2. O 1s XAS Spectra.....	79
9.2.1. Experimental O 1s XAS Spectra.....	80
9.2.2. StoBe O1s XAS spectra.....	83
9.3. N 1s XAS.....	86
9.3.1. Experimental N 1s XAS Spectra.....	86
9.3.2. StoBe N 1s XAS Spectra.....	88
9.4. Fe 2p XAS.....	90
9.5. Radiation Damage.....	98
10. XES AND RIXS SPECTRA.....	101
10.1. C K_{α} Emission.....	101
11. DENSITY OF STATES CALCULATIONS.....	105
11.1. Fc-Pro ₂ -OBz Density of States.....	106
11.2. Fc-Pro ₃ -OBz Density of States.....	112
12. SUMMARY AND CONCLUSIONS.....	118
12.1. Conclusions from the Experimental XAS Spectra.....	118
12.2. Conclusions from the Calculated XAS Spectra.....	120
12.3. Conclusions from DOS Calculations.....	121

12.4. Summary	123
REFERENCES	124
APPENDIX B: Site-Resolved StoBe C 1s XAS of Fc-Pro ₂ -OBz	139
APPENDIX C: Term Values of StoBe C 1s XAS Features.....	140
APPENDIX D: Fc-Pro ₁ -OBz and Fc-COOH C K _α RIXS	142
APPENDIX E: Spartan Representations of Molecular Orbitals.....	143
APPENDIX F: Summary of Previous Studies	145

LIST OF TABLES

Table 4.1: Notations used in X-ray spectroscopy to describe core levels.....	14
Table 8.1: Calibration samples for soft X-ray absorption (XAS) and emission (XES) spectroscopy. Energy values correspond to the position of prominent features in the reference spectra.....	53
Table 9.1: Energy positions and term values for features in C 1s spectra of ferrocene sites.....	70
Table 9.2: Energy positions and term values for features in C 1s spectra of the benzyl ester sites.....	76
Table 9.3: Transitions in the calculated Fe 2p XAS spectra of Fc-Pro ₂ -OBz.....	95
Table A.1 Site-resolved term values for ferrocene C 1s XAS.....	140
Table A.2 Site-resolved term values for benzene C 1s XAS	141
Table A.3 Overview of previous XAS and XES studies of amino acids.....	145

LIST OF FIGURES

Figure 3.1 Schematic representation of Beamline 8.0 at ALS synchrotron at Lawrence Berkeley National Lab.....	7
Figure 3.2 Relative photon flux of all three monochromator gratings at Beamline 8.0 for 1st and 3rd undulator harmonics.....	8
Figure 3.3 Argon 2p-4s resonant emission measured at SXF endstation at Beamline 8.0.1, demonstrating $E/\Delta E$ value of 6120.....	9
Figure 3.4 Schematic diagram of the SXF endstation at Beamline 8.0.1, excluding channeltron and adjustable entrance slit.....	10
Figure 3.5 Schematic representation of Beamline 6.3.2 at the ALS, including reflectance endstation.....	12
Figure 4.1 Schematic representation of the radiative transitions involved in XAS (left) and XES (right).....	13
Figure 4.2 The fluorescence yields of the K and L shells plotted as a function of atomic number.....	16
Figure 4.3 C 1s XAS spectrum of C ₆₀ , with the approximate shape and position of the photoionization step function shown (dotted line). The spectrum was measured at Beamline 8.0.1 of the ALS synchrotron.....	18
Figure 4.4 The inverse of the attenuation length of photons in carbon for the energy range encompassing to the energy region monitored in C 1s XAS spectra. The attenuation length is inversely proportional to the photoabsorption.....	21
Figure 6.1 The molecular structure of ferrocene (Cp-Fe-Cp, Fe(C ₅ H ₅) ₂). The Fe atom is located at the "waist" of the molecule, and is bonded to the two Cp ligands.....	48
Figure 6.2. The structures of three amino acid monomers. Hydrogen atoms are omitted for clarity.....	49
Figure 6.3. Ortep drawing of the molecular structure of Fc-Pro ₂ -OBz with the component groups labeled. The oxygen and nitrogen sites are also labeled.....	50
Figure 8.1. Calibrated (solid) and uncalibrated (dashed) N 1s XAS spectra of reference sample hBN.....	54

Figure 8.2. Calibrated (solid) and uncalibrated (dashed) N K_{α} XES spectra of reference sample hBN.....	54
Figure 9.1. The C 1s XAS spectrum of Fc-Pro ₁ -OBz measured at Beamline 6.3.2 at the ALS. The important spectral features that are discussed in the text are labeled. The region marked "C=O" represents the energy range (287.5 eV - 288.6 eV) of the carbonyl resonance features in the spectra of the Fc-Pro _x -OBz series.	57
Figure 9.2. Close-up of the C 1s XAS spectra of Fc-Pro ₃ -OBz (top) and Fc-Pro ₁ -OBz (bottom). The positions of the significant features of each spectrum are marked with arrows; the dotted lines have been added to aid in the comparison of the spectra. The inset shows the spectrum of Fc-Pro ₁ -OBz with a box around the energy region that is shown in the main figure.	59
Figure 9.3. Comparison of the C 1s XAS spectra of Fc-Pro ₁ -OBz (top) and Fc-COOH (bottom) measured at Beamline 6.3.2 at the ALS. Spectra have had background subtracted and have been offset vertically for clarity.	62
Figure 9.4. The C 1s XAS spectra of Fc-COOH and Fc-(COOH) ₂	63
Figure 9.5. The C 1s XAS spectra of Fc-Pro _x -OBz (x= 1 - 4) measured at Beamline 6.3.2 at the ALS. Spectra have had background subtracted and have been offset vertically for clarity.	64
Figure 9.6. C 1s XAS spectra of Fc-(glu)-(OH) ₂ and Fc-(glu)-(glu) ₂ -(glu) ₄ -(OH) ₈	64
Figure 9.7. The structure of Fc-Pro ₂ -OBz, showing the labeling scheme used to identify the carbon sites.	66
Figure 9.8. C 1s XAS spectra of the ferrocene sites in Fc-Pro ₂ -OBz as calculated using StoBe. A vertical offset is added for clarity.	67
Figure 9.9. C 1s XAS spectra of the proline residues of Fc-Pro ₂ -OBz, calculated using StoBe. The upper window shows the spectra associated with the proline nearest the ferrocene moiety, while the lower window shows the adjacent proline. Spectra have not been normalized, and an offset has been added for clarity.	72
Figure 9.10. C 1s XAS spectra of the benzyl ester sites in Fc-Pro ₂ -OBz as calculated using StoBe. Vertical offset is added for clarity.	75
Figure 9.11. Experimental C 1s XAS spectrum of Fc-Pro ₂ -OBz (top) and DFT simulated spectrum (bottom). Intensity has been normalized at 285.4 eV, and a vertical offset has been added for clarity.	77
Figure 9.12. Oxygen 1s XAS of the series Fc-Pro _x -OBz (x=1-4). The energy values of the most significant transitions are marked.	80

Figure 9.13 The O 1s XAS spectra associated with the four oxygen sites in Fc-Pro ₂ -OBz, as calculated using StoBe. The sites are numbered according to their distance from the ferrocene moiety, as illustrated in the inset. The energy axes of all spectra were shifted by -0.3 eV to better correspond to the experimental data.	83
Figure 9.14 Theoretical O 1s XAS spectrum of Fc-Pro ₂ -OBz produced by weighted sum of StoBe spectra of individual sites, compared with the measured spectrum.	85
Figure 9.15. Nitrogen 1s XAS of the series Fc-Pro _x -OBz (x= 1-4) measured at Beamline 6.3.2 at the ALS. Spectra have had background subtracted, and a vertical offset has been added for clarity.	87
Figure 9.16 The StoBe simulations of the N 1s XAS spectra of both nitrogen sites in Fc-Pro ₂ -OBz, as well as the spectrum measured at Beamline 6.3.2 of the ALS.	88
Figure 9.17 Sum of the spectral contributions calculated by StoBe for both nitrogen sites in Fc-Pro ₂ -OBz (bottom) compared to the measured spectrum (top). The unbroadened contributions are displayed along the bottom of the plot.	90
Figure 9.18. The Fe 2p XAS spectra of Fc-COOH and Fc-Pro _x -OBz (x=1-4) measured at Beamline 6.3.2 at the ALS. All spectra have had background subtracted and have been offset for clarity.	91
Figure 9.19. The Fe 2p XAS spectrum of Fc-COOH, measured at Beamline 6.3.2. The energies of the notable transitions are marked on the 2p _{3/2} absorption feature.	92
Figure 9.20. The uncalibrated Fe 2p XAS spectra of Fc-Pro ₂ -OBz, as calculated by StoBe. The spectrum associated with each 2p orbital is numbered with a subscript to avoid confusion with the numbering scheme used for nonequivalent sites in previous figures.	94
Figure 9.21. Fe 2p XAS spectrum of Fc-COOH compared to spectrum predicted by DFT.	97
Figure 9.22. The C 1s XAS spectra of Fc-Pro ₁ -OBz before (solid line) and after (dashed line) exposure to high-intensity soft X-rays, showing the effects of radiation damage. Both spectra were measured at Beamline 8.0.1 at the ALS.	99
Figure 9.23. The C 1s XAS spectrum of Fc-Pro ₁ -OBz measured with increasing (top) and decreasing (bottom) excitation energy at Beamline 6.3.2. A small vertical offset is added to differentiate the spectra.	100
Figure 10.1. The C K α RIXS spectra of Fc-Pro ₁ -OBz (upper panel). The excitation energy for each spectrum is shown to the right of the main resonance, and the location of each excitation energy is indicated by an arrow on the XAS spectrum (lower panel).	102

Figure 10.2. C K α RIXS spectra of Fc-Pro ₁ -OBz and Fc-COOH. The bottom spectrum is the difference between the two normalized spectra.....	103
Figure 11.1. The site-resolved carbon density of unoccupied states of Fc-Pro ₂ -OBz, calculated using StoBe. Each plot represents the contribution of an individual atom to the overall DOS, and the sites are arranged according to their position in the molecule.	106
Figure 11.2. The LUMO of Fc-Pro ₂ -OBz as calculated by Spartan (bottom). The wireframe structure of the molecule is shown above as a reference.	107
Figure 11.3. The unoccupied DOS of Fc-Pro ₂ -OBz, calculated using StoBe. All components are displayed separately, and the plots are arranged according to their corresponding position on the molecule. A vertical offset is added for clarity. ..	109
Figure 11.4. The <i>s</i> and <i>d</i> contributions to the Fe density of states of Fc-Pro ₂ -OBz, calculated using StoBe.....	110
Figure 11.5. The contributions of the individual 3d orbitals to the unoccupied Fc-Pro ₂ -OBz DOS, as calculated using StoBe. The region from -0.6 eV to 0.1 eV is magnified 100 times, and a vertical offset is added for clarity.	111
Figure 11.6. The C-H σ^* orbitals of Fc-Pro ₂ -OBz as calculated using Spartan. The numbering system is a reference to the number of orbitals between the one in question and the LUMO (i.e. LUMO +7 is the eighth unoccupied orbital).	112
Figure 11.7. The component-resolved unoccupied DOS of Fc-Pro ₃ -OBz, as calculated using StoBe. Plots are arranged according to their location in the molecule, and a vertical offset is added for clarity.....	113
Figure 11.8. The unoccupied DOS of the benzyl ester sites in Fc-Pro ₃ -OBz as calculated using StoBe. The position of each site in the molecule is labeled on the inset, and a vertical offset is added.	114
Figure 11.9. The LUMO and LUMO+1 orbitals of Fc-Pro ₃ -OBz calculated using Spartan.	115
Figure A.1 Site-resolved StoBe C 1s XAS of Fc-Pro ₂ -OBz	139
Figure A.2 Comparison of the C K α RIXS spectra of Fc-Pro ₁ -OBz and Fc-COOH....	142
Figure A.3 A 3e _{2u} orbital of gaseous ferrocene	143
Figure A.4 The LUMO and LUMO+1 orbitals of toluene.....	144

LIST OF ABBREVIATIONS

ALS	Advanced Light Source
RF	Radio Frequency
REIXS	Resonant inelastic X-ray scattering
UHV	Ultra-high vacuum
MCP	Multi-channel plate
XAS	X-ray absorption spectroscopy
NEXAFS	Near-edge X-ray absorption fine-structure
XES	X-ray emission spectroscopy
RIXS	Resonant inelastic X-ray scattering
TEY	Total electron yield
TFY	Total fluorescence yield
PFY	Partial fluorescence yield
DOS	Density of states
PDOS	Partial density of states
DFT	Density functional theory
SCF	Self-consistent field
DZVP	Double-zeta with valence polarization
TZVP	Triple-zeta with valence polarization
DIIS	Direct inversion of iterative subspace
Fc	Ferrocene
Cp	cyclopentadienyl
COOH	Carboxylic acid
Gly	Glycine
Pro	Proline
Glu	Glutamic acid
OBz	Benzyl ester
CV	Cyclic voltammetry
Redox	reduction-oxidation

EELS	Electron energy loss spectroscopy
MO	Molecular orbital
EXAFS	Extended X-ray absorption fine structure

1. INTRODUCTION

Electron transfer in peptides is known to be involved in a variety of biological processes, including photosynthesis,¹ and may also have implications in the field of molecular electronics. The mechanism that allows this important process to occur is, however, poorly understood. The goal of this study is to increase the understanding of electron transfer by modelling the electronic structures of peptides that have been modified by the attachment of electroactive structures. These structures consist of an electron-donating molecule attached to one end of the peptide and an electron-accepting molecule to the other end.²⁻⁷ The peptides were conceived and are prepared in the Department of Chemistry at the U of S, and have been found to display unusual electronic behaviour. It has been shown that, in certain types of samples, it becomes easier to transfer an electron from one end to the other as the size of the peptide increases,⁴ contrary to the inverse relationship that would be expected. If the source of this unusual behaviour can be understood, it will lead to a better understanding of electron transfer in organic materials in general. This multi-disciplinary study requires an understanding of chemistry, biochemistry, and, of course, physics, and is the most ambitious site-selective spectroscopic study of peptidic materials ever performed. Few previous studies have provided both an experimental and a theoretical examination of the peptide's electronic structure, and none have examined modified peptides.

Soft X-ray spectroscopy using synchrotron radiation is employed in this study to probe the electronic structure of the molecules. This sort of analysis provides a site- and element-specific representation of the valence and low-energy unoccupied orbitals of the materials, states that have a key role in many electronic properties. The measured spectra are supplemented by theoretical models based on density functional theory calculations. These calculations aid in the analysis of the experimental data and provide a wealth of information that cannot be obtained experimentally.

The following sections describe all aspects of the project, beginning with a basic description of synchrotron light sources (Section 2) and the experimental facilities that were used in the data collection (Section 3). Next, a detailed description of soft X-ray spectroscopic techniques will be included (Section 4), providing the background information that is needed to interpret the experimental results. To the same end, a summary of the origin and development of density functional theory, including specific details of the program and parameters that are employed in this study, will be presented (Section 5).

Once the techniques and facilities have been discussed, the specific details of the project will be presented. The structures and behaviour of the materials that were described at the beginning of this section will be discussed in detail (Section 6), followed by brief descriptions of the preparation of the samples for measurement (Section 7) and the techniques that are used to calibrate and normalize the experimental data (Section 8).

The next section (Section 9) is by far the largest and most comprehensive, presenting and analyzing the experimental and calculated X-ray absorption spectra all elements in the molecules. Section 9 contains the bulk of the analysis, and will be followed by a discussion of the complementary soft X-ray emission spectra of the molecules (Section 10).

The last major section (Section 11) describes the results of the density of states calculations that were performed in this study. These theoretical models of the electronic structure of the modified peptides provide both confirmation of the conclusions drawn in the earlier sections, as well as suggesting a possible explanation for the unusual behaviour of the modified peptides. The data presented in this section represent the final stage of this study of electroactive organic materials, and it is followed by a brief summary of the results of each section of the analysis.

2. SYNCHROTRON LIGHT SOURCES

Third-generation synchrotron facilities provide extremely brilliant light that can be applied in a large number of materials research techniques. Synchrotron radiation is produced when the path of electrons traveling at nearly the speed of light is bent by a magnetic field. The resulting photons that are produced in the synchrotron travel in the direction of the electron beam, with little deviation. Synchrotron radiation is emitted in a continuous spectrum, which has helped to develop a number of techniques that make use of light in energy regions where low intensity has traditionally been a hindrance. The following section describes the general nature of the synchrotron and synchrotron radiation.

The primary driving force behind synchrotrons such as the Canadian Light Source (CLS) and the Advanced Light Source (ALS) at the Lawrence Berkeley National Laboratory is a linear electron accelerator (linac). In this device, electrons that are emitted by a cathode are initially accelerated due to the action of a large electric potential difference. The electrons are then bombarded with bursts of microwave radiation, which causes them to gain energy and also to bunch together in a manner related to the radiation frequency. These bunches of energetic electrons are then ejected into the booster ring of the synchrotron.

The main difference between the linear accelerator and the booster ring is geometric, rather than functional. As in the linac, the electrons in the booster ring are accelerated by tuned microwave radiation. The circular structure of the booster ring has the advantage that the electrons pass through the RF cavity every time they complete a circuit of the ring, rather than only once in the linac. As a result, the booster ring can impart an extremely large amount of energy to the circulating electrons. When the electron bunches have achieved the target energy (approximately 1.9 GeV at the ALS),

they are ejected into the storage ring, where they will circulate for several hours and can be used to perform scientific experiments.

While in the storage ring, the energy of the electrons is maintained by an additional RF system, and their path is manipulated by bending magnets and insertion devices. Bending magnets serve the twofold purpose of directing the electron beam along the path of the ring and, in doing so, producing synchrotron light that can be used for experiments. Insertion devices are found in the straight sections of the storage ring, and produce high intensity light as the electron beam passes through the device and continues along its initial trajectory.

2.1. Bending Magnets

Bending magnets, such as the one that supplies synchrotron radiation to Beamline 6.3.2 at the ALS, cause the electrons in the storage ring to emit a broad spectrum of intense radiation. Because of the relativistic energy of the electrons in the storage ring, the radiation that is emitted when they are accelerated by the magnetic field is contained in a tight cone around the direction of propagation of the electrons.⁸ Because the electrons are changing direction, the radiation cone changes direction accordingly, and the light is scanned across a broad horizontal range. Some of the radiation will enter the beamline, where it must then be monochromatized so that it can be used for experiments.

The electrons that pass through a bending magnet must follow a specific path if they are to continue into the next section of the storage ring. Accordingly, the field of the bending magnet must remain constant, because the electrons are kept at a constant energy by the RF system. Since all of the system-related parameters are constant, the radiation that is produced in the bending magnet is characteristic of that particular environment.

As was mentioned previously, the energy range of the light that is emitted by a bending magnet is very large, and so a quantity called the critical photon energy (E_c) must be defined so that the dependence of the emitted spectrum on the various system

parameters can be described. The critical photon energy is defined as the midpoint in the curve describing the intensity of the light as a function of its energy. At the point E_c , half of the total emitted energy is transmitted as photons having energy less than E_c , and half as higher-energy photons.⁸ Attwood, among others, showed that this energy is given by the equation

$$E_c = \frac{3e\hbar B\gamma^2}{2m} \quad (2.1)$$

where B is the magnetic field, m is the mass of an electron, and γ is the Lorentz factor describing the electron bunches as observed in the laboratory frame. The constants can be collected, and the Eq. 2.1 can be rewritten in terms of the energy of the electrons and the magnitude of the applied magnetic field, yielding an expression for the critical energy in keV.

$$E_c(\text{keV}) = 0.6650E_e^2(\text{GeV})B(T) \quad (2.2)$$

As is shown by Eq. 2.2, the radiation of the bending magnet is fairly simple to describe once the parameters of the beam and storage ring are set. The description of undulator radiation, however, is more complicated.

2.2. Undulator Insertion Devices

The insertion device that produces the light used at BL 8.0.1 is an undulator, which produces light with a much higher brightness ($\sim 10^{19}$ photons/(s)(mm²)(mrad²)(0.1% BW)) than a bending magnet ($\sim 10^{15}$). The undulator is an array of electromagnets that are oriented such that the electrons passing through the device experience a periodically alternating magnetic field. The magnetic field causes the electrons to oscillate sinusoidally about their mean direction of propagation, emitting radiation as a result of this acceleration. As in the bending magnet, the emitted radiation is contained in a tight cone directed tangent to the path of the beam. Unlike the bending magnet, the geometry of the undulator allows the intensity of the light produced during each period of

oscillation to be additive, because there will be two points in each period where the electrons, and therefore the radiation cone, will be traveling parallel to their mean direction of propagation.

An undulator will produce a broad spectrum of radiation, although certain characteristics of the undulator can be adjusted to maximize amount of radiation that is emitted around a certain energy. Equation 2.3 shows how the wavelength corresponding to the maximum intensity of radiation is affected by the parameters of the undulator and the electron bunches.⁸ The equation can easily be rearranged to express the energy of the photons, rather than their wavelength, but the effect of changes in the parameters is more difficult to intuit in that form.

$$\lambda_n = \frac{\lambda_U}{2\gamma^2 n} \left(1 + \frac{B_0^2 K^2}{2} + \gamma^2 \theta^2 \right) \quad (2.3)$$

In this equation, λ_n is the wavelength of the n^{th} harmonic, λ_U is the natural wavelength of the undulator, γ is the Lorentz factor, θ is the angle of observation measured from the axis of the light's propagation, and B_0 is the magnitude of the magnetic field of an undulator magnet. The factor K is a constant for a given undulator, and is defined as $K \equiv \frac{e\lambda_U}{2\pi mc}$ where e and m are the charge and mass of an electron, respectively, and c has its usual meaning as the speed of light.

The value of the above expression is dominated by the first two terms, while the third term accounts for off-axis variations in the central wavelength. The factors that most greatly affect the emitted radiation, the natural frequency of the undulator and the magnetic field within it, are described by the first and second terms in Eq. 2.3, respectively. Because it is not practical to change the undulator wavelength, tuning of the radiation wavelength is performed by adjusting the magnetic field. The magnetic field is adjusted by changing the size of the gap between the magnets; the smaller the gap, the higher the magnetic field will be. Of course, the presence of the Lorentz factor in the equation means that the wavelength could also be tuned by changing the velocity of the electrons in the storage ring, but this procedure would be both impractical and inefficient.

3. BEAMLINES

The experimental data included in this study were measured at two different beamlines at the ALS synchrotron. The following sections will outline the basic components and operation of Beamlines 8.0.1 and 6.3.2. Emphasis will be placed on the discussion of Beamline 8.0.1, as our group primarily uses that facility and it is somewhat similar to the REIXS beamline that will be a key component of the CLS synchrotron. The discussion of Beamline 6.3.2 will be significantly shorter, but much of what is written about the former beamline is also true for the latter.

3.1. Beamline 8.0.1

A schematic representation of Beamline 8.0.1⁹ is shown in Figure 3.1. The light that is produced by the undulator is collimated, monochromatized, and focused before it reaches the endstation. The water-cooled vertical condensing mirror, which is the first optical device that the undulator radiation encounters upon entering the beamline, is used to direct the largest possible amount of the radiation through the adjustable entrance slit, thus increasing the intensity of the radiation that passes into the monochromator. Interchangeable rotatable spherical gratings are used to monochromatize the radiation. A horizontal re-focusing mirror is used to focus the radiation onto the endstation. The endstation consists of a horizontal re-focusing mirror, a translatable exit slit, and a horizontal & vertical ellipsoidal re-focusing mirror. The endstation is used for experiments such as SXF and EMA.

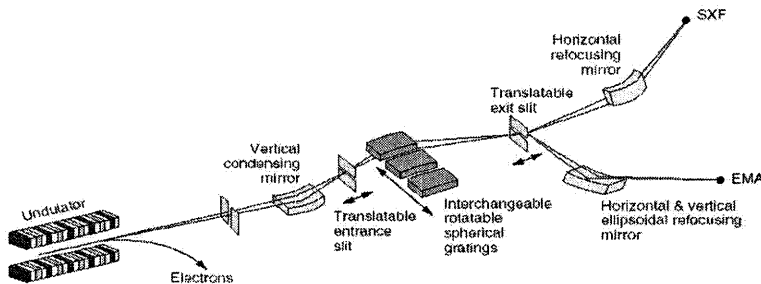


Figure 3.1 Schematic representation of Beamline 8.0 at ALS synchrotron at Lawrence Berkeley National Lab.

3.1.1. The Monochromator

Once the radiation passes through the entrance slit, it is incident upon one of three interchangeable spherical gratings. It is these gratings that allow the radiation to be tuned to a desired energy. All three have a radius of curvature of 70 m, and the low-, medium- and high-energy gratings have rulings of 150 lines/mm, 380 lines/mm, and 925 lines/mm, respectively. The gratings are mounted parallel to each other so that an individual grating can be selected by simply moving the mounting apparatus along a path perpendicular to the beamline's axis. Energy selection is accomplished by rotating the grating to such a position that the desired energy passes through the exit slit. The sizes of both the entrance and exit slits, along with the position of the latter, are adjustable and can be manipulated to provide a balance of flux and resolution that is appropriate for the experiment.

Figure 3.2 shows the relationship between the desired photon energy and the available flux for all three gratings. This figure is available on the ALS website.¹⁰ The focusing of the X-rays is optimized when the diffraction grating, entrance slit, and exit slit are positioned such that they satisfy the Rowland Geometry, which stipulates that all three elements lie on a circle with a radius equal to one-half of the radius of curvature of the grating.

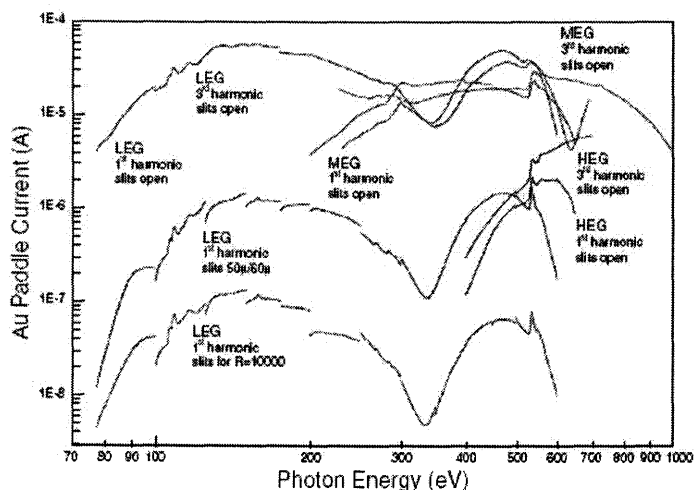


Figure 3.2 Relative photon flux of all three monochromator gratings at Beamline 8.0 for 1st and 3rd undulator harmonics

The resolving power of the monochromator energy is commonly expressed as an $E/\Delta E$ value, where E is the desired photon energy, and ΔE is the bandwidth of the energy passing through the monochromator. Put another way, when the monochromator is used to select a specific photon energy from the broad spectrum produced by the undulator, the light that actually passes through it has an energy in the range $E \pm \frac{1}{2}\Delta E$. The energy resolution is strongly related to the size of the entrance and exit slits and is also dependent on the location of the desired energy region. In general, as the photon energy increases the sizes of the slits must be decreased in order to achieve a high resolution. This tendency limits the amount of flux that is available at higher energies, and so it is important to find an acceptable balance between resolution and flux. In the past, resolving powers of up to 6000 have been measured at this beamline.

Figure 3.3 was taken from the ALS website,¹⁰ and shows a curve, composed of a superposition of Gaussian and Lorentzian functions, which has been fit to an experimental argon 2p-4s resonant absorption feature. The Lorentzian function accounts for the broadening due to the lifetime of the excited state, while the Gaussian accounts for the instrumental broadening. The instrumental broadening can be assumed to be equal to the energy resolution of the monochromator, and so the Gaussian broadening suggests a ΔE value of approximately 40.1 meV ($E/\Delta E > 6000$). The difference between the measured curve and the fit is described by the nearly flat line at the bottom of the spectrum figure.

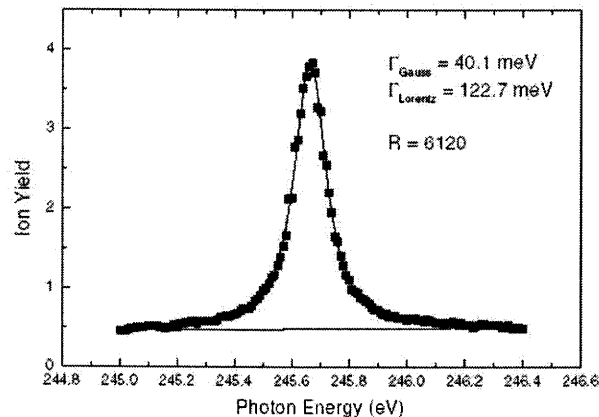


Figure 3.3 Argon 2p-4s resonant emission measured at SXF endstation at Beamline 8.0.1, demonstrating $E/\Delta E$ value of 6120.

3.1.2. Focusing and Flux Measurement

Before the photons from the monochromator reach the experimental endstation, they are first reflected from a horizontal mirror, which allows the beam to be both focused and positioned in the horizontal plane, and then must pass through a highly transparent gold mesh. The majority of the photons that are incident on the mesh pass through unimpeded, but a certain amount of them cause free electrons to be ejected from the mesh, causing a net positive current to flow from the mesh. The current provides a measure of the number of photons entering the sample chamber, a parameter that needs to be known in order to normalize both XAS and XES measurements.

3.1.3. Soft X-ray Fluorescence Endstation

Figure 3.4 shows the schematic layout of the soft X-ray fluorescence endstation at Beamline 8.0.1. Figure 3.4 does not show the recently added channeltron detector and variable-aperture spectrometer entrance slit.

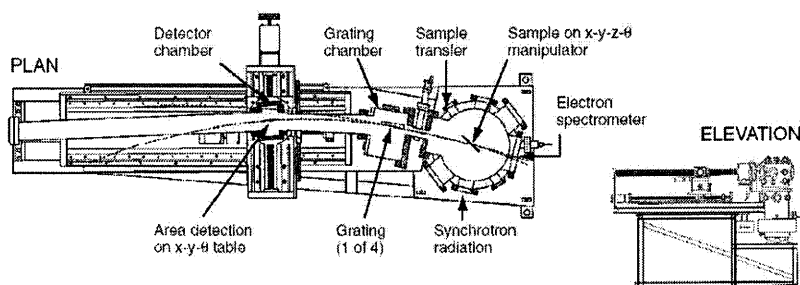


Figure 3.4 Schematic diagram of the SXF endstation at Beamline 8.0.1, excluding channeltron and adjustable entrance slit

The entirety of the sample chamber and spectrometer area is kept under UHV conditions. The fluorescence photons pass through the spectrometer entrance slit, striking one of four selectable gratings, which serve to separate the photons according to energy. Having different energies, photons created through different processes are diffracted different amounts, and so the area-sensitive detector can produce a detailed, energy-resolved picture of the fluorescence emission. Like the monochromator and its

entrance and exit slits, the detector, gratings, and spectrometer entrance slit are positioned according to Rowland geometry in order to optimize focusing.

The photon-counting area detector consists of a stacked array of three multi-channel plates (MCP). The MCPs consist of a number of silicon channels that are biased in such a way that they generate an electron cascade when struck by a photon. Incoming fluorescence photons pass through a gold mesh and produce a free electron when they come into contact with one of the channel walls. The gold mesh carries a negative voltage with respect to the MCP; this biasing acts as a retarding potential, forcing the ejected electrons back onto the MCP. The front of the MCP has a strong negative bias with respect to the back of the array, which causes the free electrons to be accelerated toward the positive end, producing a cascade of electrons along the way. Signal gains on the order of 10^6 are typical of this arrangement.¹¹ The electron pulses are counted and displayed on a PC as a function of the corresponding photon energy, producing a spectrum of the fluorescence radiation.

This sort of detector has an inherently low quantum efficiency, which compounds the difficulties involved in soft X-ray spectroscopy, particularly the characteristically low fluorescence yields. At Beamline 8.0.1 the first stage of the MCP detector is coated with CsI, increasing the quantum efficiency of the detector to between 10% and 20%.

3.2. Beamline 6.3.2

The absorption-only Beamline 6.3.2 is slightly different from Beamline 8.0.1, even neglecting the absence of a spectrometer at the former facility. As was mentioned previously, the source of the radiation at Beamline 6.3.2 is a bending magnet, rather than an undulator, so the intensity of the light is significantly lower than at Beamline 8.0.1. The physical layout of Beamline 6.3.2 is shown in Figure 3.5, taken from the Center for X-ray Optics website.¹² Although the layout is different, the purposes of the various components can easily be inferred through comparison with Beamline 8.0.1.

Figure 3.5 includes the reflectometer and detector that were not used for the XAS measurements in this study. Instead, total electron yield measurements were performed by attaching an alligator clip to the sample holder and measuring the sample current that was produced when electrons were ejected from the sample. Also, due to the relatively low photon flux delivered by the bending magnet, it was impractical to monitor the number of photons passing through the beamline using a gold mesh. Therefore, regular measurements of the sample current produced by irradiation of clean gold foil were required for normalization, which will be discussed in Section 8.

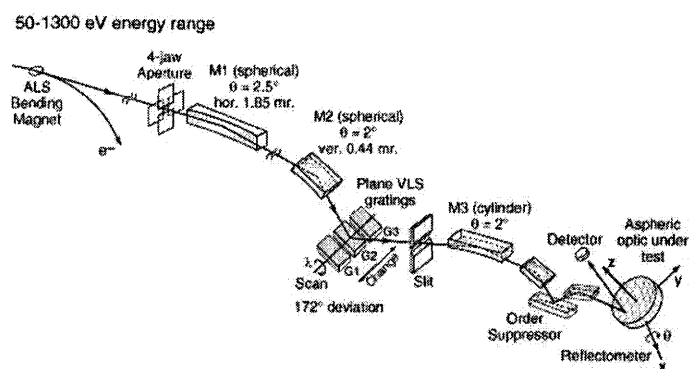


Figure 3.5 Schematic representation of Beamline 6.3.2 at the ALS, including reflectance endstation.

4. SOFT X-RAY SPECTROSCOPY

Soft X-ray spectroscopy is used to probe the electronic structures of materials. A number of characteristics are related to the electronic structure, such as conductivity, magnetism, electron transfer, etc. Soft X-ray spectroscopy is a general term encompassing a number of complementary techniques; the two that were used in this study are soft X-ray emission spectroscopy (XES) and X-ray absorption spectroscopy (XAS). Used together, these techniques provide a picture of the local partial densities of occupied and unoccupied electronic states, respectively.

Soft X-ray spectroscopy methods involve the production and monitoring of transitions between core states and either valence or conduction states. In XES measurements, a core hole is created via excitation with synchrotron radiation and the radiative transition that results when it is refilled is monitored. In XAS measurements, the amount of incoming photons that is absorbed through the creation of a core hole is observed.

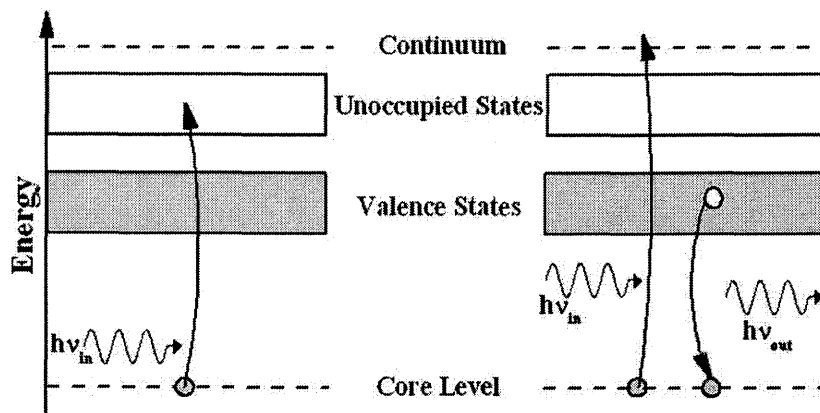


Figure 4.1 Schematic representation of the radiative transitions involved in XAS (left) and XES (right).

Figure 4.1 shows a schematic representation of the XAS and XES processes. Since the transitions that are being monitored are radiative, the information they provide is restricted by dipole selection rules. The dipole selection rules govern the changes in quantum numbers that an electron can undergo during excitation or relaxation. Using single-electron notation, the allowable transitions that an electron can undergo are those that do not violate the following conditions: $\Delta l = \pm 1$, $\Delta s = 0$, $\Delta j = 0$ or ± 1 , and $\Delta m_j = 0$ or ± 1 (although $m_j=0 \rightarrow m_j=0$ transitions are not allowed if $\Delta j = 0$). The change in the principle quantum number, Δn , is not constrained.

Soft X-ray spectra are generally labeled according to the quantum numbers of the core hole created by the irradiation. XAS generally uses atomic notation to denote the identity of the core hole, while XES uses X-ray notation with the letters K, L, M..., corresponding to the value of the principal quantum number n . To differentiate between the different subshells in the latter convention, an integer subscript is used. The value of the subscript increases according to the value of the total angular momentum quantum number j . It is perhaps more convenient to think of the increasing subscript as corresponding to a decrease in the binding energy of the core state. The atomic and X-ray notations for the core levels that are commonly of interest in soft X-ray spectroscopy are shown in the table below.

Table 4.1: Notations used in X-ray spectroscopy to describe core levels.

Atomic Notation	X-ray Notation	Quantum Numbers		
		n	l	j
nl_j	n_m	n	l	j
$1s_{1/2}$	K	1 (K)	0 (s)	1/2
$2s_{1/2}$	L_1	2 (L)	0 (s)	1/2
$2p_{1/2}$	L_2	2 (L)	1 (p)	1/2
$2p_{3/2}$	L_3	2 (L)	1 (p)	3/2
$3s_{1/2}$	M_1	3 (M)	0 (s)	1/2
$3p_{1/2}$	M_2	3 (L)	1 (p)	1/2
$3p_{3/2}$	M_3	3 (L)	1 (p)	3/2

The X-ray notation can be modified to describe transitions between two core levels. For these transitions, a subscript from the Greek alphabet is used to describe the order of the transitions, with higher subscripts symbolizing transitions from more loosely

bound core states. As an example, the emission feature arising from transitions from the $L_{2,3}$ level to the K level is the K_α feature, while transitions from the $M_{2,3}$ level to the K level produce the K_β feature. Transitions from L_1 (2s) or M_1 (3s) to K are not included, as they are forbidden by the dipole selection rules, as $\Delta l = 0$ in those cases.

While XES and XAS provide a very good indication of the local partial density of electronic states of a system, the character of the unoccupied states is affected by the presence of the core hole created during the absorption process. The core hole only has a significant effect on the absorption measurements, not the emission measurements, because of the final-state rule.¹³

The final-state rule simply states that an electronic transition takes place in the potential defined by the final electron configuration. In the case of emission, a valence electron fills a core hole created through photon excitation, and the final electronic core state is said to be identical to the ground state. As a result, emission spectra provide a picture of the occupied density of electronic states in the valence band, relatively unperturbed by the potential of the core hole. Conversely, an absorption measurement inherently contains an excited electron and a core hole, meaning that XAS measurements probe the unoccupied density of electronic states in the presence of a modified core potential. While the effect of the core hole may be relatively small, it must be taken into account when analyzing the absorption spectra.

Both absorption and emission methods are element- and site-specific in the soft X-ray region, allowing the contributions of the individual components of a particular material to be studied individually. This specificity is achieved by selectively exciting the unique core levels of each element or site in order to monitor transitions involving that core level specifically.

Traditionally, soft X-ray techniques have been hampered by some inherent difficulties. Low fluorescence yields in the soft X-ray region are the inevitable result of the fact that holes created in shallow core levels are filled much more efficiently through non-radiative processes than by radiative transitions.¹⁴ As a result, the study of these transitions using traditional X-ray tube techniques is impractical, due to the low

intensity of the light that is produced. This fundamental difficulty was overcome with the advent of 3rd generation synchrotron light sources producing highly brilliant light over a broad spectrum. The high intensity of the synchrotron radiation allows for a greater number of excitations and a corresponding increase in the number of radiative transitions.

The curves in Figure 4.2 were taken from the X-ray Data Booklet prepared by the Lawrence Berkeley National Laboratory,¹⁵ and are based on the numbers tabulated by Krause.¹⁴ The curves represent the fraction of all transitions into a given vacant K or L shell orbital that are radiative, plotted as a function of the atomic number of the element in question. The spectra that are studied in this work are the K emission of carbon, nitrogen, and oxygen ($Z=6-8$) and the L-emission of iron ($Z=26$). Inspection of Figure 4.2 illustrates the fact that the fluorescence yields for these transitions are extremely low.

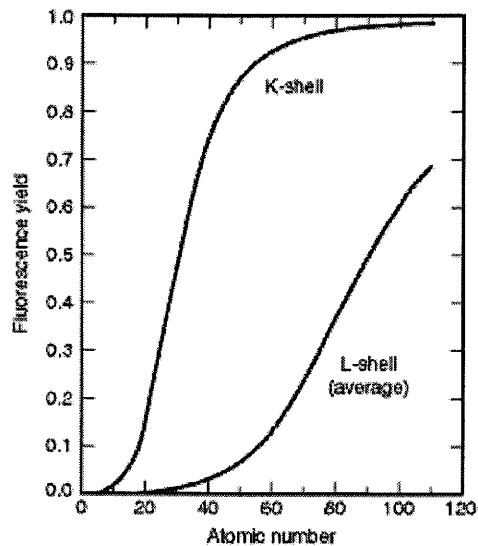


Figure 4.2 The fluorescence yields of the K and L shells plotted as a function of atomic number.

The following sections provide a specific analysis of the methods and instrumentation used in soft X-ray absorption and emission spectroscopy.

4.1. X-ray Absorption Spectroscopy (XAS)

X-ray absorption spectroscopy is used to probe the unoccupied partial density of electronic states (PDOS) of a material. The spectra of the unoccupied states are related to the type of bonding found in the material and can give valuable information regarding electron transport, optical properties, and other properties.

Absorption measurements are performed by manipulating the monochromator and undulator such that the energy of the exciting radiation is scanned across a core-level absorption threshold of the elements being studied. The energy is increased or decreased by discrete amounts, and the relative photon absorption at each level is recorded for a set time interval. The spectra are comprised of the superposition of a number of features, including resonant excitations to discrete electronic states and features due to the photoionization of the core levels.

Figure 4.3 shows the C 1s XAS spectrum of buckminsterfullerene (C_{60}) measured at Beamline 8.0.1 of the ALS. Its form is representative of soft X-ray absorption spectra as a whole, and is included here to provide a visual reference for the discussion of the XAS technique. The most prominent features in the spectra are the aforementioned resonance peaks. When the energy of the incident photons closely approaches that of an allowed transition from the core-level to an unoccupied orbital, the photons are strongly absorbed, resulting in a narrow peak. The position of the resonance feature, therefore, provides an indication of the energy of the previously unoccupied orbital relative to the core hole created by the incoming photon. As mentioned previously, the field of the core hole affects the energy level of the excited electron, resulting in a shift of the resonance features to lower energies. This core hole effect must be considered when absorption spectra are analyzed.

The peaks associated with the resonant excitation of the core levels are superimposed on the step-like signal due to the ionization of the core-level electrons. The approximate shape and position of this step feature is indicated by the dashed line in Figure 4.3. While XAS is not an ideal technique for studying the ionization edge of a material, in many cases the location of the edge is useful for calibration of the energy

axis, among other things. The techniques used to analyze different regions of the spectrum allow a variety of information to be obtained. This study focuses on the features that are found below the ionization potential, with only occasional reference to the higher-energy resonant features. The study of this portion of an XAS spectrum is often referred to as near-edge X-ray absorption fine structure (NEXAFS) spectroscopy, although the more general term (XAS) will be used throughout this study.

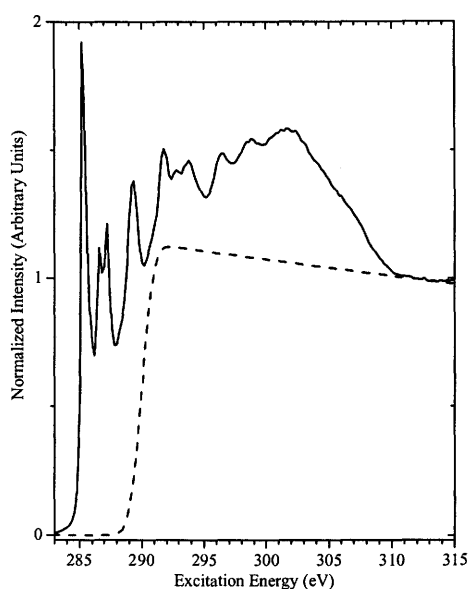


Figure 4.3 C 1s XAS spectrum of C_{60} , with the approximate shape and position of the photoionization step function shown (dotted line). The spectrum was measured at Beamline 8.0.1 of the ALS synchrotron.

A variety of methods can be used to obtain XAS spectra of a material. The most classic and direct method is to illuminate the sample and measure the amount of electromagnetic radiation that passes through it. This method can provide a very good indication of the quantitative absorption coefficient of a material, but it is hindered by the requirement of an extremely thin and uniform sample. In the majority of cases, measuring absorption spectra via transmission is impractical, if not impossible.

Three methods for obtaining absorption spectra are used at the beamlines at which the data for this study were acquired, all of which have various strengths and weaknesses. A discussion of these three methods – total electron yield (TEY), total fluorescence yield (TFY), and partial fluorescence yield (PFY) – follows.

4.1.1. Total Electron Yield (TEY)

Total electron yield measurements determine the relative absorption of the incoming photons by monitoring the current flowing from the sample as a function of the excitation energy. The current is produced when electrons are ejected from the sample and are replaced by electrons from the sample holder.

One method by which electrons are ejected from the sample is via ionization. When the energy of the incoming radiation exceeds the ionization energy, the core electron is ejected from the sample. This electron must be replaced if the electrical neutrality of the sample is to be maintained. The influx of electrons from the electrically insulated sample holder results in a net positive current flowing from the sample, the magnitude of which is proportional to the number of electrons that are removed from the sample, and therefore to the magnitude of its ionization cross-section.

The ejection of primary electrons during ionization is a simple one-step process, but it does not explain the presence of peaks due to the absorption occurring as a result of transitions to bound states. In these resonant transitions, the total charge of the sample remains neutral, since the excited electron is still bound to the nucleus. Fortunately, the resonant absorption can be measured using a second-order process. As mentioned previously, an electron can move from a high-energy state to a low-energy state via fluorescence or Auger electron emission, and the Auger process dominates for all small atoms.¹⁴ In Auger decay, an electron decays to a more tightly bound, unoccupied state, and the excess energy is dissipated via the emission of a loosely bound valence electron. The valence electron must then be replaced, as in direct photoionization, resulting in a measurable flow of electrons.

Since TEY measurements require the emission of electrons, they are considerably more surface sensitive than are fluorescence yield measurements, as the escape depth of electrons is much lower (~1 nm for carbon) than that of photons (~1000 nm for carbon) for any given energy¹⁵. This surface sensitivity has a useful consequence, however, in that a combination of electron and fluorescence yield measurements can be used to detect the effects of surface contamination on a sample. Furthermore, the amorphous nature of molecular systems suggests that surface sensitivity does not have as large an effect on samples of this type as on solid-state systems.

The insulating behaviour of many of the samples that are studied here leads to another difficulty in TEY measurements. In such samples, the emission of electrons is not affected, but the replacement of those electrons is slowed. As a result of this sample charging, the measured current is lower than expected, and fails to provide an accurate portrayal of the absorption. Charging is a common problem when dealing with biological samples, but it can often be overcome through proper sample preparation and mounting.

4.1.2. Fluorescence Yield Measurements

Fluorescence yield measurements rely entirely on second-order processes to provide a measurable quantity related to the absorption of the incoming photons. As such, the measured signal is strongly dependent on the likelihood of a particular excited state to decay via fluorescence. The detection method, as well as the information acquired, depends on whether the measurements are of the total (TFY) or partial (PFY) fluorescence yield type.

A general weakness associated with fluorescence yield measurements of absorption is that they do not provide as accurate a picture of the total photoabsorption cross section as do TEY methods. The source of this problem is the self-absorption of the outgoing photons, which is an unavoidable consequence of fluorescence measurements of bulk samples.

Figure 4.4 shows the inverse of the attenuation length of photons in carbon in the energy range associated with C 1s XAS. The attenuation length is inversely proportional to the photoabsorption coefficient, and so the curve provides an indication of the behaviour of the latter quantity as a function of excitation energy. The curve was calculated using a database found on the Center for X-ray Optics' website,¹⁶ and is based on the values tabulated by Henke.¹⁷

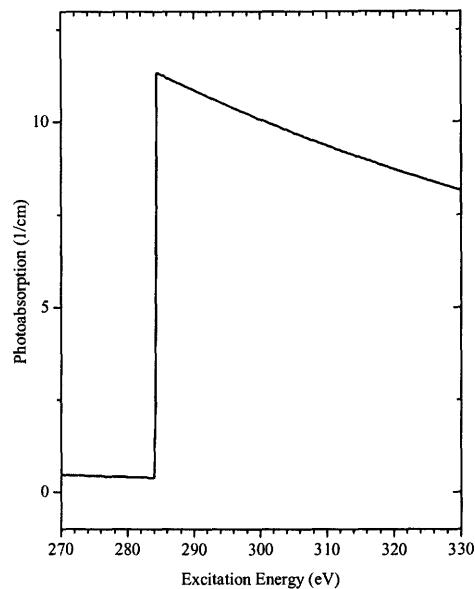


Figure 4.4 The inverse of the attenuation length of photons in carbon for the energy range encompassing to the energy region monitored in C 1s XAS spectra. The attenuation length is inversely proportional to the photoabsorption.

The maximum possible energy of the emitted photon is that of the absorbed photon; in practice, however, the emitted photon has a lower energy. In general, photons with lower energy will be more strongly absorbed than those having higher energy, as is shown by the general decrease in the value of the curve in Figure 4.4 as energy is increased. However, the obvious exception comes at the step associated with the ionization of the C 1s electrons. When the excitation energy crosses this threshold, the incoming photons are absorbed very strongly, while the lower-energy outgoing photons

are more likely to leave the sample. This large mismatch in the absorption coefficients may lead to intensity levels in the fluorescence yield spectra that are not directly proportional to the number of photons being absorbed.¹⁸ Although Figure 4.4 does not show any of the fine structure associated with transitions to bound states, a similar phenomenon occurs when the excitation energy crosses these thresholds.

Despite the difficulties associated with fluorescence yield methods, they often provide unique information about the electronic structure of a sample, and so it is useful to discuss these methods in detail.

Total fluorescence yield measurements attempt to detect all of the photons emitted from the sample, regardless of energy. The photons are detected by an electron multiplier known as a channeltron. When a photon with energy greater than the channeltron's detection threshold impinges on it, a free electron may be produced. The electron will then be accelerated by the large bias voltage (approximately 3000 V) of the channeltron and produce a cascade of free electrons that can be measured and recorded. The electron cascade measurements must be closely monitored due to the possibility of overload. If the count rate becomes too large, (approximately 10^6 /second) the pulses can overlap and become indistinguishable from each other. As a result of this overlap, the number of pulses detected will actually decrease as the number of photons impinging on the channeltron increases. This effect provides a ceiling for the obtainable count rate, but this maximum is sufficiently high that the statistical error associated with TFY measurements is negligible. Overload can be avoided by decreasing either the bias voltage or the number of photons impinging on the sample.

While TFY measurements are extremely useful due to their high count rates and their bulk-sensitive properties, it is sometimes desirable to monitor the amount of the incoming photons that are absorbed due to a particular resonant transition. Energy selectivity is required for this type of measurement, and so a channeltron, which does not identify the energy of the impinging photon, cannot provide transition-specific information.

Partial fluorescence yield measurements are designed to monitor only the photons that are emitted within a certain energy window. At Beamline 8.0.1 the PFY measurements use the XES spectrometer to record the absorption spectrum. The range and position of the spectrometer window is adjusted such that it corresponds to the energy of the transition in question; the characteristics of the window are determined by identifying the relevant transitions from an initial XES measurement. The excitation of the sample is performed in the same way as for other absorption measurements, and the number of photons impinging on the spectrometer is recorded for each iterative step.

The main disadvantage of PFY measurements is their inherently low count rate. This difficulty arises from the experimental setup, which necessarily requires that the fluorescence photons pass through a narrow spectrometer slit, causing only a small fraction of the relevant photons emitted by the sample to be detected. As with XES measurements, the small detector window is necessary for the energy resolution of the spectrometer. An additional factor that contributes to the low count rate of PFY measurements is the aforementioned tendency of excited states to decay via non-fluorescent decay mechanisms.

The problems associated with low count rates are far from insurmountable, however. The standard remedy for low count rates is to increase the counting time. For PFY measurements, this means that the counting time associated with each iteration of the excitation energy must be sufficiently long to produce a statistically significant number of counts. The total time needed to measure a PFY spectrum can be expressed by the formula:

$$t = \frac{\Delta t}{\Delta E} E \quad (4.1)$$

where Δt is the time needed to acquire the desired number of counts at each energy step, ΔE is the magnitude of the energy steps, and E is the total energy range over which the spectrum is being measured.

Typically, an absorption spectrum will be composed of on the order of 300 steps, and each step will require a counting time measured in minutes, as opposed to fractions of a second for other methods. As a result, it may take several hours to measure a meaningful PFY spectrum. The desire for high count rates and good statistical data must be mitigated by the need to use beamtime efficiently.

4.2. X-ray Emission Spectroscopy (XES)

As was mentioned at the beginning of this chapter, X-ray emission spectroscopy provides a picture of the partial occupied density of electronic states of a material, which is complementary to the information provided by absorption spectroscopy. Emission spectroscopy is divided into two categories, based on the relative energies of the excitation and the emission processes. In non-resonant X-ray emission spectroscopy (referred to by the general term XES), the monochromator is set such that the excitation energy is well above the ionization threshold of the core state of the element being examined, removing the core electron from the system entirely. Because the core electron is removed it does not have an influence on the refilling of the core hole, and so the fluorescence decay of the valence electrons is governed only by the standard dipole selection rules. In the case of resonant excitation, however, this is not the case.

The excitation and emission processes associated with resonant inelastic X-ray scattering (RIXS) measurements cannot be decoupled. As the name suggests, the excitation energy in RIXS measurements is set such that it corresponds to a transition from a core state to an unoccupied bound state. The energy corresponding to these resonant transitions can be readily determined from the location of the resonance peaks in XAS spectra. Because individual resonance features are often associated with a particular atomic site in a substance, the emission spectrum that is produced when exciting at that energy provides information about the electronic structure of that particular site.

5. DENSITY FUNCTIONAL THEORY

The electronic structure of a material can be expressed as a solution to the many-particle Schrödinger equation having the form

$$H\psi(x_1, x_2, \dots, x_N) = E\psi(x_1, x_2, \dots, x_N) \quad (5.1)$$

where $\psi(\vec{x}_1, \vec{x}_2, \dots, \vec{x}_N)$ is the total N-electron wave function and the eigenvalue E is the ground state energy of the system. The individual contributions \vec{x}_i contain both the spatial (\vec{r}_i) wave function and the spin (σ_i) information, such that the i^{th} electron is completely described by the function

$$\vec{x}_i = \vec{r}_i \sigma_i. \quad (5.2)$$

Solutions to the equation must take into account the kinetic energy (T) of the electrons, as well as the attractive interactions between the electrons and the nuclei (V_{n-e}) and the electron-electron repulsion (V_{e-e}). The Hamiltonian (H) can therefore be written

$$H = T + V_{n-e} + V_{e-e}. \quad (5.3)$$

Unfortunately, the Schrödinger equation is exactly solvable for only a very limited number of systems, with the N-electron molecule not being counted among their number. As it is therefore impossible to analytically determine the characteristic wave function of the molecule in this manner, it has been necessary to develop methods that can be used to approximate it.

Density functional theory (DFT) is a widely used method for studying electronic structure. It has as its basis the assumption that the electronic structure of an N-particle system can be described in terms of a single density function (hereafter designated ρ)

rather than N single-electron functions. The DFT approach uses several useful assumptions and procedures that allow for speedier calculations than are associated with other methods, most notably the considerably more rigorous Hartree-Fock approach.¹⁹ Density functional theory calculations involve the self-consistent solution of a series of equations using numerical methods.

The theoretical justification of the use of the electron density in electronic structure calculations was first published by Hohenberg and Kohn,²⁰ and their theorems led to the development of modern DFT methods. The following year, Kohn and Sham²¹ developed a method for determining the density functional through the self-consistent solution of a set of three equations. The following sections describe the origin and development of DFT, including the details of the calculations that are found later in this work.

5.1. The Hohenberg-Kohn Theorems

In 1964, Hohenberg and Kohn presented the first formal proof of the ability of electron density functions to provide a complete description of the electronic structure of a many-electron system. A summary of the proof is presented below, owing much to the analysis by Chretien and Salahub in their treatise on density functional theory.²²

Using the definitions from the previous section, the general, exact form of the electron density function can be written as

$$\rho(r_1) = N \int \dots \int d\sigma_1 dr_2 d\sigma_2 dr_3 d\sigma_3 \dots dr_N d\sigma_N |\psi(x_1 \dots x_N)|^2. \quad (5.4)$$

This function represents the probability that electron 1 can be found having a spin state σ_1 and a spatial wave function r_1 while the rest of the electrons in the system are found in the volume element described by the remaining differential elements in Eq. 5.4. The density must also obey the normalization condition

$$\int \rho(r_1) dr_1 = N. \quad (5.5)$$

As this definition of the electron density function is dependent on the N-particle wave function, it cannot be solved for analytically. Fortunately, the theorems of Hohenberg and Kohn are proved for a general, unknown density functional and are therefore universally applicable. In order to prove that the general density function ρ is a valid substitute for the N-particle wave function, it must be shown that it is a singular function of the potential generated by the nuclear structure, $V(\vec{r}_i)$, and that, conversely, this potential is unique for a particular density.

The first condition is easily satisfied by examination of the definitions of the parameters involved. The Hamiltonian defined in Eq. 5.3 can be rewritten using more specific definitions of the three terms, as shown below.

$$H = \sum_{i=1}^N \left(-\frac{1}{2} \nabla_i^2\right) + \sum_{i=1}^N V(\vec{r}_i) + \sum_{i=1}^N \sum_{i < j}^N \frac{1}{|\vec{r}_i - \vec{r}_j|} \quad (5.6)$$

The second term is the one we are most concerned with at this point, and it can be written in a more specific form as

$$\sum_{i=1}^N V(\vec{r}_i) = \sum_{i=1}^N \sum_{\alpha=1}^M \frac{-Z_{\alpha}}{|\vec{R}_{\alpha} - \vec{r}_i|}, \quad (5.7)$$

where Z_{α} is the atomic number of atom α , R_{α} is its position, and M is the number of atoms in the system.

When the number of electrons in the system is known, the kinetic and electron-electron terms of the Hamiltonian are fixed, and so the only parameter that is dependent on external factors is the nuclear repulsion term. Therefore, for a given potential $V(\vec{r}_i)$ the Hamiltonian is explicitly defined, and so, therefore, is the wave function $\psi(\vec{x}_1, \vec{x}_2, \dots, \vec{x}_N)$. Thus, it is shown that the density function in Eq. 5.4 is unique for any given potential $V(\vec{r}_i)$.

The above proof is relatively simple, as it follows directly from the definitions of the parameters involved. The proof of the converse relation, namely that a given electron density can be produced by only one unique potential, must be proved by contradiction. Specifically, it is first assumed that a given density $\rho(r)$ will arise in the presence of two different potentials, $V_1(\vec{r})$ and $V_2(\vec{r})$, and it will then be shown that this assumption leads inevitably to a contradiction. The Hamiltonians involving the two potentials will be referred to as H_1 and H_2 , respectively. Because the Hamiltonians of the two systems differ from each other, their eigenfunctions (the N-particle wave functions) and possibly their eigenvalues (the ground state energy of the system) must also differ. These parameters will be denoted by ψ_1 and ψ_2 and E_1 and E_2 , respectively. The individual contributions, \vec{x}_i , to the wave functions have been omitted for simplicity.

From this point on, the proof proceeds rather simply. By definition, each energy eigenvalue corresponds to the lowest possible energy state associated with its Hamiltonian, and we can therefore create the following inequality.

$$E_1 = \langle \psi_1 | H_1 | \psi_1 \rangle < \langle \psi_2 | H_1 | \psi_2 \rangle = \langle \psi_2 | H_2 - V_{1_{n-e}} + V_{2_{n-e}} | \psi_2 \rangle \quad (5.8)$$

The right-hand side of the equation requires that the kinetic and electron repulsion terms in the two Hamiltonians be identical. As was mentioned in the first portion of the proof, these two terms are dependent only on the number of electrons in the system, and so the equality is justified. A similar inequality for E_2 can be derived in the same way, and this pair of expressions can be simplified to read

$$E_1 < E_2 + \langle \psi_2 | -V_{1_{n-e}} + V_{2_{n-e}} | \psi_2 \rangle \quad (5.9a)$$

$$E_2 < E_1 + \langle \psi_1 | -V_{2_{n-e}} + V_{1_{n-e}} | \psi_1 \rangle. \quad (5.9b)$$

When added together, 9a and 9b lead to the paradoxical inequality

$$E_1 + E_2 < E_2 + E_1. \quad (5.10)$$

The significance of this contradiction is that it illustrates that two different external potentials, and by extension two different N-particle wave functions, cannot produce identical density functionals. The electron density functional is therefore shown to provide a complete description of the electronic structure of a system.

The ground state energy of the system (E_0) is related to the density functional in the same way that it is related to the wave function in a traditional N-particle Schrödinger equation, although by convention it is written in a slightly different form. The energy equation includes a term incorporating the external potential $V(\vec{r}_i)$ and a second term in the form of a universal functional of $\rho(\vec{r})$, designated $F_{HK}[\rho(\vec{r})]$. This universal functional represents the kinetic energy and electron repulsion energy terms.

$$E_0[\rho(\vec{r})] = \int V(\vec{r})\rho(\vec{r})d\vec{r} + F_{HK}[\rho(\vec{r})] \quad (5.11)$$

The Hohenberg-Kohn theorems provided both a theoretical justification of density functional theory and a starting point for the development of numerical methods for solving DFT-based problems. They led directly to the development of the Kohn-Sham equations that form the basis of most modern density functional calculations.

5.2. The Kohn-Sham Method

The Kohn-Sham method involves finding the form of a universal functional $F[\rho(r)]$ that takes into account kinetic energy and electron repulsion, as well as exchange and correlation energies. The functional can no longer be considered to have the same definition as in the original Hohenberg-Kohn theorems, and so the HK subscript has been dropped at this point. The Kohn-Sham method for determining $F[\rho(r)]$ can be viewed as an application of perturbation theory. Approximate models of the kinetic energy and electron repulsion terms are developed and solved exactly; a correction is then applied to more accurately model the real situations.

5.2.1. The Universal Functional

The electron repulsion is initially modeled with an explicit calculation of the classical electron-electron Coulomb interaction for a uniform electron gas. This Coulomb repulsion dominates the interactions between electrons and forms the basis for any perturbative calculations. A corrective term is added to the interaction to account for all non-classical effects, such as exchange, correlation, and self-interaction energies. These methods will be discussed at greater length later in the manuscript.

The kinetic energy of the electrons in a molecule forms a large portion of the functional $F[\rho(r)]$, and so it is desirable to represent it as accurately as possible. Unfortunately, the kinetic energy of a system of interacting particles cannot be determined through analytical methods, and so it is necessary to develop approximate models of the quantity. Kohn and Sham proposed to first determine the exact kinetic energy of a *non-interacting* electron gas having the same density as the real, interacting system. In this way, as with the electron repulsion energy, the largest contribution to the kinetic energy can be exactly determined. This theoretical kinetic energy can then be adjusted to include interaction effects. By this method, the kinetic energy term of the energy functional can be determined with great accuracy and relative ease.

The Kohn-Sham form of the energy functional is described by Eq. 5.12. The term $T_s[\rho(r)]$ is the kinetic energy of the non-interacting system described above. The dependence on $\rho(\vec{r})$ indicates that this system has the same density as the interacting system that we wish to model. The next term, $J[\rho(\vec{r})]$, is the classical electron-electron repulsion energy that was previously discussed.

$$F[\rho(\vec{r})] = T_s[\rho(\vec{r})] + J[\rho(\vec{r})] + E_{xc}[\rho(\vec{r})] \quad (5.12)$$

The final term in Eq. 5.12 is the exchange-correlation energy. Encompassing, as it does, all non-classical interactions, no exact expression for $E_{xc}[\rho(\vec{r})]$ can be developed for an arbitrary density functional. Symbolically, $E_{xc}[\rho(\vec{r})]$ can be expressed, as in Eq. 5.13, as the sum of the differences between the approximate representations of the terms in

$F[\rho(\vec{r})]$ and the corresponding terms in the real physical system. The exchange-correlation term must be determined numerically; the methods used to derive the models will be discussed later.

$$E_{xc}[\rho(\vec{r})] = T[\rho(\vec{r})] - T_s[\rho(\vec{r})] + V_{ee}[\rho(\vec{r})] - J[\rho(\vec{r})] \quad (5.13)$$

5.2.2. The Kohn-Sham Equations

With these definitions and theorems in place, a series of equations relating the density functional, the effective potential, the exchange and correlation interactions, and the energy of the system can be derived. The first step is to define the energy equation as follows.

$$E[\rho(\vec{r})] = T_s[\rho(\vec{r})] + \frac{1}{2} \iint \frac{\rho(\vec{r})\rho(\vec{r}')}{|\vec{r} - \vec{r}'|} d\vec{r}d\vec{r}' + \int V(\vec{r})\rho(\vec{r})d\vec{r} + E_{xc}[\rho(\vec{r})] \quad (5.14)$$

As the energy is a function of $\rho(\vec{r})$, it is apparent that the lowest energy will be that which corresponds to the ground state density. Differentiating Eq. 5.14 with respect to the density functional and setting the result equal to zero, Kohn and Sham arrived at the following expression:

$$\int \rho(\vec{r}) \left[V(\vec{r}) + \int \frac{\rho(\vec{r}')}{|\vec{r} - \vec{r}'|} d\vec{r}' + V_{xc}[\rho(\vec{r})] + \frac{\partial T_s[\rho(\vec{r})]}{\partial \rho(\vec{r})} \right] d\vec{r} = 0 \quad (5.15)$$

where $V_{xc}[\rho(\vec{r})] \equiv \frac{\partial E_{xc}[\rho(\vec{r})]}{\partial \rho(\vec{r})}$.

Collectively, the first three bracketed terms reflect the effective potential, which will be designated $V_{eff}[\rho(\vec{r})]$, that is associated with the density functional $\rho(\vec{r})$. By defining $V_{eff}[\rho(\vec{r})]$ in this way, all classical and non-classical effects are included in the potential and the system can be analyzed as if it were a system of non-interacting particles defined by $\rho(\vec{r})$. The effective potential requires only a suitable model for the exchange and

correlation interactions to become exactly solvable for a given density functional. Formally, the potential is defined as

$$V_{eff}[\rho(\vec{r})] = V(\vec{r}) + \int \frac{\rho(\vec{r}')}{|\vec{r} - \vec{r}'|} d\vec{r}' + V_{xc}[\rho(\vec{r})]. \quad (5.16)$$

As a result of the isolated nature of the electrons in the Kohn-Sham model, the density functional can be expressed as a superposition of N single-particle orbital functions.

$$\rho(\vec{r}) \equiv \sum_{i=1}^N \sum_{\sigma=\uparrow,\downarrow} |\phi_i(\vec{r}, \sigma)|^2 \quad (5.17)$$

The orbitals in Eq. 5.17 are eigenfunctions of the one-electron Hamiltonian that includes the effective potential defined by Eq. 5.16. The corresponding single-electron Schrödinger equation can be written

$$\left[-\frac{1}{2} \nabla^2 + V_{eff}[\rho(\vec{r})] \right] \phi_i(\vec{r}, \sigma) = \epsilon_i \phi_i(\vec{r}, \sigma). \quad (5.18)$$

These three equations (5.16, 5.17, and 5.18) are known collectively as the Kohn-Sham equations, and must be solved as a self-consistent system. A complete solution of the Kohn-Sham equations gives a description of the density functional, the effective potential, and the orbitals associated with each electron in the system. Although sophisticated numerical methods must be used to solve the equations, the general procedure is quite simple. Assuming that a model for $V_{xc}[\rho(r)]$ has been developed beforehand, a trial functional $\rho'(\vec{r})$ is chosen and inserted into Eq. 5.16. The effective potential $V_{eff}[\rho'(r)]$ is then inserted into Eq. 5.18 and the resulting eigenfunctions, $\phi'_i(r, \sigma)$, are used in Eq. 5.17 to define a new functional $\rho''(\vec{r})$. The cycle is repeated until the differences between the values associated with successive iterations are less than a preset threshold.

5.3. The Exchange Interaction

At this point, it is beneficial to provide a brief discussion of the previously mentioned exchange interaction. The largest non-classical effect in many electron systems, the exchange interaction is a quantum-mechanical phenomenon that describes the effect of the Pauli exclusion principle on the electrostatic repulsion between the electrons in a material. Descriptions can be found in most quantum mechanics books; the discussion found in this section owes much to the work in References 23-25.

5.3.1. Origin of the Exchange Interaction

Exchange interactions are found in all multi-electron systems, and arise from the inhomogeneities in electronic structure that are the inevitable result of the interactions of the various electron wave functions. The most important factors that must be taken into account are the Pauli exclusion principle and the antisymmetry of the overall electron wave function. For simplicity, the two-electron case will be discussed because it is easily visualized and it provides a complete analysis of the basic form of this phenomenon. The first step is to determine the form of the two-electron wave function. Like the function defined in Eq. 5.2, the wave function has both a spatial and a spin component. The spatial part of the two-electron wave function is formed from the wave functions of the two component electrons, and it is subject to the condition that the resulting probability distribution is invariant under the exchange of the two identical particles. That is, since electrons 1 and 2 are indistinguishable particles, and the numbering system is arbitrary, the system must not change when the positions of the electrons are interchanged²³. This condition leads to two possible functions, one symmetric, one antisymmetric. Using the notation seen in Eqs. 1 and 2, these functions are defined below.

$$\vec{r}_s(1,2) = \frac{1}{\sqrt{2}} [\vec{r}_1(1)\vec{r}_2(2) + \vec{r}_1(2)\vec{r}_2(1)] \quad (5.19a)$$

$$\vec{r}_a(1,2) = \frac{1}{\sqrt{2}} [\vec{r}_1(1)\vec{r}_2(2) - \vec{r}_1(2)\vec{r}_2(1)] \quad (5.19b)$$

Although interchange of the particles leads to a sign change in the antisymmetric wave function, $\vec{r}_A(1,2)$, the resulting probability distribution, $|\vec{r}_A(1,2)|^2$, is not affected. The antisymmetric wave function given by Eq. 5.19b also provides an illustration of the Pauli exclusion principle. If the two particles have identical quantum numbers, the function is described by $\vec{r}_A(1,1)$, which must be equal to zero. The same reasoning can be applied to the total wave functions (Eq. 5.21a,b) that will be discussed shortly, proving that if two particles in the same quantum state are described by an antisymmetric wave function, then the function must necessarily be equal to zero. The analysis can be extended to many-particle wave functions, providing a direct illustration of the Pauli exclusion principle.

The spin component of the total wave function is also subject to the condition of invariance under particle interchange. There are four possible spin combinations for the two particles: $\sigma_\alpha(1)\sigma_\alpha(2)$, $\sigma_\beta(1)\sigma_\beta(2)$, $\sigma_\alpha(1)\sigma_\beta(2)$, and $\sigma_\beta(1)\sigma_\alpha(2)$, where α and β represent spin-up and spin-down states respectively. The first two combinations are unequivocally symmetric, but the same cannot be said for the remaining functions. These combinations of spin are neither symmetric nor antisymmetric on their own, but can be used to create total spin functions that are analogous to the spatial functions found in Eq. 5.19.

$$\sigma_S(1,2) = \frac{1}{\sqrt{2}} [\sigma_\alpha(1)\sigma_\beta(2) + \sigma_\alpha(2)\sigma_\beta(1)] \quad (5.20a)$$

$$\sigma_A(1,2) = \frac{1}{\sqrt{2}} [\sigma_\alpha(1)\sigma_\beta(2) - \sigma_\alpha(2)\sigma_\beta(1)] \quad (5.20b)$$

The above discussion describes four possible forms for the total two-electron spin function, three symmetric and one antisymmetric. These states are known as the triplet and singlet states, respectively, and are associated with total spin quantum numbers of $S=1$ and $S=0$. Because the exchange interaction is based on the symmetries of the total

spatial and spin functions, the triplet states will be collectively represented by σ_s in the following discussion.

The total wave function for a system of electrons must be completely antisymmetric.* There are two combinations of spin and spatial functions that will satisfy the condition; one of them uses the singlet spin function, and the other requires a triplet spin state. These functions are shown below, and will hereafter be referred to in terms of their spin state. The numerical superscript preceding the wave function represents the value of the quantity $2S+1$ that is often used in spectroscopy to differentiate between multiplet states.

$${}^3\psi(1,2) = \vec{r}_A \sigma_s \quad (5.21a)$$

$${}^0\psi(1,2) = \vec{r}_s \sigma_A \quad (5.21b)$$

With these definitions in place, it is now a very simple matter to describe the origin of the exchange interaction. To this point, none of the models of electronic structure have included the effects of the electron spin. The exchange interaction arises from the different spatial distributions of the singlet and triplet states in a system. In the system presented above, two separate two-electron states have been described using two configurations of the same one-electron wave functions. The symmetry of the spatial portion of the singlet wave function will cause the two electrons to be, on average, closer together than in the triplet state. This difference in the spatial probability distributions causes the electron repulsion in the singlet state to be greater than that associated with the triplet state. The two-electron system is the simplest example of the exchange interaction, and is included here simply to illustrate the effects of spatial inhomogeneity on the electronic structure in a multiple electron system. All theoretical examinations of the electronic structure of a system must take the exchange interaction into account.

* This property is common to all multiple-fermion systems and is a consequence of the spin-statistics theorem of quantum field theory. An explanation of the theorem is well beyond the scope of this discussion, but a good discussion is presented in Schwabl's advanced quantum mechanics text. 24. F. Schwabl, *Advanced quantum mechanics* (Springer, Berlin; New York, 1999).

5.3.2. Approximations of the Exchange Interaction

In the rigorous Hartree-Fock method of determining electronic structures, the exchange energy is calculated explicitly by evaluating an exchange integral for each pair of electrons in the system.¹⁹ As mentioned above, DFT calculations rely on approximations to represent all non-classical effects, including exchange interactions and electron correlation. The origin of the exchange function in DFT can be directly illustrated by examining the difference between the real electron repulsion in a system and the repulsion that is classically expected. Introducing the density into the explicit form of this relation, the real, quantum mechanically correct electron repulsion can be expressed as the sum of the classical repulsion and a correction term, as shown below.¹⁹

$$\langle \psi | \sum_{i < j}^N \frac{1}{r_{i,j}} | \psi \rangle = \frac{1}{2} \iint \frac{\rho(\vec{r}_1)\rho(\vec{r}_2)}{|\vec{r}_1 - \vec{r}_2|} d\vec{r}_1 d\vec{r}_2 + \frac{1}{2} \iint \frac{\rho(\vec{r}_1)h(\vec{r}_1, \vec{r}_2)}{|\vec{r}_1 - \vec{r}_2|} d\vec{r}_1 d\vec{r}_2. \quad (5.22)$$

In Eq. 5.22, the correction term contains a function $h(r_1, r_2)$, which describes the density of a hole function, centred at r_1 , evaluated at the location specified by r_2 . The attractive Coulomb interaction between the exchange hole and the remaining electrons provides the necessary corrections to the classical theory. The idea of the Coulomb hole predates the use of DFT, having its origin in attempts to eliminate the tedious necessity of evaluating exchange integrals in Hartree-Fock calculations.²⁵ The hole function must satisfy the following conditions:²⁶

$$h(\vec{r}_1, \vec{r}_1) = -\frac{\rho(r_1)}{2} \quad (5.23)$$

$$h(r_1, r_2) \leq 0 \quad (5.24)$$

$$\int h(r_1, r_2) dr_2 = -1 \quad (5.25)$$

A number of different approximations of the exchange energy can be used in DFT calculations. Most are based on gradient expansions of the exchange energy term in Eq. 5.22. The expansion has the form²⁷

$$E_x[\rho(\vec{r}_1)] = -\frac{3}{4} \left(\frac{3}{\pi} \right)^{\frac{1}{3}} \int d\vec{r}_1 \rho^{\frac{4}{3}} + C_x \int d\vec{r}_1 \frac{|\nabla \rho|^2}{\rho^{\frac{4}{3}}} + \dots \quad (5.26)$$

Only the first two terms of the expansion are used in exchange energy approximations. If only the first term is retained, the resulting model is referred to as a local density approximation (LDA). The LDA is based on the general assumption that the exchange energy at any point is dependent only on the value of the density functional at that point. Although the hole density associated with the LDA satisfies all of the normalization conditions, this first-order model is not valid in practice.

The first attempt to correct the shortcomings of the LDA was known as the gradient expansion approximation (GEA) and sought to improve the approximation by simply retaining the second term in the expansion in Eq. 5.26. GEA used the exact numerical value of the second-order coefficient, C_x , and produced little to no improvement over LDA calculations. This deficiency was explained in a letter by John Perdew, who showed that the hole function associated with the GEA violated the conditions imposed by Eqs. 24 and 25.²⁸ Perdew's solution was to introduce cut-off functions into the GEA in order to correct its behaviour. The resulting approximation provides a vast improvement over LDA and GEA methods, but is, unfortunately, too complicated to be of any practical use. In particular, it is not possible to calculate the functional derivative of the energy expression, and so the potential $V_{xc}[\rho(\vec{r})]$ cannot be obtained. The form of this functional was simplified in a subsequent publication²⁶ by fitting polynomial functions to the expression. Similar methods were employed to develop an approximation to the correlation energy.²⁹ Perdew and Wang's method is an example of the generalized gradient approximation (GGA), a term that encompasses all methods employing the second order expansions of Eq. 5.26 while avoiding the shortcomings of GEA.

Another GGA method was developed by Becke,³⁰ who included empirical parameters in his model in order to obtain correct asymptotic behaviour. Becke's exchange functional is written

$$E_x = E_x^{LDA} + \beta \int \rho^{\frac{4}{3}} \frac{[s(r_1)]^2}{(1 + 6\beta s \sinh^{-1}[s(\vec{r}_1)])} d\vec{r}_1 \quad (5.27)$$

where E_x^{LDA} is the exchange energy predicted by the local density approximation, and β is the aforementioned empirical parameter. Eq. 5.27 and all other GGA exchange energies are dependent on the parameter $s(r_1)$, defined as

$$s(\vec{r}_1) = \frac{|\nabla\rho|}{\rho^{\frac{4}{3}}}, \quad (5.28)$$

which is seen in the second-order term of the gradient expansion (Eq. 5.26). The value of β was determined by performing a least-squares fit to the Hartree-Fock exchange energies calculated for the noble gases He-Rn. The calculations in this study make use of Becke's exchange function and Perdew's correlation function. The details of the calculations are contained in the following section.

5.4. Using the Kohn-Sham Framework

The Hohenberg-Kohn and Kohn-Sham papers provide theoretical justification of density functional theory as well as a basic outline of a computational method. They do not, however, provide any guide to the form of the density functional. Models of this form have become extremely sophisticated, as have the methods used to solve the set of Kohn-Sham equations. This section deals with the general method that is used to perform DFT calculations, as well as the specific methods used by StoBe,³¹ which is based on the DeMon DFT code.³² The following discussion owes much to the analysis that is found in Cramer's book on computational chemistry.¹⁹

Solving the Kohn-Sham equations requires a model of the electron density that can be easily modified in an iterative process. Just as the density can be expressed as the sum of the probability distributions of the individual orbitals in a system (Eq. 5.17), these orbitals can themselves be described as the sum of several simpler functions. Each

orbital can be represented as being composed of a number of basis functions as shown below.

$$\varphi = \sum_{k=1}^n a_k \chi_k \quad (5.29)$$

In Eq. 5.29, the basis function χ can have a number of forms; StoBe uses Gaussian-type functions. The coefficients of the basis functions are the parameters that are varied in DFT calculations, while the function itself is not altered. The basis functions are collectively known as a basis set, and a basis set usually has functions of more than one form. Generally, functions having the same symmetries as atomic orbitals (described as s , p , d , etc. functions) are included, as the orbitals in a molecular system can be generally expressed as being formed from the orbitals of each individual atom. The assumption that complex molecules can be described in this way is based on Molecular Orbital (MO) theory, which underlies all simulations of electronic structure, including DFT.

The Gaussian basis sets in StoBe are based on the Huzinaga basis sets³³ that were optimized for Hartree-Fock calculations. In general, basis sets are described by the number of s -, p -, and d -type functions included in the set. The notation ($n_s/n_p/n_d$) is commonly used to this end. Before the DFT calculation is begun, the LSD approximation is used to optimize the coefficients and exponents of the Gaussian basis functions, such that the total atomic energy is minimized. This step need only be performed once, as it is dependent only on the atomic number of the element in question and is therefore valid for all systems. It is these optimized basis functions that are used in the self-consistent field (SCF) portion of the calculations.

Most of the calculations in this study focus on descriptions of C, N, and O, and so a closer look at the basis sets associated with these elements is justified. The simplest Huzinaga basis sets for these elements have the basic form (63/5), meaning that a total of nine s -type functions and five p -type functions are used to describe the orbitals of the associated atom. Once this basis set has been optimized for a particular element, as described above, it is expanded in a way that will make it more useful in molecular calculations. Simply put, the blocks of three s -type functions and five p -type functions

are broken up to form a (621/41) basis set, which has greater flexibility than the contracted basis set. An additional, *d*-type function is included to better describe the effects of polarization. The resulting basis set is of the DZVP (double-zeta with valence polarization) form, and is written (621/41/1*). The DZVP basis set can be improved by the addition of extra functions. If an extra *s*- and an extra *p*-type function are included and the basis set is expanded further, it becomes a triple-zeta (TZVP) basis set, (7111/411/1*).

DFT calculations can be performed using only orbital basis sets; some of the calculations, however, can be simplified by including basis set representations of other parameters in the system, namely the density itself, rather than just its component orbitals, and the exchange correlation potential V_{xc} . As is the case with the orbitals, each atom in the system has one of these *auxiliary* basis sets associated with it. In terms of the auxiliary basis set, the density can be expressed as

$$\rho(\vec{r}) = \sum_{i=1}^m b_i \Omega_i . \quad (5.30)$$

The coefficients b_i are found by fitting the density functional described by Eq. 5.30 to the one that is formed by the orbital functions. This fitting is performed by minimizing the Coulomb energy between the two representations.³⁴ The auxiliary functions Ω_i differ from their orbital counterparts in that they are functions of probability density, rather than probability amplitude. Despite this difference in form, all deMon-based DFT programs use the orbital basis functions to provide a starting point for the fitting of the auxiliary density. The lowest exponent of the Gaussian orbitals is retrieved and inserted into the auxiliary function, after being doubled to represent the amplitude-squared nature of the functions Ω_i .

The representation of the exchange-correlation potential is accomplished using a similar procedure. Formally, the potential is written, in a manner completely analogous to Eq. 5.30, as

$$V_{xc} = \sum_{i=1}^p c_i \Phi_i. \quad (5.31)$$

The coefficients and exponents of the basis functions are determined by fitting the Gaussian-represented potential to the model potential. This procedure involves a least-squares fit at a number of mathematical grid points around each atom. As in the previous section, the starting values of the exponents are determined from the lowest-valued exponent in the orbital basis set. Rather than being doubled, as they are when the density was being modeled, the coefficients for the exchange-correlation functions are divided by three, reflecting the general $\rho^{\frac{1}{3}}$ dependence of the models of exchange-correlation potentials.

Auxiliary basis sets are formed from s -type functions and *blocks* of s -, p -, and d -type functions that are constrained to have the same exponent. This format is well suited to the calculation of molecular integrals. Because of the constraints on the p -, and d -type functions, the notation for auxiliary basis sets is different from the orbital notation. They are written in a $(k_s, k_{spd}; l_s, l_{spd})$ format, with the indices l and k representing the number of functions used to fit the density and the exchange-correlation potential, respectively. As will be discussed in Section 5.5.1, whenever possible the StoBe calculations performed in this study make use of the A5 auxiliary basis set, expressed as (5,2;5,2), that is derived from the TZVP orbital basis sets. As convergence was a problem in some cases, the A1 basis set (4,3;4,3) derived from the DZVP orbital functions was also employed in a limited number of cases

With the density and exchange-correlation potential thus represented, the difficulty lies in the determination of the orbital coefficients such that the ground state density is minimized. The basis of this determination is the application of a variational principle. The procedure that is used is analogous to the iterative process associated with the self-consistent solution of the Kohn-Sham equations, although the form of the equations must be altered to accommodate the presence of basis functions in the model.

The first step in the procedure is to choose basis sets for each atom in the system. At this point, the coefficients of the basis sets correspond to a generic starting value optimized for each element. The orbital coefficients are used to construct a density matrix, the elements of which are given by

$$P_{\lambda\sigma} = 2 \sum_{j=1}^{N_{occ}} a_{\lambda j} a_{\sigma j}, \quad (5.32)$$

where N_{occ} is the number of occupied orbitals in the molecule. The factor of two accounts for the double-occupancy of each orbital. Physically speaking, the matrix elements correspond to the magnitude of the contribution of each basis function to the overall wave function. This quantity provides a means for determining the relative importance of the various exchange and Coulomb interactions included in the model. The overall density matrix has the form

$$P = 2 \sum_{j=1}^{N_{occ}} \begin{bmatrix} a_{1j} a_{1j} & \dots & a_{1j} a_{Nj} \\ \vdots & & \vdots \\ a_{Nj} a_{1j} & \dots & a_{Nj} a_{Nj} \end{bmatrix}. \quad (5.33)$$

Once the preliminary steps of choosing the basis sets and constructing the density matrix have been performed, the analysis of the system can begin. The coefficients can be determined using a variational principle that is based on the premise, previously mentioned, that the ground state electronic structure of a system will be associated with the minimum value of its energy function. Cramer shows that the energy of a wave function can be expressed as

$$E = \frac{\sum_{i,j} a_i a_j K_{ij}}{\sum_{i,j} a_i a_j S_{ij}}, \quad (5.34)$$

where S_{ij} is called the overlap integral, and K_{ij} is the resonance integral. The overlap integral is simply an indication of the spatial overlap of two orbital basis functions.

$$S_{ij} = \int \chi_i \chi_j dr \quad (5.35)$$

The resonance integral is considerably more complex, and it includes terms describing all of the interactions in the system.

$$K_{\mu\nu} = \langle \chi_\mu | -\frac{1}{2} \nabla^2 + \sum_{\alpha=1}^M \frac{-Z_\alpha}{|\vec{R}_\alpha - \vec{r}|} + \int \frac{\rho(r')}{|\vec{r} - \vec{r}'|} d\vec{r}' + V_{xc} | \chi_\nu \rangle \quad (5.36)$$

In the case where $i=j$, the resonance integral is analogous to the single particle Schrödinger equation (Eq. 5.18) for an electron occupying an orbital described by χ_i . The physical significance of the integral when $i \neq j$ is more complex, but its magnitude is roughly correlated with the magnitude of the overlap integral.

Having now defined the terms in the energy expression (Eq. 5.34), we can now apply the variational principle. If the density function is to be at the ground state, then all of the orbitals, and, by extension, the basis functions, must be in their lowest energy configurations. Because the sole variables in the orbital basis functions are their coefficients a , it is those coefficients that must be varied in order to minimize the energy. Inspection of Eq. 5.34 supports this, since the integrals S_{ij} and K_{ij} are invariant once the basis set has been chosen and a model for the exchange and correlation potential has been applied. The coefficients are therefore the sole variables in the energy expression.

In order for the energy to be minimized, its partial derivative with respect to each coefficient must be equal to zero. If the necessary partial derivatives are calculated, the result is a set of N equations (with N being the number of basis functions) with N unknowns, defined by

$$\sum_{i=1}^N a_i (K_{ki} - ES_{ki}) = 0 \quad \text{for all } k. \quad (5.37)$$

The eigenvector defined by a_i will be nontrivial if and only if the determinant of the factors $(K_{ki} - ES_{ki})$ is equal to zero and E is an eigenvalue of the equation.³⁵ The determinant is written as

$$\begin{vmatrix} K_{11} - ES_{11} & \cdots & K_{1N} - ES_{1N} \\ \vdots & & \vdots \\ K_{N1} - ES_{N1} & \cdots & K_{NN} - ES_{NN} \end{vmatrix} = 0. \quad (5.38)$$

The above determinant will have N_{occ} solutions E_j that correspond to the energies of the occupied orbitals. Substituting each of these energies in turn into Eq. 5.37 will give the set of coefficients (the eigenvector a_i) that correspond to that orbital. With the basis set coefficients of each orbital determined, a new density matrix P' can be constructed. The new matrix can be compared to the matrix from the previous iteration, and if the difference between the two is less than a previously set convergence criterion, the calculation is completed. If the result is not yet satisfactory, the calculations are performed again with P' replacing P .

5.5. XAS Calculations

DFT calculations usually provide an indication of the density of electronic states of a molecule; in this study they are also used to simulate soft X-ray absorption spectra. Due to the final state rule that was discussed in Section 4, the simulation of the XAS spectra must be based on the orbitals found in the excited state of the system, *i.e.* they must include the core hole effect.

The method that StoBe uses to model this state involves the creation of a half-occupied core state, rather than a completely unoccupied state.^{36,37} This state is known as a transition state, and its application to this type of calculation was proposed by Slater for use in his $X\alpha$ method, to which the deMon code owes a great deal of its methodology.³² In the StoBe calculations, only the initial state is given an occupation of 0.5, the final state is left unoccupied, meaning that the calculation of the unoccupied states is performed using a frozen-orbital approximation, in which the potential due to the excited electron is not included in the Hamiltonian.³⁶ This approximation is employed largely to cut down on computation time, as to do otherwise would require a complete recalculation of the electronic structure for each transition that is to be modeled.

A separate XAS calculation must be performed for each atom in the molecule; the sum of the individual calculations provides a representation of the measured spectrum. While calculating the spectrum in this way is time-consuming, the site-resolved absorption spectra are invaluable in the analysis of the experimental data, as will be shown later in this work, beginning in Section 9.1.2.

Once the iterative process of determining the orbital energies for the transition state is completed, there is still another element of the calculation to be performed. In order to simulate the XAS spectra, the oscillator strength corresponding to each transition must be calculated. The total oscillator strength is determined from the x , y , and z components of the dipole transition moment. As an example, the x moment is given by³⁸

$$D_x = \langle \varphi_{core} | x | \varphi_f \rangle \quad (5.39)$$

where φ_{core} and φ_f are the core and final state orbitals, respectively. Once the dipole transition moments for a given transition have been calculated, the oscillator strength is simply given by^{36,38}

$$Osc = \frac{2}{3} E_{EX} (D_x^2 + D_y^2 + D_z^2) \quad (5.40)$$

where E_{EX} is the excitation energy in Hartrees.

5.5.1. Parameters Used in Calculations

The StoBe calculation requires a number of parameters as input. The most important part of the input file is the set of xyz coordinates of the atoms in the molecule. This study uses the atomic coordinates that had been previously determined using X-ray diffraction,⁴ and so the resulting density of states and XAS calculations represent the molecule as it was measured, in the solid form. Sample input files are included in Appendix A.

The only structural optimization that was performed was used to position the hydrogen atoms in the structures, as these sites cannot be detected by X-ray diffraction and were

added afterward. Although the isolated molecule was used in the calculations, necessarily neglecting intermolecular effects, this limitation is not expected to have a significant effect on the calculated spectrum. Experimental evidence has shown that the effects of these interactions are mostly limited to the broadening of features, particularly those involved with Rydberg transitions, rather than a shift in the relative energies of the spectral features.^{39,40} It is these energies with which this study is largely concerned.

The convergence criteria used in the density of states (DOS) and XAS calculations in this study were quite stringent. Two criteria were used, one governing the minimum difference between the energies of successive iterations, and one governing the difference between successive densities. For convergence to be achieved, both convergence criteria must be satisfied for three successive iterations. In both cases, the threshold was set at 1×10^{-6} Hartrees for both the energy and density convergence.

Triple-Zeta Huzinaga orbital basis sets were used in the DOS calculations in this study, along with A5 auxiliary basis sets. For the XAS calculations, a large `iii_iglo` orbital basis set^{36,38,41} was used to describe the transition site. A large augmentation basis set, containing over one hundred diffuse functions centred on the excitation site, was also added to model the unoccupied orbitals.

As was discussed above, the XAS calculations are performed on a transition state with a half-occupied core hole. In order to ensure that the core hole is localized on a specific atom, the other sites of the same element must be represented by what is called a pseudopotential. The pseudopotential combines the nuclear charge of the atom with those of its innermost electrons, the 1s electrons in the case C, N, and O sites. The remaining electrons are constrained to have the same symmetry as would the outer electrons of the atom. This representation assumes that the tightly bound electrons that are replaced in the pseudopotential model do not interact with the other sites in the molecule. This appears to be a valid assumption, due to the localized nature of the 1s orbitals.

Several other parameters can be adjusted to optimize the StoBe calculations; most of them simply affect the rate of convergence and will not be discussed here. It is, however, worthwhile to discuss one of these parameters, known as the direct inversion of iterative subspace (DIIS) parameter.³¹ The DIIS option accelerates conversion by applying an algorithm that uses the results of a given number of previous iterations to better predict the form of the density matrix to be used in the next calculation. The option was not used in the majority of the calculations presented here, as it could not be used in the calculations of all spectra because of uncertainty about its effect on the result. The StoBe output files contain a summary of the results of each iteration of the calculation. In some cases the column devoted to the DIIS error did not converge to a value of zero, suggesting that the DIIS had caused the calculation become stuck on a false solution, one with a higher energy than the ground state of the system.⁴² The spectra that exhibited this error had to be recalculated with the DIIS option off, and so it was decided that the spectra of all of the sites should be calculated in this way, for the sake of uniformity. The only exceptions to this rule are the calculations of the XAS spectra associated with the Fe₂ and Fe₃ sites, which will be discussed in Section 9.4. The calculations of these two spectra could not be made to converge without the DIIS option, but the DIIS error did not go to zero when energy convergence was achieved. As will be shown in Section 9.4, this difficulty seems to have had a negligible effect on the calculated spectra, although it necessarily introduced a degree of uncertainty into the analysis.

6. FERROCENE-PEPTIDE CONJUGATES

A series of novel ferrocene-peptide conjugates have been prepared by Dr. Kraatz's group in the Department of Chemistry at the University of Saskatchewan. These samples consist of a sequence of amino acids attached to a ferrocene molecule at one end, and terminated at the other end by one of several other molecules. They display unique electronic properties that may lead to better understanding of the mechanisms by which electrons are transferred in biological systems. The preparation, structure and properties of ferrocene-peptide conjugates have been presented in a number of publications;^{2-4,6,7,43-49} the present discussion is intended to be a brief introduction to the samples that were analyzed in this study.

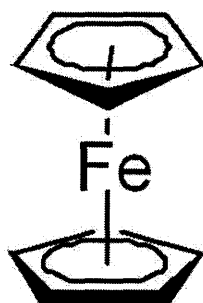


Figure 6.1 The molecular structure of ferrocene (Cp-Fe-Cp, Fe(C₅H₅)₂). The Fe atom is located at the "waist" of the molecule, and is bonded to the two Cp ligands.

To begin, it is helpful to describe the individual structures that make up the ferrocene-peptide conjugates. The structure of ferrocene (Fc) is shown in Figure 6.1. The ferrocene molecule is a "sandwich-type" molecule, composed of an iron atom sandwiched between two five-membered hydrocarbon rings, called cyclopentadienyl (Cp) rings. Compounds of Fc can be made by replacing one or more of the hydrogen atoms with a substituent molecule. The most basic structure that is examined in this

study is ferrocene carboxylic acid (Fc-COOH), where the carbon atom in the acid is attached to one of the Cp rings. The two oxygen sites in Fc-COOH- are in different bonding environments, one single-bonded to both the carbon and the hydrogen, the other double-bonded to the carbon. This molecule is used as the basis for the larger molecules.

Peptides are composed of amino acids, which are the building blocks of proteins and are, therefore, important in many biological processes. All amino acids have a common structure as their foundation; the molecules are differentiated by the structure of their sidechains. The most basic amino acid, glycine, has only a hydrogen as a sidechain, and is therefore a useful starting point for the discussion of the more complex structures. The structures of three amino acids that are important in the current study are shown in Figure 6.2. Because carbon is so ubiquitous in biological samples, by convention it is not labeled in schematic diagrams like the ones in Figure 6.2. Carbon atoms are found at every bond intersection that is not otherwise labeled. The positions of the hydrogen atoms that are attached to the carbon sites are also not traditionally shown in this sort of diagram.

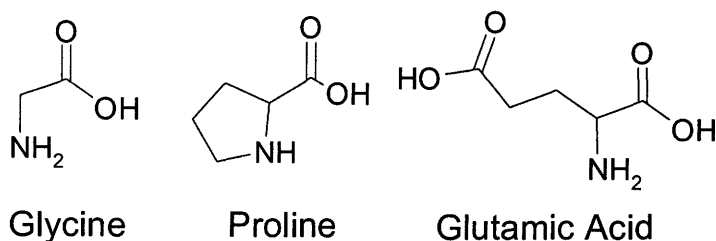


Figure 6.2. The structures of three amino acid monomers. Hydrogen atoms are omitted for clarity.

The amino acids that make up the peptide are referred to as residues in this context. In this experiment, all of the residues in a given peptide are of the same amino acid. The C-terminus (the carbon atom that is double-bonded to an oxygen atom in all acids) of one amino acid has its OH group removed, and it is then bonded in place of one of the hydrogen atoms that is attached to the N-terminus (the nitrogen atom found in all acids) of the next. The N-C bond is referred to as the peptide or amide bond and has a

unique character that will be explored when the experimental data are examined. Peptides formed from Glu have a different structure, as there are two separate OH groups that can be removed and attached to the N-terminus of another residue. Peptides formed in this way have a branching, or dendritic structure.

The majority of the analysis in this study is concerned with the study of the series Fc-Pro_x-OBz (x=1-4), which does not have a dendritic structure. The N-terminus of the peptide is attached in place of the OH group of Fc-COOH, and its C-terminus is capped with a benzyl ester.

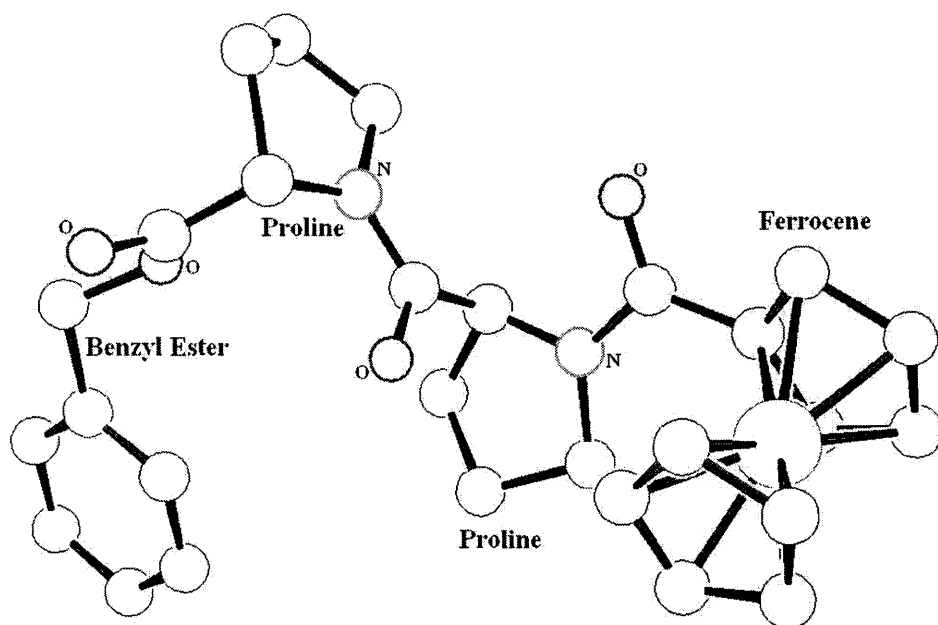


Figure 6.3. Ortep drawing of the molecular structure of Fc-Pro₂-OBz with the component groups labeled. The oxygen and nitrogen sites are also labeled.

The benzyl ester (designated OBz) is simply a benzene ring (C₆H₆) that has had a substituent, composed of a carbon atom and an oxygen atom, attached in place of one of the H sites. The carbon atom is attached directly to the benzene ring, and the oxygen atom is single-bonded to both the carbon atom and the C-terminus of the peptide. The structure⁴ of Fc-Pro₂-OBz, plotted using Ortep-3,⁵⁰ is shown in Figure 6.3

with the important components labeled. The hydrogen atoms have been omitted for simplicity. The modified peptide exhibits a helical structure, one turn of which is completed when three proline residues are included. Three of the four oxygen atoms in Fc-Pro₂-OBz are double-bonded to the adjacent carbon site. These carbonyl groups have a unique spectroscopic signature that is prominently involved in the analysis of the XAS data obtained in this study.

The motivation for studying these unique structures lies in their unusual electrical properties. Cyclic voltammetry (CV) studies have shown that the potential that is needed to transfer an electron from the ferrocene (oxidation) to the benzene (reduction) is linked to the number of proline residues included in the peptide.⁴ The fact that these two quantities are related is not unexpected; rather it is the nature of their relation that is unusual. In general, the reduction-oxidation (redox) potential would be expected to increase as the distance between the electron donor (Fc, in this case) and acceptor (OBz) increases. However, the CV measurements suggest that, rather than becoming more difficult to oxidize, the increase in the number of proline residues made the redox reaction easier to perform. If an explanation for this unusual behaviour can be found, it may provide a basis for understanding the electron transfer reactions that occur in larger peptides and proteins, processes which are involved in many natural processes, such as photosynthesis.¹

7. SAMPLE PREPARATION

If meaningful data are to be obtained, it is important to mount the samples in such a way that the effects of charging and contamination are minimized. In this study multiple samples were mounted one above another on the same sample plate, and so particular attention needed to be paid to the latter concern. Because the ferrocene-peptide conjugates are in the form of either powders or thin needles,⁴ it was necessary that they be adhered to the holder in such a way that none of the material could detach itself and contaminate the adjacent samples.

Several preparation techniques were tried and rejected before the best method was found. The clearest and most trustworthy measurements are obtained when the sample is dissolved in a small amount of ethyl alcohol, and the resulting paste is spread as thinly as possible onto a piece of indium foil. The alcohol evaporates rapidly, and any excess material is shaken from the holder, taking care not to contaminate the adjacent sites. The thin film that is the product of this procedure is firmly attached to the holder and allows electrons that are removed during measurements to be easily replaced by those from the indium foil.

8. CALIBRATION AND NORMALIZATION

In soft X-ray absorption and emission spectroscopy, it is important that the energy scales of measurements made at different times agree with each other. Because the various components of beamlines and endstations are not static and there is a degree of backlash whenever they are moved, the exact experimental geometry for a certain measurement cannot be reproduced consistently, leading to small shifts in the measured photon energies. Fortunately, this difficulty can be overcome by measuring the spectra of a reference sample every time a set of measurements is performed on a sample of interest. The reference spectra have readily identifiable features that correspond to established values of excitation energy (for XAS) and emission energy (for XES). The energy scale of the reference spectra can then be shifted to correspond with the absolute scale; the energy scales of the samples' spectra are shifted by the same amount. Table 8.1 lists the samples that were used for calibration of energy scales in this project along with the energy levels of their characteristic features.

Table 8.1: Calibration samples for soft X-ray absorption (XAS) and emission (XES) spectroscopy. Energy values correspond to the position of prominent features in the reference spectra.

Sample	Edge	XAS Energy (eV)	XES Energy (eV)
HOPG (highly-oriented pyrolytic graphite)	C 1s	285.4 ⁵¹	277.0 ⁵²
hBN (hexagonal Boron-Nitride)	N 1s	402.1 ⁵³	394.7 ⁵³
BGO (Bi ₄ Ge ₃ O ₁₂)	O 1s	532.7 ^{54,55}	526.4 ^{54,55}
Fe Metal	Fe 2p		705.0 ⁵⁶
Ferrocene	Fe 2p	709.1 ⁵⁷	

As an example, the absorption spectrum of hexagonal Boron-Nitride (hBN), used for calibration of N 1s spectra, is shown in Figure 8.1. In this instance, the energy scale needed to be shifted 2.9 eV so that the N 1s \rightarrow π^* feature was found at the correct energy.⁵³ The amount by which the spectra need to be shifted differs from experiment to experiment, and so it is necessary to measure a reference spectrum whenever a set of

measurements is performed at a particular edge. For completeness, the calibration of the hBN N $K\alpha$ XES spectrum is shown in Figure 8.2.

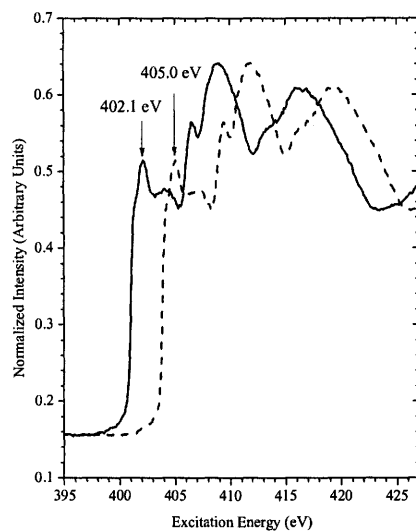


Figure 8.1. Calibrated (solid) and uncalibrated (dashed) N 1s XAS spectra of reference sample hBN.

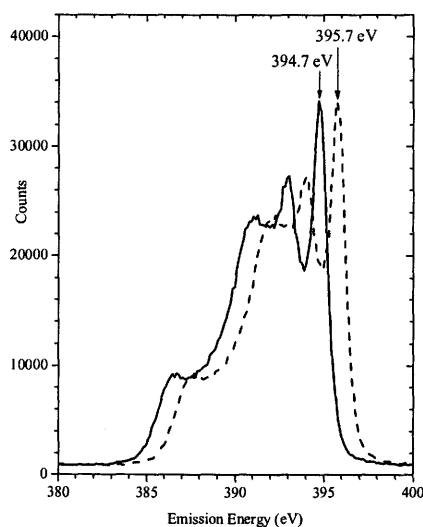


Figure 8.2. Calibrated (solid) and uncalibrated (dashed) N $K\alpha$ XES spectra of reference sample hBN.

In addition to the changes that must be made to the energy axes of the as-measured data, the intensity of the spectra must also be conditioned to reflect the true nature of the transitions being probed. The intensity of the measured transition, be it in an absorption or an emission spectrum, is affected by the intensity of the incoming X-rays. As was discussed in Section 3, the X-rays are monitored by measuring the photoionization current produced in a sample of gold. At Beamline 8.0.1, a highly transparent gold mesh is used to measure the number of incoming photons while the measurement is being performed, while a separate measurement of the intensity is needed at Beamline 6.3.2.

In both cases, the measured XAS spectrum is divided by the energy-dependent current that is measured from the gold sample, in order to provide a representation of the absorption profile relative to the intensity of the incoming radiation. To reflect the fact that the measurements gold and sample currents are not performed concurrently, the normalization of the Beamline 6.3.2 data is a two-step process. Before the normalization is performed, both the absorption spectrum and the gold sample current are divided by the energy-dependent current that is measured from mirror M3, shown in Figure 3.5. The measurement of the mirror current is performed at the same time as the spectra it is used to normalize, and therefore provides an intensity measurement of the incoming photons.

Because all of the parameters involved are proportional to the quantity that they are being used to represent, rather than being exact numerical measurements, the intensities of the resulting normalized spectra are displayed using arbitrary units. This convention reflects the fact that no attempt has been made to scale the results in such a way as to reflect the absolute absorption coefficient of the material. For the purposes of comparative analysis, such scaling is unnecessary.

9. EXPERIMENTAL AND THEORETICAL XAS SPECTRA

A number of soft X-ray spectroscopy studies of the electronic structure of amino acids have recently been published. These studies have taken a number of different approaches, including purely experimental,⁵⁸⁻⁶⁰ purely theoretical,^{61,62} and combinations of theory and experiment.^{40,63-68} The majority of these studies^{40,59,60,64,65,67,68} have been concerned with the study of glycine, the most basic amino acid, while others have studied the electronic structures of a number of samples.^{58,61-63,66} Zubavichus *et al.* have also studied the effects of radiation damage on the spectra of amino acids,^{69,70} an effect which is also discussed briefly in this study (Section 9.5). A summary of the previous studies is tabulated in Appendix F. The electronic structure of ferrocene^{57,71-73} has been studied using electron energy loss spectroscopy (EELS), which provides much the same information as soft X-ray spectroscopy. All of these studies provide valuable information about the behaviour of the individual components of the structures with which this study is concerned, which will help analyze the spectra of the larger molecules. This study is the first known attempt to provide a combined theoretical and experimental spectroscopic examination of modified peptides, and is also the only such study of ferrocene molecules that have been modified by the attachment of extremely large substituents.

9.1. C 1s XAS Spectra

Carbon is the most abundant element in the Fc-peptide samples, forming the main structure of the molecule. In electron transfer reactions, an electron from the donor molecule (the ferrocene) moves to the acceptor molecule (benzene). Both of these components are primarily composed of C atoms, and so the C 1s spectra are of great interest. The spectra of the structures Fc-Pro_x-OBz will be studied in detail, with comparisons to other Fc-peptides included where appropriate.

9.1.1. Experimental C 1s XAS Spectra

The C 1s spectra of the Fc-peptide samples can largely be analyzed by viewing them as the superposition of the spectra of ferrocene, amino acids, and whatever molecule is used to protect the carbonyl terminus of the peptide. In the case of the Fc-Pro_x-OBz series, this molecule is the benzyl ester. Figure 9.1 shows the C 1s XAS spectrum of Fc-Pro₁-OBz, which is representative of the Fc-Pro_x-OBz series as a whole. The labels on the main spectral features indicate the identity of the final-state unoccupied orbital associated with that feature.

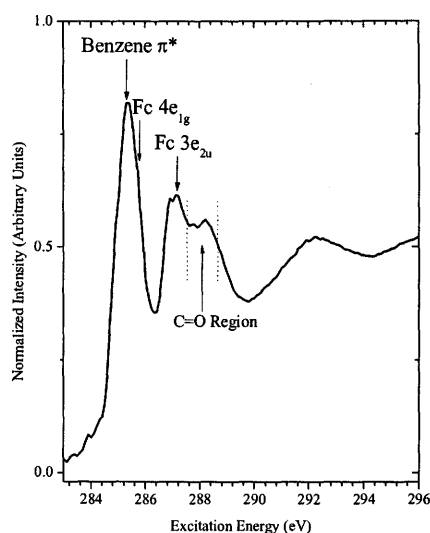


Figure 9.1. The C 1s XAS spectrum of Fc-Pro₁-OBz measured at Beamline 6.3.2 at the ALS. The important spectral features that are discussed in the text are labeled. The region marked "C=O" represents the energy range (287.5 eV - 288.6 eV) of the carbonyl resonance features in the spectra of the Fc-Pro_x-OBz series.

Note that because the Fc-peptides in this study do not belong to any simple space groups it is not possible to give accurate, descriptive names to their molecular orbitals. By convention, the orbitals will be described using names that correspond to the MOs that would be found in the gaseous form of the component in question. For example, the benzene π^* orbital is found in gaseous benzene; the lack of symmetry in the extended structure technically renders even this simple label inaccurate. Nevertheless,

the label will be preserved, as it is preferable to referring to the orbitals by the proper, generic labels 1A, 2A, etc. It will be shown that, in most cases, these orbitals are modified to some degree by intramolecular interactions, although these changes are on a strictly perturbative level, and so the labels used will retain their physical significance in the vicinity of the component in question, although this is not necessarily true in the case of the extended orbitals that will be discussed in many of the following sections.

The spectrum of Fc-Pro₁-OBz is dominated by the low-energy feature around 285.5 eV. Comparison with previous studies suggests that this large feature is actually produced by transitions into two distinct final states: the benzene π^* ⁷⁴ (~285.3 eV) and Fc 4e_{1g}⁷² (~285.7 eV) molecular orbitals. We will see later that the energies given for these features are, by necessity, only approximate, as they involve multiple transitions between non-degenerate levels. This property is suggested by the spectrum in Figure 9.1, which exhibits a number of shoulders on both the high- and low-energy sides of the 285.5 eV peak. These features are in agreement with the results previously reported in studies of substituted ferrocenes⁵⁷ and benzaldehyde.⁷⁵ Benzaldehyde is a similar molecule to the benzyl ester that is found in the Fc-Pro_x-OBz samples, although the benzaldehyde oxygen site is double-bonded to the adjacent carbon, as opposed to the single-bond found in the benzyl ester.

Continuing toward higher energy, the next major transition is also associated with the ferrocene moiety. It is associated with transitions into the 3e_{2u} MO,⁷² which is closely associated with the π^* orbitals of the Cp rings, as opposed to the aforementioned 4e_{1g} MO, which has a larger contribution from the unoccupied Fe 3d orbitals. There is a considerable amount of fine structure in this region, which cannot be fully appreciated in Figure 9.1, due to the large energy range of the plot. Figure 9.2 shows a close up view of the 3e_{2u} region and the 'C=O' region, which will be discussed in detail later on. The inset in Figure 9.2 shows the location of the energy window of the main figure relative to the spectrum of Fc-Pro₁-OBz.

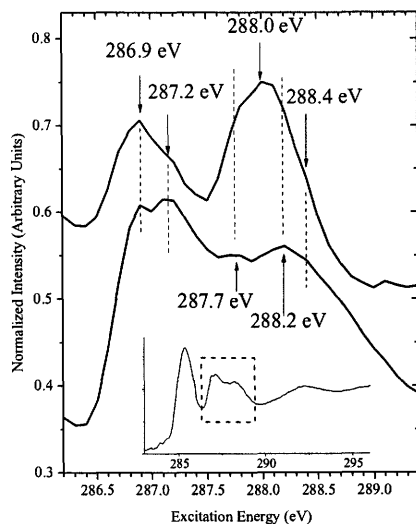


Figure 9.2. Close-up of the C 1s XAS spectra of Fc-Pro₃-OBz (top) and Fc-Pro₁-OBz (bottom). The positions of the significant features of each spectrum are marked with arrows; the dotted lines have been added to aid in the comparison of the spectra. The inset shows the spectrum of Fc-Pro₁-OBz with a box around the energy region that is shown in the main figure.

Figure 9.2 shows two distinct features in the region around the expected position of the $3e_{2u}$ molecular orbital. If only the measured spectrum is examined, it cannot be determined whether these transitions represent a splitting of the $3e_{2u}$ orbital or if the transitions are associated with two separate final states. The presence of the substituent could cause a break in the degeneracy of the orbitals; previous studies have shown small (on the order of 0.1 eV) shifts when the spectra of substituted and unsubstituted ferrocenes are compared.^{57,72} The measurements in those previous studies were performed on gas-phase samples using EELS, a technique in which the resolving power is generally worse than in XAS, and so it is possible that two separate, non-degenerate transitions appeared as a single resonance feature. It must also be noted that there is a shoulder on the low-energy side of the feature (around 286.5 eV), which cannot be explained through comparison with previous studies, although its origin becomes clear upon examination of the calculated spectra presented in Section 9.1.2.

The region from 287.5 eV to 288.6 eV contains a number of features, most of which are due to transitions into the π^* orbitals associated with the carbon-oxygen double

bonds in the peptide's carbonyl groups. Transitions in this energy region are found in the spectra of all amino acids, and, for the monomer the location of the resonance does not vary by a great amount from acid to acid.⁶³ Studies have shown, however, that the position of the peak is dependent on the bonding environment of the carbon. In the specific case of amino acid spectra, there is considerable experimental evidence that shows that there is a shift to lower energies (approximately 0.3-0.4 eV) when a peptide bond between two amino acids is formed.^{58-60,67} This observed shift agrees with the general environment-dependent behaviour of carbonyl C 1s→ π^* transitions, which have been shown to vary in position by as much as 3.8 eV.⁷⁶ This variation is attributed to changes in the energies of both the core and final state carbon orbitals, which are dependent on the nature of the structure to which the carbon is attached. More specifically, the position of the peak is related to the electronegativity of the nearby structures; the more electronegative the environment is, the higher the energy of the peak will be. With this relationship in mind, it is suggested that the 288.2 eV feature in the spectrum of Fc-Pro₁-OBz can be attributed to transitions into the π^* orbitals associated with the carbonyl group at the C-terminus of the proline.

If the 288.2 eV feature is thus assigned, then the feature associated with the carbonyl group that is adjacent to the ferrocene must occur at a lower energy. For convenience, this location will be referred to as the ferrocene carbonyl. Close examination of the spectra in Figure 9.2 suggests that the feature labeled 287.7 eV is actually composed of multiple transitions, seen as a series of shoulders on the low-energy side of the 288.0 eV peak. It is likely that one of these features is associated with the ferrocene carbonyl group, although a firm assignment cannot be made at this time. Less ambiguous is the assignment of the 288.0 eV feature in the spectrum of Fc-Pro₃-OBz. This peak is present in the entire Fc-Pro_x-OBz series (x=2-4) and is associated with the carbonyl group that is located at the peptide bond.

The origins of the remaining contributions to the feature at 287.7 eV in the Fc-Pro₁-OBz spectrum are also difficult to determine. Previous studies have shown that the absorption spectrum of benzaldehyde has a feature at this energy, which was attributed to the bond that is formed between the benzene ring and its attached

substituent.⁷⁵ However, the spectrum of proline also exhibits a peak at this energy, attributed to transitions into σ^* orbitals that are the result of C-H bonds in the prolines⁶³. Analogous features appear as shoulders in the C 1s spectra of the larger peptide samples in this study, as is evident from the spectrum of Fc-Pro₃-OBz in Figure 9.2. There are also numerous shoulders on the high-energy side of the C=O region that cannot be easily explained by simply comparing the spectra with those of the constituents, although some of the structure is likely associated with the benzyl ester, which is expected to have a π^* feature in this region.⁷⁵

To supplement the comparison with the spectra in the literature, the assignment of spectral features can be clarified by comparing the spectra of the Fc-Pro_x-OBz series with the spectra of some related samples. Figure 9.3 shows the spectra of Fc-Pro₁-OBz on the same axes as that of Fc-COOH. As the Fc-COOH molecule does not contain a benzyl ester, the position of the main resonance around 285.5 eV occurs at a higher energy, due to the absence of the 285.3 eV resonance associated with the missing molecule. The peak in the Fc-COOH XAS spectrum is located at 285.7 eV, in agreement with the assumed location of the $4e_{1g}$ feature in the spectrum of the Fc-Pro₁-OBz (Figure 9.1).⁷² The other main characteristic of ferrocene C 1s XAS absorption spectra, the $3e_{2u}$ -like transition around 287 eV, is also retained. This feature is not split in the way that the corresponding feature in the Fc-Pro₁-OBz spectrum is, suggesting that the lower-energy (286.9 eV) feature is associated with either the proline or the benzyl ester. The Fc-COOH spectrum also exhibits the previously mentioned shoulder around 286.5 eV, although it is an extremely minor contribution.

The Fc-COOH spectrum also exhibits a peak (288.5 eV) that is associated with the carboxyl group. The peak is found at a higher energy than the 288.2 eV peak in the Fc-Pro₁-OBz spectrum. This shift is in keeping with the relationship shown by Urquhart and Ade,⁷⁶ as the carbonyl is attached to an oxygen atom in Fc-COOH and to a nitrogen atom in Fc-Pro₁-OBz.

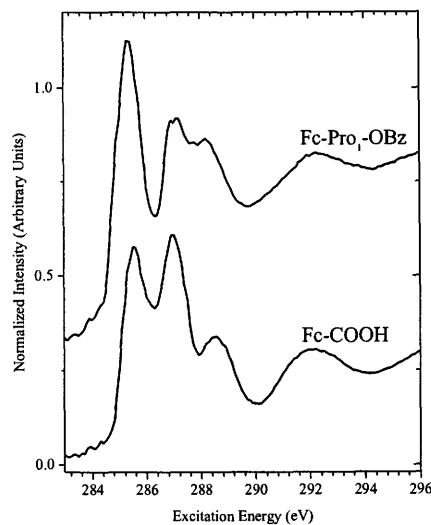


Figure 9.3. Comparison of the C 1s XAS spectra of Fc-Pro₁-OBz (top) and Fc-COOH (bottom) measured at Beamline 6.3.2 at the ALS. Spectra have had background subtracted and have been offset vertically for clarity.

Valuable insight into the regions of the C 1s XAS spectra that are associated with the $3e_{2u}$ -like final state can be gained by comparing the spectrum of Fc-COOH with that of the disubstituted sample Fc-(COOH)₂. The latter sample has a carboxylic acid substituent on each of the Cp rings of the ferrocene. Given this molecular structure, it would be expected that the spectral changes caused by the presence of the substituent would be magnified. The experimental data suggest that this is, indeed, the case. The spectra shown in Figure 9.4 were measured at Beamline 8.0.1 of the ALS, and were normalized to a uniform intensity at approximately 305 eV. The spectrum of Fc-COOH looks slightly different than that which was measured at Beamline 6.3.2 (Figure 9.3), but the features in the region of interest are represented in both spectra. The feature labeled 'a' (286.6 eV) corresponds in energy to the shoulder that was seen in the spectra in Figure 9.3, and feature 'b' corresponds to the 287.2 eV feature. It is quite apparent that the intensity of feature 'a' is increased upon the addition of the second substituent, while feature 'b' becomes less distinct and may undergo a shift to higher energy, although the shape of the spectrum makes it difficult to verify this last point. The behaviour of the spectra in this region suggests that feature 'a' is

characteristic of substituted Cp rings, and feature 'b' is characteristic of unsubstituted rings. As feature 'b' is found at an energy consistent with that of the $3e_{2u}$ orbital,^{57,72} this observation seems valid, and it will be shown that it is consistent with the predictions of the StoBe calculations.

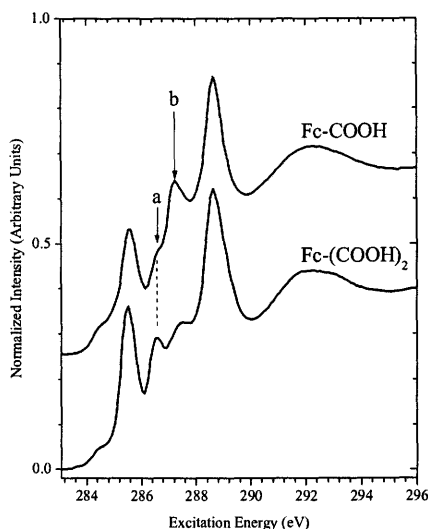


Figure 9.4. The C 1s XAS spectra of Fc-COOH and Fc-(COOH)₂.

The spectra of the entire Fc-Pro_x-OBz series are shown in Figure 9.5. The ratio of the peak intensity of the main Benzene/ $4e_{1g}$ feature to that of the $3e_{2u}$ feature remains effectively constant throughout the series, and there are no discernible shifts in the energy levels of these features. These two observations suggest that the electronic structure of the ferrocene moiety does not change significantly as a function of the number of proline residues that are attached.

The intensity of the resonance feature associated with the peptide bond increases, as expected, when more proline residues are added. The position of the peak does not change as a function of the number of residues in the peptide. While no firm conclusions can be drawn from this observation, it is possible that, even at relatively large separations, the ferrocene affects the electronegativity of the peptide. The location of the resonance is lower than that which would be found in unmodified

peptides, suggesting that the carbonyls involved in the peptide bonding are in a more electropositive environment than would be expected.

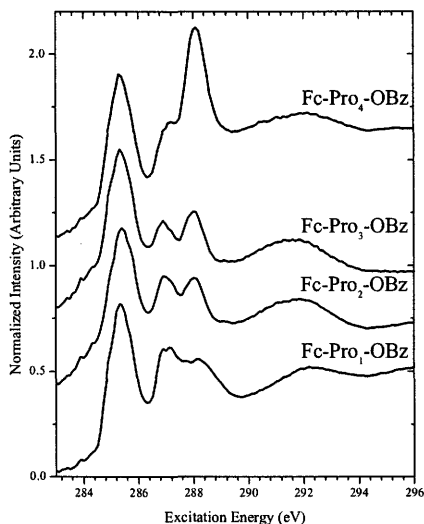


Figure 9.5. The C 1s XAS spectra of Fc-Pro_x-OBz ($x=1-4$) measured at Beamline 6.3.2 at the ALS. Spectra have had background subtracted and have been offset vertically for clarity.

The general behaviour of the spectra in Figure 9.5 is reproduced in the XAS spectra of other Fc-peptide samples. The trend in the carbonyl π^* peak is much more pronounced in the C 1s absorption spectra of Ferrocene-glutamic acid compounds (Figure 9.6), due to their dendritic structure. The upper spectrum has contributions from fifteen C=O bonds, as opposed to three in the spectrum of Fc-glu-(OH)₂.

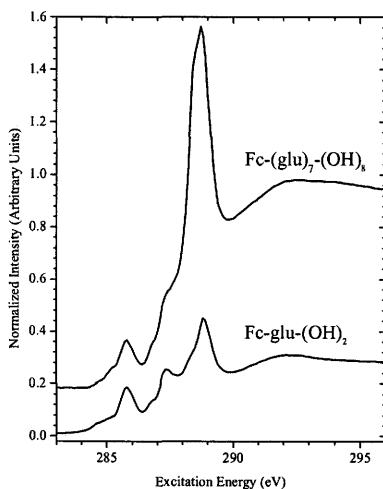


Figure 9.6. C 1s XAS spectra of Fc-(glu)-(OH)₂ and Fc-(glu)₇-(OH)₈

9.1.2. StoBe C 1s XAS Spectra

The C 1s absorption spectrum of each individual site in Fc-Pro₂-OBz was calculated separately, and the results were added together to simulate the absorption spectrum of the entire molecule. Performing the calculations in this way allows the contribution of each individual site to be determined separately, allowing for unambiguous assignment of the spectral features seen in the measured spectra.

All of the DFT simulations of the electronic structure of Fc-Pro₂-OBz were calculated using the geometry that was determined by X-ray diffraction.⁴ For reference purposes, a StoBe input file including the xyz atomic coordinates is included in Appendix A. The atomic coordinates that were used for the Fc-COOH calculations were created by modifying the Fc-Pro₂-OBz structure; the extended peptide structure was replaced by an OH group, and a geometry optimization was performed using Spartan. A sample input file for this molecule is also included in Appendix A.

Some difficulties were encountered when performing the calculations. For some sites, particularly in the aromatic ring structures, overlapping basis sets caused a computational problem that led to erroneous results.⁴² At the suggestion of StoBe author Lars Pettersson, this problem was eliminated by the substitution of smaller A2 auxiliary basis sets in the calculation. Unfortunately, time constraints made it impossible to recalculate all sites with the smaller basis sets, as the calculation for each site requires approximately 1.5 days to converge. Fortunately, the size of the auxiliary basis sets appears to have only a negligible effect on the calculated spectra, and so these results are compared alongside those involving the larger A5 basis sets.

A problem that could not be so easily overcome involved the calculation of the spectrum associated with site C21, the carbon site at the C-terminus of the peptide. This carbonyl site is expected to have a significant contribution to the overall spectrum. For reasons that have not been determined, the calculations for this site could not be made to converge. Attempts to correct this problem involved variation of every meaningful parameter, including basis sets, exchange-correlation potential models, DIIS values, and dmixing levels, all to no avail. Convergence was finally

achieved when the ferrocene moiety was removed from the structure and replaced by an OH group. As expected, the resulting spectrum shows a strong π^* feature in the general vicinity of the other carbonyl peaks. However, the energy of the peak as calculated was approximately 1 eV higher than the other two carbonyl sites (C11 and C16), which does not agree with the measured spectra. As a result, the energy axis of the C21 spectrum has been shifted in all spectra to more closely resemble the measured spectra. To signify that the spectrum is not displayed as calculated, it is shown as a dashed line, while the other spectra will be displayed as solid lines. On a positive note, the apparent increase in the energy of this transition suggests that the previously mentioned effect of the ferrocene on the peptide, namely decreasing its electronegativity, may be valid.

Because the spectrum of each part of the molecule uniquely contributes to the overall spectrum, extremely valuable information can be obtained by examining each section separately. The carbon sites are numbered according to their positions in the molecule; the numbering scheme is shown on the schematic diagram of Fc-Pro₂-OBz in Figure 9.7. In the following discussion, the sites found in the ferrocene, the proline residues, and the benzyl ester will be discussed separately. A plot of the individual site-resolved C 1s XAS spectra on a common energy axis is provided in Appendix B.

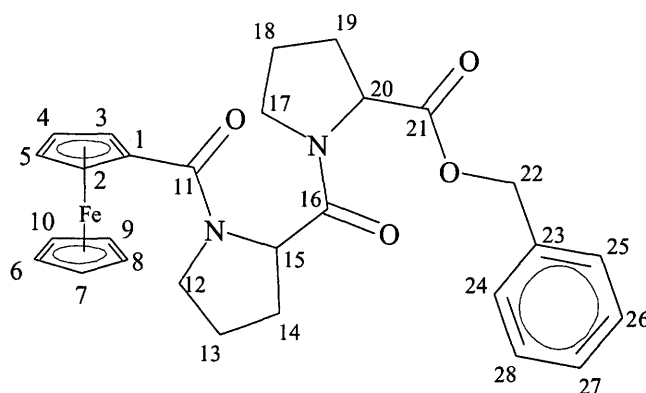


Figure 9.7. The structure of Fc-Pro₂-OBz, showing the labeling scheme used to identify the carbon sites.

The spectra associated with the individual carbon sites in the ferrocene moiety (including the carbonyl site adjacent to the ferrocene, C11) are shown in Figure 9.8. As expected the spectra of the Cp ring sites have prominent low-energy peaks, ranging in energy from 285.2 eV to 285.8 eV, that are assumed to involve transitions into the $4e_{1g}$ -like orbital discussed in the experimental section. The variation in the energy of the peak arises from the differences in the energy of the 1s core level among the various sites. In order to confirm that the transitions involve a common final state, the term value of the feature is examined. The term value is calculated by subtracting the transition energy from the ionization potential of the associated core electron, providing an indication of the energy of the final state with respect to the continuum.

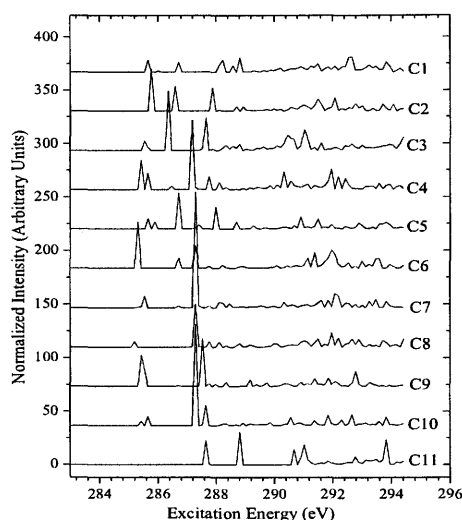


Figure 9.8. C 1s XAS spectra of the ferrocene sites in Fc-Pro₂-OBz as calculated using StoBe. A vertical offset is added for clarity.

The average term value for the lowest-energy transition in Figure 9.8 is 5.46 eV, which does not agree with those found by Wen *et al.*⁵⁷ which ranged from 4.3 eV for unsubstituted ferrocene to 4.5 eV for Fc-C₂H₃. However, the above term values were calculated using the calibrated absorption spectra; if the 1.2 eV shift that was applied to each spectrum is taken into account, then the average value (4.26 eV) is in agreement with the published results. This suggests that the core level energies given

by the StoBe calculations are approximately 1.2 eV too low, while the unoccupied levels are consistent with the physical system. The term values that take the effect of the shift into account will be considered to be correct, with the graph-based values included in parentheses in Table 9.1. In all further discussions of the term values, the values derived from the shifted features will be omitted.

In addition to the lowest-energy transition, several of the spectra, most notably those corresponding to the C4, C5, and C10 sites, exhibit a second feature at a slightly higher energy. Closer inspection shows that the C1, C6, and C7 spectra also have similar contributions, although they are comparatively minor. These six peaks have an average term value of 4.03 eV, which is similar to that of the previously discussed transition. The study by Wen *et al.*⁵⁷ notes that although splitting of the $4e_{1g}$ orbital is expected in substituted ferrocene, they found no evidence of it in their data. It seems apparent that the feature that is currently under discussion can be attributed to such a splitting, and that the lack of experimental evidence is the result of the overlapping of this feature with the other transitions in the region. The peak positions in the calculated spectra range from 285.5 eV to 286.0 eV, a region that is encompassed by the prominent resonance seen in this region of the measured spectra (Figure 9.5). The two non-degenerate $4e_{1g}$ -like orbitals will be referred to as the $4e_{1g}'$ and $4e_{1g}''$ orbitals, in order of ascending transition energy.

Examination of the StoBe output files shows that the transition into the $4e_{1g}''$ orbital is present in all calculated spectra, although the oscillator strengths are extremely low in some cases. The values in Table 9.1 are calculated using only the spectra where the transition is visible. The core levels, peak locations, and term values for this orbital, as well as all notable higher-energy orbitals associated with the ferrocene, are given as an average of the values associated with each site. The values for each individual site are included in Appendix C.

There are other prominent contributions to the C 1s XAS spectrum associated with the Cp ring sites. Recalling that the sites C1-C5 are associated with the substituted Cp ring (Cp'), the calculations shown in Figure 9.8 suggest that the $3e_{2u}$ -like orbital

(~287.2 eV) is split under the influence of the substituent. The sites C1-C5 have a prominent feature at approximately 286.5 eV, corresponding closely in energy to the transition labeled 'a' in Figure 9.4. A very minor increase in intensity is also seen around this energy in the spectra of C6, C7, and C9, although the average term value for these features is slightly lower (2.97 eV) than for the Cp' features. The assignment of all of the transitions in this region to one orbital, which will be assumed to be $3e_{2u}$ -like and referred to as $3e_{2u}'$, is supported by the similarities in the term values. The difference between the term values of the features seen in the unsubstituted cyclopentadienyl ring (which will be referred to as Cp'') and Cp' spectra is likely due to changes in the core hole relaxation effect, brought about by the change in environment introduced by the substituent. If the peaks in the spectra that are associated with Cp'' ring are neglected, the average term value for this feature is 3.34 eV, which is higher than the values found by Wen *et al.*⁵⁷ for the $3e_{2u}$ orbital (2.91 eV for Fc-C₂H₃, 2.82 for Fc and Fc-C₄H₉). Including the Cp'' sites lowers the average value (3.20 eV) but does not bring it into agreement with the previous work. It will be shown shortly that the source of this disagreement can be easily understood.

The next-highest-energy peaks in the spectra of sites C4-C10 have an average energy of 287.3 eV, with an average term value of 2.36 eV. The transitions associated with sites C4 and C5 have a term value that is, on average, 0.23 eV higher than the sites on the unsubstituted ring, suggesting there is a substituent-influenced relaxation effect involved in this orbital as well. Therefore, the energies shown in Table 9.1 do not take these two transitions into account, as they can be considered to belong to a different system. Because the average energy of these features closely resembles that of feature 'b' in Figure 9.4 (287.2 eV), they will also be assumed to involve a $3e_{2u}$ -like final state, denoted $3e_{2u}''$. If the term values of all of the peaks associated with these two $3e_{2u}$ -like states are included, the average term value is 2.79 eV, in close agreement with the previous study. This agreement suggests that the single features observed previously were, in fact, the result of the superposition of non-degenerate $3e_{2u}$ -like states.

The spectrum of the substituent carbon site, C11, has a peak at 288.8 eV with a term value of 3.41 eV. The term value is slightly above the average value for the $3e_{2u}'$

orbital, but it is within the range of the values used to calculate the average included in Table 9.1. This feature is important because it shows that the $3e_{2u}'$ orbital contributes to the electronic structure of the substituent, suggesting that it may provide a means for the electrons from the ferrocene to be transferred to the peptide, which must occur if the peptide is involved in the electron transfer from the ferrocene to the benzene ring. As will be discussed later, transitions from the metal site to $3e_{2u}$ -like orbitals necessarily involve a redistribution of charge within the ferrocene, with electrons being transferred from the metal to the Cp rings.^{57,73}

Table 9.1: Energy positions and term values for features in C 1s spectra of ferrocene sites

Site	Core Level (eV)	Feature (eV)	Term Value (eV)	Assignment
C1	291.19	285.66	4.33 (5.53)	$4e_{1g}'$
C2	291.21	285.77	4.24 (5.44)	
C3	290.96	285.54	4.22 (5.42)	
C4	290.88	285.42	4.26 (5.46)	
C5	291.16	285.66	4.31 (5.51)	
C6	290.90	285.42	4.28 (5.48)	
C7	290.82	285.42	4.19 (5.39)	
C8	290.66	285.19	4.27 (5.47)	
C9	290.91	285.42	4.29 (5.49)	
C10	290.88	285.42	4.26 (5.46)	
Site	Core Level ^a (eV)	Feature ^a (eV)	Term Value ^a (eV)	Assignment
C1,4,5 6,8,10	290.95	285.71	4.03 (5.23)	$4e_{1g}''$
C1-5	291.02	286.50	3.34 (4.54)	$3e_{2u}'$
C6-10	290.89	287.34	2.30 (3.50)	$3e_{2u}''$
C2-5	291.05	287.81	2.04 (3.24)	Cp' C-H σ^*
C6-10	290.83	288.25	1.39 (2.59)	Cp C-H σ^*
^a average value for all sites involved in transition				

The analysis of the transitions into the $4e_{1g}$ - and $3e_{2u}$ -like orbitals of this substituted ferrocene suggest that the substituent has a significant effect on the electronic structure of the Cp rings. The calculated spectra clearly show that the degeneracy of both orbitals is broken as a result of the presence of the substituent, although the specific nature of the effect differs between the two orbitals. The $3e_{2u}'$ and $3e_{2u}''$ orbitals are mostly associated with the substituted and unsubstituted Cp rings, respectively, while the two $4e_{1g}$ -like orbitals have strong contributions from both rings. The origin of this

difference may be in the different natures of the orbitals. The ferrocene $4e_{1g}$ state is mostly associated with the Fe atom; if the influence of the substituent changes the electronic structure of the atom, then this change may be reflected similarly in its interaction with both Cp rings. Conversely, the $3e_{2u}$ in an unsubstituted ferrocene is associated almost exclusively with the Cp rings, and so any changes in their electronic structure would likely be due to their immediate environment, hence the observed association of the two non-degenerate features with a particular ring.

Another set of features is seen in the region ranging from 287.6 eV to 288.4 eV of all spectra in Figure 9.8. In the measured spectra, this region is dominated by the C=O π^* transitions and so a comparison of the theoretical features with the experimental data is difficult. Valuable information can still be gained from the examination of the calculated spectra, however. The C2-C5 spectra display a prominent peak at approximately 287.8 eV (term value 2.04 eV) that is likely, given its similarity in position to the 287.7 eV feature in Figure 9.2, the result of transitions into C-H σ^* orbitals. Similar transitions are seen around 288.3 eV (average term value 1.39 eV) in the spectra associated with the Cp'' sites. These transitions may produce the feature at 288.4 eV in Figure 9.2, or may be seen in the many shoulders observed on the high-energy side of this feature.

Figure 9.9 shows the C 1s XAS spectra of the proline residues. The spectra of the individual sites are grouped according to their location in the molecule. The spectra are ordered according to the numbering scheme shown in Figure 9.7, in order to facilitate comparison between equivalent sites in adjacent proline residues. When the spectra of these nearly equivalent sites (e.g. C13 and C18) are compared, it becomes evident that there is little variation in spectral features between the two adjacent proline residues.

As would be expected from both the experimental data and from all previous XAS studies of amino acids, the dominant features in the proline spectra are those associated with the carbonyls. Sites C16 and C21 correspond to these atoms, and display a prominent peak at 287.6 eV. As was mentioned previously, the energy scale of the

C21 spectrum needed to be shifted, due to difficulties in the calculation. As a reminder, the spectrum is displayed as a dashed line. The spectrum of C15 shows a minor peak at the same energy (287.6 eV) as the carbonyl feature, which on first inspection would suggest that the two features are closely related. Examination of the term values, however, shows that this is not the case. The term value of the C=O resonance feature is 4.59 eV while the C15 feature has a term value of 3.30 eV. This term value matches that of a much less intense, higher-energy feature of the C16 spectrum, found at 288.9 eV. It should also be noted that the term value agrees with that of the $3e_{2u}'$ orbital that has been shown to be present on both the substituted Fc rings and the substituent carbon atom (C11). The similarity in term values suggests that there is an unoccupied state at seemingly constant energy, relative to the continuum, associated with every carbon site along the peptide backbone all the way from the substituted Cp ring to the C-terminus of the first proline residue, at the peptide bond.

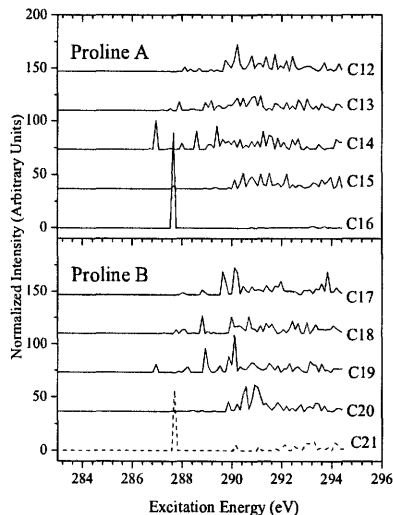


Figure 9.9. C 1s XAS spectra of the proline residues of Fc-Pro₂-OBz, calculated using StoBe. The upper window shows the spectra associated with the proline nearest the ferrocene moiety, while the lower window shows the adjacent proline. Spectra have not been normalized, and an offset has been added for clarity.

At this point, it must be noted that there is some disagreement between the experimental and theoretical spectra of the carbonyl C sites, in addition to the previously discussed difficulties associated with site C21. In the case of site C16, located at the peptide bond, the calculated energy position of the main π^* peak does not agree with the experimental data. As is shown in Figure 9.5, all of the spectra of the series Fc-Pro_x-OBz have a prominent peak at 288.0 eV, which was assumed to be associated with the carbonyl groups located at the peptide bonds. The increase in the intensity of this feature as more residues were added to the peptide was seen in previous studies,^{58-60,67} and is the behaviour that would be predicted by a simple building block approach. The π^* peak associated with the peptide bond is the only major feature that would become more prominent in such a model. As a result of the unambiguous assignment of the feature in the measured spectrum, it is assumed that the calculated value of 287.6 eV is incorrect. This assumption is supported by the relation between electronegativity and the position of the carbonyl π^* peaks; the C16 feature is expected to occur at a higher energy than the similar feature in the C11 spectrum, due to the influence of the electropositive ferrocene moiety on the latter. The DFT calculations place both features at the same energy.

The calculated spectra of the C11 site may or may not agree with the experimental data; its π^* peak is found at 287.6 eV, which corresponds to one of the shoulders seen in Figure 9.2, however there are numerous other features within approximately 0.2 eV of this location. Given that the energy of the C16 feature does not appear to have been calculated correctly, it cannot be determined whether or not it is appropriate to assign the shoulder at 287.6 eV in the measured spectra to the π^* resonance of site C11. Examination of the experimental data shows that there is not a high intensity contribution to the spectra at 287.6 eV, suggesting that the C11 peak may be more appropriately assigned to the 287.8 eV, which has a more significant contribution to the main peak located at 288.0 eV.

A possible explanation for the disparity between the experimental and theoretical data lies in the method that was used to calculate the spectra. As was discussed in Section 5.5, in order to localize the core hole on a particular atom, all other atoms of that

element were replaced by a pseudopotential, essentially treating the nucleus and closely bound electrons as a single point charge. While efforts are made to make the electrons around the pseudopotential resemble the outer-shell electrons of the atom that it is replacing, the match may not be perfect. In the case of carbon atoms, each pseudopotential has four electrons, rather than six, and the nucleus and 1s electrons are replaced by a point charge of $4e^+$, a nucleus of Be. Generally, smaller atoms are less electronegative than larger atoms, and so it is possible that the pseudopotential representation of the carbon atom has a lower electronegativity than the atom itself. If this is the case, then the position of the calculated resonance will be lower than the actual resonance.⁷⁶

As it is not known how the electronegativity of the surrounding environment affects the other features in the spectrum of the same site (or, indeed, if this is truly the source of the disagreement), the term values were determined from the as-calculated spectra. For the purposes of matching the calculated spectrum to the measured spectrum, however, the spectra of sites C11 and C16 were shifted to 287.8 eV and 288.0 eV, respectively.

The calculated C 1s XAS spectra for the benzyl ester sites are shown in Figure 9.10. As in the spectra of the ferrocene C sites, the spectra in Figure 9.10 are dominated by a sharp, low-energy feature around 285.4 eV, corresponding to the benzene π^* resonance. The exception is the spectrum of C22, the site associated with the substituent, which is single-bonded to site C23 and to the benzyl ester oxygen site. Because the environment of site C22 is so different from that of the benzene sites in the ring structure, the details of the transitions in its spectrum are included in a separate section of Table 9.2.

As was seen in the low-energy features of the Cp spectra (Figure 9.8), the position of the sharp resonance varies from site to site; this is attributed to shifts in the core hole energies of the sites, as the variation in the term values associated with the transitions is considerably less than the variation in the peak position (0.58 eV variation in the peak position, 0.19 eV variation in the term value). The peak positions and term

values of the main features in the calculated benzene spectra are summarized in Table 9.2. As was done with the ferrocene sites in Table 9.1, the complete listing of peak positions, etc. is included for the main π^* resonance, while the average values for the other transitions are presented in summary form. The complete, site-specific listing is included in Appendix C.

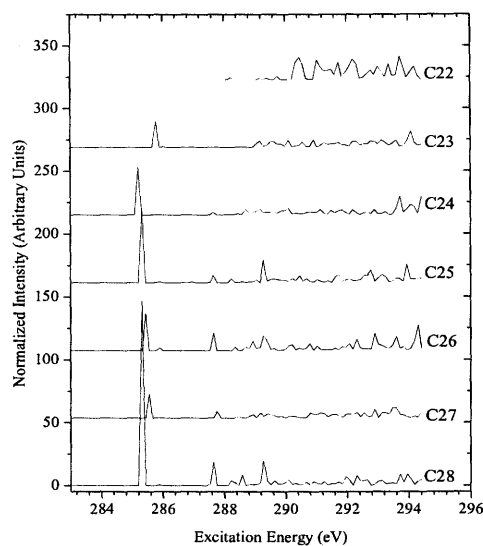


Figure 9.10. C 1s XAS spectra of the benzyl ester sites in Fc-Pro₂-OBz as calculated using StoBe. Vertical offset is added for clarity.

Aside from the π^* resonance, there are three other distinct features in the C 1s XAS spectrum of the benzyl ester. The assignment of the final orbitals involved in these transitions has been the subject of considerable controversy. For the purposes of this study, which is primarily concerned with the characteristics of the ferrocene and peptide portions of the molecules, the final states are assigned according to a recent publication by Püttner *et al.* which makes use of the same DFT program was used in the present work.⁷⁷ The energy levels and spectral features in Püttner's study are in better agreement with the values calculated here than were those presented in the study of benzaldehyde.⁷⁵

Table 9.2: Energy positions and term values for features in C 1s spectra of the benzyl ester sites

Site	Core Level (eV)	Feature (eV)	Term Value (eV)	Assignment
C23	291.32	285.77	4.35	C=C π^*
C24	290.89	285.19	4.50	C=C π^*
C25	291.05	285.31	4.54	C=C π^*
C26	291.11	285.42	4.49	C=C π^*
C27	291.17	285.54	4.43	C=C π^*
C28	291.05	285.31	4.54	C=C π^*
C22	292.82	288.22	3.39	
C22	292.82	289.51	2.11	
C22	292.82	289.74	1.88	
C22	292.82	290.44	1.17	
Site	Core Level ^a	Feature ^a (eV)	Term Value ^a	Assignment ^b
C23-	291.10	287.66	2.24	σ -valence+Rydberg
C23-	291.10	288.32	1.58	σ -valence+Rydberg
C23-	291.10	289.31	0.58	π^* b _{2g} +Rydberg
^a average value for all sites involved in transition ^b assignments based on those given by Püttner <i>et al.</i> ⁷⁷ for benzene				

In addition to the major features discussed above, there is a minor peak at 286.9 eV in the spectrum of site C23, to which the substituent is attached. This feature is also present in the C25 spectrum. The presence of these peaks finally explains the origin of the feature at this energy that was seen in Figure 9.2 and Figure 9.3, falling between the locations of the $3e_{2u}'$ and $3e_{2u}''$ orbitals. Peaks in this energy range have been observed in other substances containing substituted benzene rings, such as the amino acids tyrosine and phenylalanine,⁷⁰ and gaseous phenol⁷⁸. They have been attributed to the main π^* resonance feature of the carbon atom to which the substituent is attached, with the energy shift being the result of a change in the 1s level under the influence of the substituent. The C23 spectrum in Figure 9.10 does indeed show such a shift, the magnitude of which is comparable to that observed in benzaldehyde,⁷⁵ but the 286.9 eV feature is seen *in addition* to the shifted π^* feature, not as a result of it. The term value of the 289.6 eV feature is 3.18 eV, very nearly the same as that of the 288.22 eV peak in the C22 spectrum. The similarity in the two values suggests that the features have an origin in the σ^* -like orbital formed by the single bond between the C22 and C23.

Having examined the spectra of each individual site in the molecule Fc-Pro₂-OBz, it is now beneficial to provide a visual display of the agreement between experiment and theory. Figure 9.11 shows the experimental C1s XAS spectrum of Fc-Pro₂-OBz, with the StoBe DFT calculation below. The individual calculated spectra were broadened in order to improve the visual agreement between the two spectra, and the energy scale of the spectrum was shifted 1.2 eV to lower energies to agree with the calibrated experimental spectrum. The exceptions are the energy scales of sites C11, C16, and C21, which were shifted to correspond to their assumed positions in the measured spectrum: 287.8 eV, 288.0 eV, and 288.2 eV, respectively.

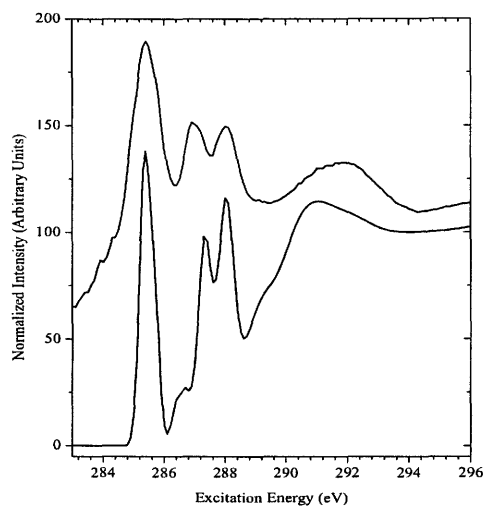


Figure 9.11. Experimental C 1s XAS spectrum of Fc-Pro₂-OBz (top) and DFT simulated spectrum (bottom). Intensity has been normalized at 285.4 eV, and a vertical offset has been added for clarity.

It is evident from Figure 9.11 that the overall absorption spectrum is well represented by the sum of the individual absorption components, once the necessary energy shifts have been applied to the carbonyl spectra. All of the main features in the measured spectrum are present in the calculated spectrum, although the intensity ratios do not completely agree. However, better agreement could be achieved by selectively broadening and weighting the sum of the individual components. As this study is not concerned with absolute determinations of oscillator strengths, this time consuming procedure is not necessary. Also, it has been shown that the intensities of some

features can only be accurately modeled if intermolecular interactions are taken into account,⁴⁰ which is not possible in the current study.

An interesting difference between the spectra is seen in the energy range immediately above the carbonyl π^* resonances (287.5 eV to 288.6 eV). The measured spectrum of Fc-Pro₂-OBz, as well as all other Fc-peptide samples, display an extremely minor shoulder around 288.8 eV, which is not prominently featured in the DFT spectrum. The theoretical spectrum, however, contains a prominent shoulder at 289.0 eV, 0.2 eV higher than the missing feature. This shoulder is due to the contribution of the C11 $3e_{2u}'$ orbital, shifted to a higher energy in this spectrum than in the spectrum used to determine its term value. Although the proline residues also display minor peaks around 288.8 eV (288.9 eV, to be exact), the suppression of the feature in the calculated spectrum, coupled with the emergence of the shoulder feature at an energy consistent with the magnitude of the shift, suggests that the main contribution to the 288.8 eV feature in the measured spectrum is the C11 $3e_{2u}'$ site.

This observation is not only important for matching the calculated and measured spectra, it has ramifications concerning the overall analysis of the electronic structure. If it is true that the DFT calculation correctly predicted the position of this feature, even though the main π^* resonance associated with this site was found at the wrong energy, two of the assumptions made in the analysis to this point are supported. First, because the term value of the C11 feature was calculated using the energy of the feature in the as-calculated spectrum, an error in this energy would change the term value. If, however, the position of this feature was calculated correctly, the term value of 3.41 eV is correct, and the association of the peak with at $3e_{2u}'$ final state is justified. It is important that this association be made, as it is hypothesized that this orbital plays a prominent role in the transfer of charge from the Cp rings to the peptide. If the shifted value is used, the calculated term value is 3.21 eV, which is still very close to the average, although it falls outside of the range of values used to calculate that average.

Second, and less importantly for the purposes of this study, if the energy of the $3e_{2u}'$ feature was calculated correctly, while the main resonance was not, then it would seem that the observed dependence of the position of the π^* feature on the electronegativity of the environment does not directly apply to the unoccupied orbitals of the other features of the site. This conclusion is, of course, dependent on the previous assumption that the errors in calculated π^* positions were due to the difference in electronegativity between the pseudopotentials and the atoms that they were replacing. It must be noted that this latter assumption is by no means confirmed in the present study.

9.2. O 1s XAS Spectra

The oxygen spectra of the Fc-peptide conjugates, involving transitions from the O 1s level to states with 2p contributions, are much less complex than the carbon spectra, due to the difference in the number of non-equivalent sites between the two elements. In fact, in all of the Fc-peptide samples, oxygen is found in only two different nearest-neighbour environments. Each molecule has a single-bonded oxygen site connected to the C-terminus of the final residue in the peptide. This oxygen site will either be in a C-O-C type bonding environment (as in the Fc-Pro_x-OBz series) or a C-O-H environment (for peptides that are protected by an OH group). All other oxygen sites in the molecules are double-bonded to a carbon atom that is in a carboxyl- or amide-like (connected to a nitrogen) environment. Because of these similarities between the oxygen sites of different amino acids, the analysis is rather straightforward. The bulk of the studies that are found in the literature are concerned with near-edge spectroscopies of glycine-based samples, and the results presented here are generally in agreement with those results. The addition of the ferrocene and benzene to the peptide samples does, however, add richness to the spectra.

9.2.1. Experimental O 1s XAS Spectra

The O1s spectra of the Fc-Pro_x-OBz series are shown in Figure 9.12. These spectra were measured at Beamline 6.3.2 at the ALS synchrotron. The minimum value of all spectra has been set equal to zero, and they were then normalized to the intensity of the broad resonance feature located at approximately 539 eV. It must be noted that the spectrum of Fc-Pro₅-OBz was also recorded, but is not shown here. This spectrum is omitted because it is suspected that the sample was contaminated at some point during the process. At all edges, the spectra of Fc-Pro₅-OBz closely resembled that of Fc-Pro₄-OBz. This resemblance was not observed in measurements performed on any edge, at any other time, and so it was decided that the spectra should not be analyzed.

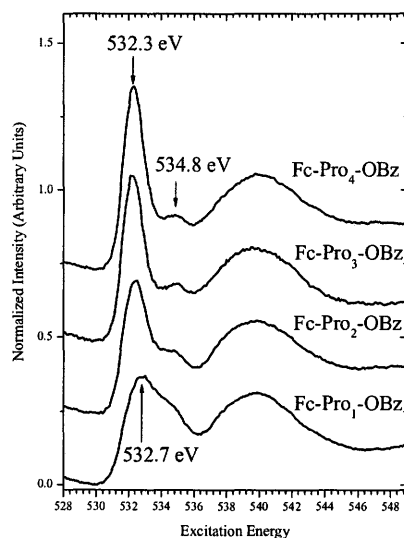


Figure 9.12. Oxygen 1s XAS of the series Fc-Pro_x-OBz ($x=1-4$). The energy values of the most significant transitions are marked.

The O 1s XAS spectra in Figure 9.12 are dominated by the feature centred at 532.3 eV. Based on a building-block approach, it seems apparent that this peak corresponds to transitions into the carbonyl π^* orbitals located at the peptide bonds. The literature has shown that, as in the C 1s XAS, the environment of this group cannot be neglected when the O 1s XAS spectra are being analyzed. Zubavichus *et al.* recently reported a

shift of +0.2 eV in the position of the π^* resonance in the spectrum of triglycine (a three-residue glycine peptide) as compared to the mono- and di-glycine spectra.⁵⁹ This result is similar to those obtained by Gordon and Cooper *et al.* where the shift was observed immediately upon going from the monomer to the dimer, *i.e.* as soon as a peptide bond was formed.^{60,67} These shifts are in keeping with the general behaviour that is expected in carbonyls, as the π^* peak in the O 1s XAS is expected to shift in much the same way as the corresponding C 1s feature. The position of the oxygen peak has been shown to vary by up to 1.6 eV, considerably less than the variation in the carbon peak (3.8 eV).⁷⁶ This difference suggests that the energy of the oxygen 1s orbital is not as strongly affected by the environment as is the carbon 1s orbital.

As Figure 9.12 clearly shows, the main absorption feature in the spectrum of Fc-Pro₁-OBz is centred at a higher energy (532.7 eV) than in the other spectra. This shift would seem to contradict what has been previously reported, except that the C=O groups in the Fc-Pro₁-OBz sample are not found in the same environment as in the monomer, due to the presence of the ferrocene and the benzyl ester. In contrast with the other spectra in Figure 9.12, the main peak in the Fc-Pro₁-OBz spectrum is broad and flat, suggesting that it is composed of the superposition of more than one feature. Because the position of the O 1s π^* peak increases in energy as a function of the electronegativity of the environment of the carbonyl, it is assumed that the resonance associated with the ferrocene carbonyl is found at a lower energy than is the carbonyl at the proline C-terminus.

In the other spectra in Figure 9.12, the 532.3 eV feature that is associated with the peptide bond carbonyls is dominant. It is interesting to observe that this feature appears to correspond in energy to the low-energy portion of the main Fc-Pro₁-OBz resonance peak. This similarity in energy supports the assertion that the dependence of the transition energy on the electronegativity of the surroundings is not as pronounced in the oxygen spectra as in the corresponding carbon spectra. Due to the superposition of the various C=O π^* contributions and the relatively low resolution of the spectra ($\Delta E > 0.2$ eV), it cannot be determined whether or this feature undergoes a small shift in energy analogous to that which is reported in the literature.⁵⁹

The smaller feature at 534.8 eV is not seen in any of the previously reported spectra, and so it can be assumed that it is not associated with the proline residues. The feature that is nearest to it in energy is seen at 535.7 eV in the gas-phase spectra of glycine (536.1 eV in diglycine),^{60,67} and is produced when the oxygen in the carbonyl group is protonated, forming a C-O-H structure.^{60,67,68} A relatively sharp feature is associated with the single-bonded oxygen atom when this occurs.

The protonation of the amide oxygen is linked to the pH-level of the sample, being more likely to occur in acidic solutions. This feature cannot be resolved in the spectra of aqueous glycine, as it is engulfed by the signal from the oxygen sites in the water. However, Messer *et al.* show that the carbonyl π^* resonance develops a shoulder at lower pH values, confirming that the degeneracy of the group is broken by protonation.⁶⁸ It should be noted that the spectrum of Fc-Pro₁-OBz in Figure 9.12 shows an extremely minor feature at approximately 535.7 eV, suggesting the possibility that the ethanol that was used to dissolve the sample had caused protonation of the carbonyl group in the solidified sample. This feature cannot be seen in any of the larger samples, but it is possible that it is simply overwhelmed by the larger features. Kaznacheev *et al.* briefly examined the possibility of protonation in solid samples, concluding that it is a minor effect.⁶³

Given the solid nature of the samples and the presence of the minor feature 535.7 eV in one of the samples, it is unlikely that the feature at 534.8 eV in the O 1s absorption is due to protonation. However, because of the similarities in energy, it is a fair assumption that it is also due to a single-bonded oxygen site, such as the one that is present in the benzyl ester. Additional validation of this assumption is provided by comparison with the measurements by Tanaka *et al.* which show a prominent feature at a comparable energy in the O 1s spectrum of L-aspartyl, an amino acid containing a single-bonded oxygen site.⁶⁶ It will be shown in Section 9.2.2 that the StoBe calculations confirm the assignment of the feature to this resonance.

9.2.2. StoBe O1s XAS spectra

Like the carbon 1s XAS spectra, the O 1s XAS spectra were modeled using StoBe. The spectrum of each of the four sites in the molecule was modeled separately and the broadened results were added together to form a representation of the complete absorption spectrum. The site-specific results support the peak assignments described in the previous section. Figure 9.13 shows the calculated spectra associated with each of the separate oxygen sites. Each spectrum contains valuable information and will be discussed separately.

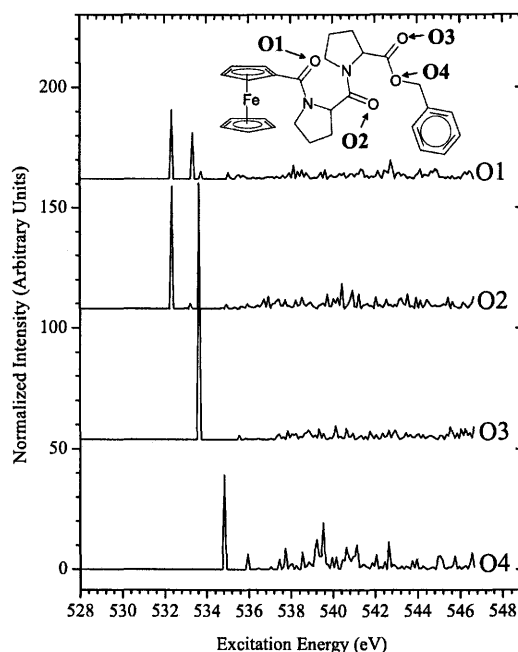


Figure 9.13 The O 1s XAS spectra associated with the four oxygen sites in Fc-Pro2-OBz, as calculated using StoBe. The sites are numbered according to their distance from the ferrocene moiety, as illustrated in the inset. The energy axes of all spectra were shifted by -0.3 eV to better correspond to the experimental data.

The theoretical spectrum of O1 is dominated by the peak at 532.3 eV, with a secondary feature observed at 533.3 eV. The separation between the two features is almost identical to that which was seen in the calculated C 1s XAS spectrum of C11, to which

O1 is attached. The spectrum also exhibits a minor peak around 535.7 eV, suggesting that the ferrocene carbonyl exhibits some single-bonding character, similar to that which would be produced by protonation. The presence of this feature suggests that the small feature seen at this energy in the experimental data is not due to protonation, and so it can be assumed that the pH of the ethanol used to dissolve the samples had, at most, a negligible effect on the spectra.

A low-energy feature also dominates the StoBe spectrum of the O2 site. Like the calculated carbon spectra associated with these two carbonyls, the peaks in the O1 and O2 spectra occur at the same energy. Comparison of the calculated carbon spectra with the experimental results suggested that the calculated peak was found at the wrong energy. Unfortunately, the broadness of the main features in Figure 9.12 makes it impossible to determine whether or not the contributions from the two sites are found at the same energy. Examination of the output files for both spectra suggests that both transitions involve the same final state. Because the energy of the O 1s orbital is not as sensitive to the environment as is the C 1s level, it is conceivable that the main peaks in the O1 and O2 spectra could be found at the same energy. Due to the lack of any evidence to the contrary, this will be assumed to be the case.

The spectrum of the O3 site is also very simple, although the main resonance is shifted to a higher energy, reflecting the difference in the bonding environment of the O3 carbonyl. The main resonance is found at 533.6 eV; a minor shoulder can be seen at this energy in the spectra shown in Figure 9.12. No other notable features are observed in the spectrum.

The spectrum of the benzyl ester oxygen site, O4, confirms the assignment of the 534.8 eV feature in Figure 9.12. The peak seen in the calculated spectrum is found at exactly this energy. The spectrum shows no evidence of any double-bonding character associated with the OBz oxygen.

Separate examination of the spectra calculated for the oxygen sites in Fc-Pro₂-OBz shows that there is excellent agreement between the experimental data and the DFT calculations. With the exception of a small, uniform shift in the energy of all four

sites, the energy scales in the calculated spectra match the calibrated scale in the experiment. In addition, it has been shown that all of the main experimental features are accounted for in the calculation and that their assignment to particular transitions is supported.

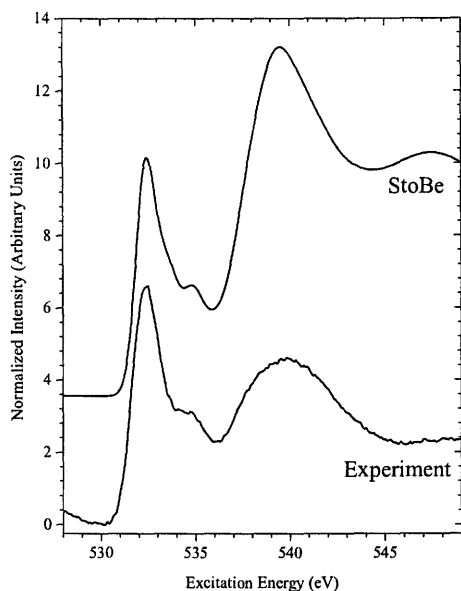


Figure 9.14 Theoretical O 1s XAS spectrum of Fc-Pro₂-OBz produced by weighted sum of StoBe spectra of individual sites, compared with the measured spectrum.

The sum of the StoBe spectra of all four oxygen sites is shown in Figure 9.14. If the spectra were simply added together, the resulting spectrum would drastically overestimate the contribution of the O3 site. This disagreement may be related to the omission of intermolecular effects in the calculations. Nyberg *et al.* used StoBe calculations to show that hydrogen bonding between glycine molecules has a stronger effect on the calculated O 1s XAS spectra than on the C 1s XAS spectra.⁴⁰ The effect of the hydrogen bonding is mostly seen in the calculated intensity of the carbonyl π^* feature. In order to achieve better agreement between the calculated and experimental results, the contribution of this site was arbitrarily scaled by a factor of 0.65; the other sites were not scaled. With the sum performed in this manner, the shape of the main

peak in the measured spectrum is well reproduced. The intensity of the above-threshold region of the spectrum is also overestimated by the calculation.

9.3. N 1s XAS

The transitions that contribute to the N 1s spectra are similar to the C and O spectra, in that they involve final states with 2p-like character. Of all the absorption edges involved in the spectroscopic study of amino acids and peptides, the N 1s edge has caused the most confusion in previously reported studies. Recent publications have shown that the characteristics of the N 1s spectrum of glycine change significantly depending on whether the sample is in solid or gaseous form,^{60,67} adsorbed onto a substrate,^{64,65} or in an aqueous solution, where the shape of the spectrum is also dependent on the pH value.⁶⁸ All of the nitrogen sites in the ferrocene-peptide samples are located at the N-termini of the amino acids, and are involved in three single-bonds each.

9.3.1. Experimental N 1s XAS Spectra

High quality XAS spectra of the Fc-Pro_x-OBz series were obtained at Beamline 6.3.2 and are shown in Figure 9.15. The lowest-energy feature in Figure 9.15 is the peak at 401.7 eV in the Fc-Pro₁-OBz spectrum. Features at approximately this energy have been observed in glycine peptides,^{59,60,67} but are absent in monomer spectra, regardless of the sample environment. The presence of this feature in peptides suggests that the final state of the transition is associated with the peptide bond. The theoretical validation of this peak assignment comes from an interesting property of the peptide bond. Although the N site in the peptide is in a single-bonding environment similar to that of ammonia (NH₃), it develops double-bonding character when the peptide bond is formed, due to the overlap of the carbonyl π^* orbital with one of the N *p*-orbitals.⁵⁸ As a result, the N 1s XAS spectrum has a prominent feature at low energy.

Fc-Pro₁-OBz does not have a peptide bond in the traditional sense, as it contains only one amino acid residue. However, the nearest-neighbour environment of the N-

terminus of the proline is identical to that which is found in a conventional peptide bond. The rest of the molecules in the series have at least one traditional peptide bond, and this difference is reflected in the shift in the main N 1s $\rightarrow\pi^*$ feature from 401.7 eV to 402.2 eV. This energy shift is related to the change in the main carbonyl π^* resonance that is seen in the C 1s XAS spectra of these samples, shown in Figure 9.5. The feature appears broader in the spectra of the larger molecules, which can be attributed to the presence of the 401.7 eV peak as a secondary feature in the main resonance. Because of the dominance of the 402.2 eV feature, however, it cannot be determined if there is any change in the character of this orbital as a function of the growing peptide length.

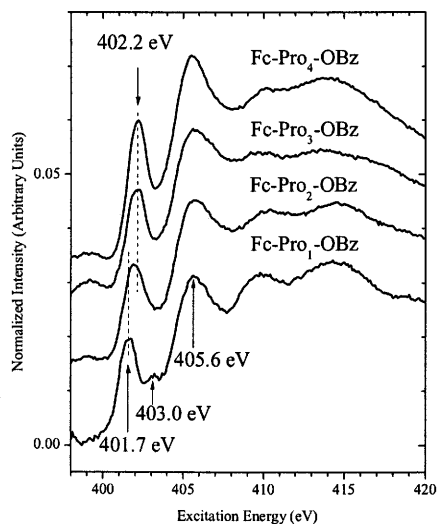


Figure 9.15. Nitrogen 1s XAS of the series Fc-Pro_x-OBz (x= 1-4) measured at Beamline 6.3.2 at the ALS. Spectra have had background subtracted, and a vertical offset has been added for clarity.

In addition to the main π^* resonance feature discussed above, there is a higher-energy feature located at 403.0 eV in the Fc-Pro₁-OBz spectrum. This feature appears to occur at the same location as a minor shoulder that has appeared but not been analyzed in some N 1s XAS spectra of glycine peptides.^{60,67} The other spectra in Figure 9.15 do not exhibit a distinct feature at this energy, although they all have a shoulder at

402.9 eV that may be of similar origin. This latter feature is present in the StoBe calculations, and its origin will be discussed further in the following section.

9.3.2. StoBe N 1s XAS Spectra

The N 1s XAS spectra of Fc-Pro₂-OBz have been simulated using StoBe. As there are only two sites, there is very little ambiguity in the analysis of the relative spectral contributions. The separate contribution of each nitrogen site in Fc-Pro₂-OBz is shown in Figure 9.16. In this case, the energy axes of the calculated spectra did not need to be shifted to correspond to the calibrated experimental data. The spectra are represented in both broadened and unbroadened forms in Figure 9.16, a display technique that was not practical for the calculated spectra corresponding to the other elements in the sample.

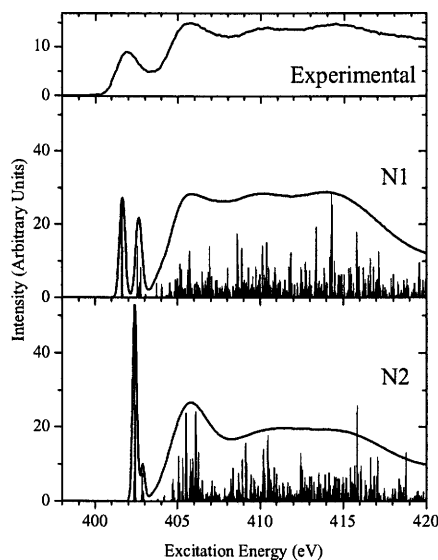


Figure 9.16 The StoBe simulations of the N 1s XAS spectra of both nitrogen sites in Fc-Pro₂-OBz, as well as the spectrum measured at Beamline 6.3.2 of the ALS.

Analysis of Figure 9.16 confirms the assignment of peaks in the measured nitrogen XAS spectra. The site labeled 'N1' is the nitrogen nearest the ferrocene, and its main peak is found at 401.7 eV, the same energy as the lowest-energy features in the

measured spectra. The calculated spectrum of N1 also displays a prominent peak at 402.6 eV, the location of a shoulder that is seen in the measured spectrum of both Fc-Pro₂-OBz and Fc-Pro₃-OBz, although it is more difficult to discern in the latter spectrum. The higher-energy portion of the spectrum consists of a large number of transitions, which is unsurprising given the central location of the nitrogen atoms in the structure. Since they are located along the main backbone of the peptide, the nitrogen atoms would be expected to interact with the majority of the other atoms in the molecule, producing a large number of molecular orbitals. When broadened, the transitions above 404 eV form three wide features, centred at approximately 405.8 eV, 410.0 eV, and 414.3 eV. The locations and appearance of these three features closely resemble the high-energy portion of the measured spectra. The 410.0 eV and 414.3 eV features appear to be located at the same energies as certain broad features in previously published spectra of glycine monomers and peptides, which were attributed to “EXAFS-like oscillations.”⁵⁹ This sort of feature would not be predicted by the StoBe DFT calculations, and therefore if the broad features seen in Figure 9.16 are indeed the aforementioned structures, then it is apparent that the published assignment is incorrect.

The spectrum of the N2 site provides insight into the nature of the peptide bond. It is dominated by a transition at 402.4 eV, which is 0.2 eV higher than the resonance features attributed to the peptide bond in Figure 9.15. Despite this slight disagreement in the energy scales, the calculated spectrum appears to confirm the peak assignment in the measured spectra. The N2 spectrum also has a peak at 402.9 eV, which can be assumed to correspond to the minor shoulders seen at this energy in the spectra shown in Figure 9.15. Its term value (3.32 eV) is very close to that of the $3e_{2u}'$ orbital seen in the C 1s XAS spectra, suggesting that the features in the N 1s spectra may have a similar origin. As in the N1 spectrum, there is a broad peak located around 405.8 eV in the spectrum of the N2 site.

Figure 9.17 shows the sum of the two calculated spectra along with the measured spectrum. Similar to what was done in the analysis of the oxygen calculations (Figure 9.14), the agreement between the spectra was improved by weighting the sum such that

the contribution of the N2 site was decreased by approximately 30%. The agreement between the experimental and calculated spectra would be further improved by shifting the energy axis of the N2 spectrum downward by 0.2 eV.

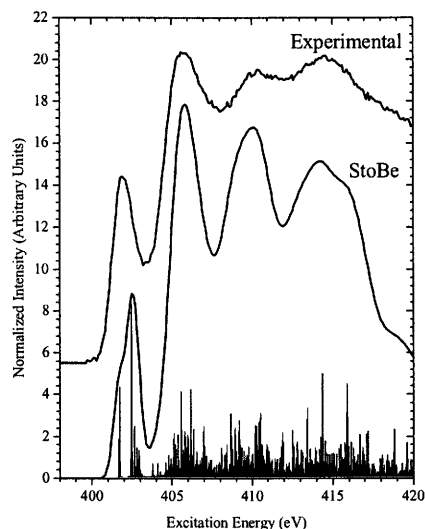


Figure 9.17 Sum of the spectral contributions calculated by StoBe for both nitrogen sites in Fc-Pro₂-OBz (bottom) compared to the measured spectrum (top). The unbrodened contributions are displayed along the bottom of the plot.

9.4. Fe 2p XAS

Previous studies of substituted ferrocenes,^{57,73,79} and disubstituted ferrocenes⁸⁰ have shown that the substituents have little to no effect on the electronic structure of the ferrocene. Dowben *et al.* demonstrated that nature of the substituent will have a small effect on the hybridization of the Fe 3d orbitals with the Cp π^* orbitals as well as the amount of charge that is transferred from the Cp rings to the substituent.⁸⁰ In this study, all of the peptides are linked to the ferrocene via a carbonyl group, and so large changes would not be expected in the electronic structure of the ferrocene. In practice, this turns out to be correct, as the Fe 2p XAS spectra show little variation when the extended structure of the peptide is altered. However, because the ferrocene acts as an electron donor in the electron transfer reactions involving the samples, it is important

to understand the origin of the features in the Fe 2p XAS spectra. The allowable transitions in the Fe spectra involve electrons moving between the 2p core level and higher lying states with either *d*- or *s*-type symmetry.

The spectra of the Fc-Pro_x-OBz series are compared to that of Fc-COOH in Figure 9.18. In general, all spectra have two dominant features, centred near 710 eV and 722 eV, which correspond to the transitions from the 2p_{3/2} and 2p_{1/2} core levels, respectively. The finer features of the spectra will be discussed shortly. The only observable spectral trend is one of increasing noisiness as the size of the peptide increases. This is the expected behaviour, as the concentration of Fe in a given volume of sample decreases drastically as more residues are added to the peptide. As an example, in a molecule of Fc-COOH, iron is one of fourteen non-hydrogen atoms, while in Fc-Pro₄OBz it is one of forty-nine non-hydrogen atoms. This change in concentration leads inevitably to a weaker signal.

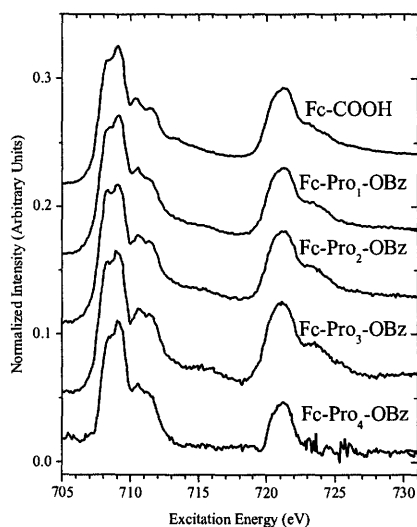


Figure 9.18. The Fe 2p XAS spectra of Fc-COOH and Fc-Pro_x-OBz ($x=1-4$) measured at Beamline 6.3.2 at the ALS. All spectra have had background subtracted and have been offset for clarity.

The DFT calculations of the Fe 2p XAS spectra were not as successful as those performed for other edges. The Fe calculations involved separate calculations for transitions from each of the three 2p orbitals, with only one of the calculations converging. As a result, the assignment of the peaks in the Fe XAS spectra cannot be

completely unambiguous, although convincing arguments will be presented in support of the proposed assignments.

The Fe 2p XAS spectrum of Fc-COOH is presented in Figure 9.19, with the locations of the features of interest marked on the $2p_{3/2}$ absorption feature. The spectra of gaseous ferrocene and substituted ferrocenes^{57,73} differ from those presented here in a number of ways. The gas phase spectra showed a clear separation between the features at 709.1 eV and 711.4 eV, with very little structure present between them. The shoulder on the low-energy side of the main peak also appears to be absent in the literature, although this may be the result of the poorer resolution of the electron energy loss technique.

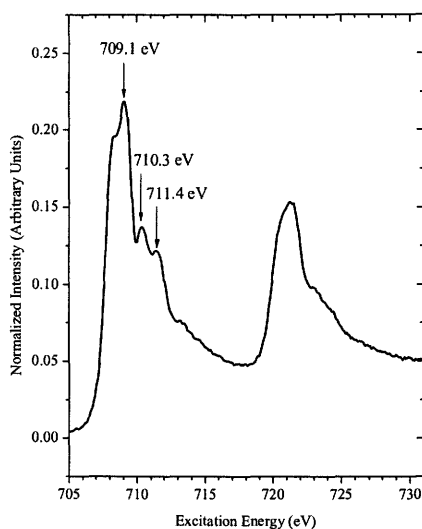


Figure 9.19. The Fe 2p XAS spectrum of Fc-COOH, measured at Beamline 6.3.2. The energies of the notable transitions are marked on the $2p_{3/2}$ absorption feature.

The main feature at 709.1 eV is assigned to transitions into a $4e_{1g}$ -like molecular orbital, similar to the low-energy features seen in the C 1s XAS spectra of these samples (Figure 9.5). Due to the broadness of the feature, it cannot be determined whether or not the peak involves contributions from both the $4e_{1g}''$ and $4e_{1g}'$ orbitals. The assignment of this major feature is quite simple and is not considered a subject of

controversy. The feature at 711.4 eV, however, cannot be so easily explained. Wen *et al.*⁵⁷ assign this peak to transitions from the Fe 2p orbital into a $3e_{2u}$ -like orbital, although there is a significant problem with this assumption.

The difference between the term values of the $4e_{1g}'$ and the $3e_{2u}''$ features in the C 1s XAS spectra is approximately 1.96 eV (0.92 eV between the $4e_{1g}'$ and the $3e_{2u}'$ features), as compared to the 2.6 eV difference seen in the Fe absorption spectra. As there is only one Fe site in the molecules, this disparity cannot be explained by a difference in core levels, suggesting that the assignment of one of the peaks is incorrect.

To resolve this difficulty, the calculated Fe 2p XAS spectra must be examined. The uncalibrated, unweighted spectrum of each of the three Fe 2p orbitals is shown in Figure 9.20. The actual physical nature of the three 2p orbitals is difficult to determine; in practice only the origin of the Fe_1 spectrum can be unambiguously determined. A preliminary DFT calculation was performed to determine the orbital characteristics of the unexcited system, and this calculation did not suffer from the convergence difficulties associated with XAS calculations. The initial calculation shows that the Fe_1 orbital has a strong $2p_z$ character, while the other two are a mixture of $2p_x$ and $2p_y$ states. Whether this mixing is an anomaly of the calculation or has real physical significance is unknown. However, the Fe_2 and Fe_3 orbitals were shown to be nearly degenerate, with only a difference of 0.2 eV in their ground-state binding energies. This similarity is consistent with what is expected for the $2p_x$ and $2p_y$ orbitals, given that both lie parallel to the planes of the Cp rings.

The transition energies and term values of some features in the calculated Fe XAS spectra are shown in Table 9.3. The transitions that will be discussed are most visible in the spectrum of Fe_3 , where they contribute to the four lowest-energy features in the spectrum. The analogous peaks in the other two spectra in Figure 9.20 are more difficult to discern.

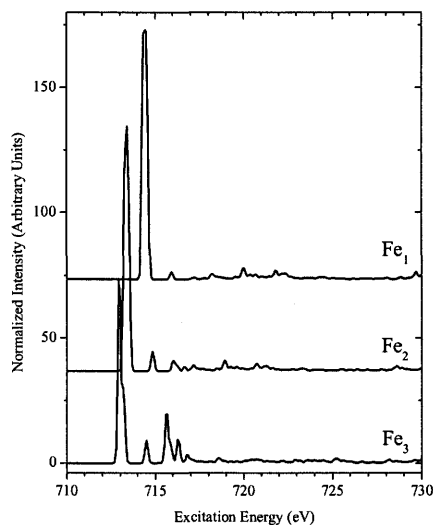


Figure 9.20. The uncalibrated Fe 2p XAS spectra of Fc-Pro₂-OBz, as calculated by StoBe. The spectrum associated with each 2p orbital is numbered with a subscript to avoid confusion with the numbering scheme used for nonequivalent sites in previous figures.

Close inspection of the main peaks in all of the spectra shown in Figure 9.20 reveals that they are produced by significant contributions from two different transitions. The term values of the two peaks are similar to those shown in Table 9.1 for transitions from the C 1s orbitals of the Cp rings into the two $4e_{1g}$ -like orbitals. The difference between those values and the ones that are shown in Table 9.3 may be attributable to differences in the effect of the core hole in the different elements. Given the similarity in the values, however, it is reasonable to assume that the assignment of the peak to transitions into the $4e_{1g}'$ and $4e_{1g}''$ orbitals is justified.

The next highest feature has an average term value of 3.20 eV, which is very similar to that of the $3e_{2u}'$ transition observed in the C 1s XAS spectra (Table 9.1). In addition, the transition in the Fe spectra is the third-lowest-energy transition that is listed in the output file, as is the $3e_{2u}'$ transition in the C 1s spectra. Given the similarities between the C and Fe transitions, it appears that the transition seen in the Fe spectra can be confidently assigned to transitions into the $3e_{2u}'$ orbital. This assignment is further supported by the relative intensities of the peaks, as it has been established that the $3e_{2u}$ -like orbital has more Cp π^* character than Fe 3d character, while the opposite is

true for the $4e_{1g}$ -like orbitals. The intensity of the transition from the Fe 2p levels into the latter orbital is expected to be much larger than into the former, consistent with the spectra that are shown in Figure 9.20.

Table 9.3: Transitions in the calculated Fe 2p XAS spectra of Fc-Pro₂-OBz

Site	Core Level (eV)	Feature (eV)	Term Value (eV)	Assignment
Fe ₁ (2p _z)	719.09	714.43	4.76	$4e_{1g}'$
		714.52	4.58	$4e_{1g}''$
		715.90	3.19	$3e_{2u}^a$
		717.24	1.85	Cp' C-H σ^*
		717.76	1.33	Cp C-H σ^*
Fe ₂	718.04	713.27	4.76	$4e_{1g}'$
		713.45	4.59	$4e_{1g}''$
		714.84	3.20	$3e_{2u}^a$
		716.01	2.02	Cp' C-H σ^*
		716.68	1.36	Cp C-H σ^*
Fe ₃	717.69	712.95	4.74	$4e_{1g}'$
		713.20	4.49	$4e_{1g}''$
		714.49	3.20	$3e_{2u}^a$
		715.60	2.10	Cp' C-H σ^*
		716.26	1.43	Cp C-H σ^*
				^a Tentative assignment

Although the above analysis strongly suggests that the transition in question involves the $3e_{2u}'$ final state, the analysis is not complete. It has not yet been explained why there is no observable transition with a term value around 2.30 eV, corresponding to the $3e_{2u}''$ orbital of the unsubstituted Cp ring. Closer examination of the StoBe output file shows that in each spectrum there is a transition with a term value of 2.30 eV; it does not appear in any of the plots in Figure 9.20 because of its extremely low oscillator strength (average value 0.000007 vs. 0.001439 for the $3e_{2u}'$ transition). This difference in oscillator strengths suggests that there is only a very small contribution of the Fe 3d orbitals to the $3e_{2u}''$ orbital, further supporting the conclusion, drawn from the analysis of the C 1s XAS spectra, that this orbital has the characteristics of the $3e_{2u}$ orbital of unsubstituted ferrocene. In pure ferrocene, the orbital has no contribution from the Fe; a pictorial representation of this orbital is included in Appendix E.

Having explained the absence of the Fe $2p \rightarrow 3e_{2u}''$ transition, the difficulty now lies in explaining the *presence*, however slight, of the Fe $2p \rightarrow 3e_{2u}'$ transition. Recalling that the final orbital is associated with the substituted Cp ring, and that, furthermore, the substituent C11 site contains an orbital with a term value equal to that of the $3e_{2u}'$ orbital, it seems likely that the presence of the Fe $2p \rightarrow 3e_{2u}'$ transition is due to the influence of the substituent. It is now apparent that the change in the electronic structure of the ferrocene is not restricted to the Cp rings; it also extends to the Fe atom. It is also apparent that the previous studies of the Fe 2p absorption spectra⁵⁷ misassigned the feature found at 711.4 eV to transitions into a $3e_{2u}$ -like final state; the location of the peak in this study lies too close to the main resonance feature to support this finding. In order to explain the true origin of this prominent feature, higher-energy transitions must be considered.

The other two spectral features included in Table 9.3 have average term values of 1.98 eV and 1.37 eV. These values are very similar to those shown in Table 9.1 for transitions into the C-H σ^* orbitals of the substituted and unsubstituted Cp rings, respectively. Given that the Fe in ferrocene is in a doubly ionized state with at least one unoccupied 4s orbital, it is possible that these orbitals are hybridized with the C-H σ^* orbitals. The energies of these transitions relative to the main $4e_{1g}$ -like resonance feature suggests that they are the source of the prominent 711.4 eV resonance feature seen in the experimental Fe 2p XAS spectra. The combination of the energy scale agreement along with the observed splitting of the feature suggests that the assignment of this transition to a σ^* orbital is justified, in contradiction of the previously published work.

The calculated Fe 2p XAS spectra can now be used to interpret the measured spectra. Figure 9.21 shows the summation of the three Fe 2p XAS spectra from Figure 9.20, shifted so that the lowest-energy transitions align with the main peak of the measured spectrum. To improve the visual agreement between the spectra, the contribution of the Fe_1 component has been given a relative weight of 0.66, and the $2p_{1/2}$ XAS feature has been reproduced by shifting the $2p_{3/2}$ component upward by 12.1 eV and scaling its

intensity to agree with the measured spectrum. The shifted and scaled feature is then added to the spectrum representing the $2p_{3/2}$ component.

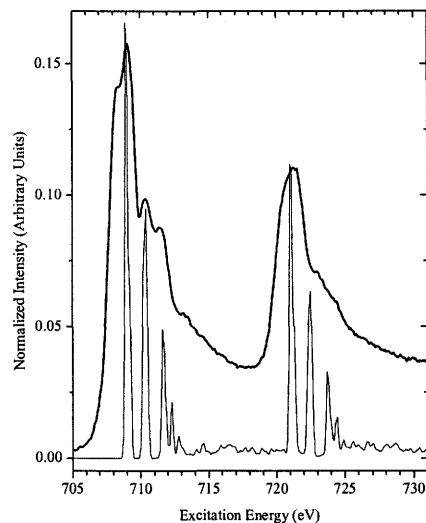


Figure 9.21. Fe 2p XAS spectrum of Fc-COOH compared to spectrum predicted by DFT.

Comparing the spectra, it appears that the prominent feature at 710.3 eV is due to the $2p_{3/2} \rightarrow 4e_{1g}$ transitions of the Fe_1 site, which unfortunately overwhelms any possible contribution from $2p_{3/2} \rightarrow 3e_{2u}$ transitions. It must be noted, however, that this analysis of the experimental peak assumes that the energy scales of the three calculated components are correct with respect to one another. If this is not the case, and all three of the $2p_{3/2} \rightarrow 4e_{1g}$ transitions contribute to the main peak at 709.1 eV, then the 710.3 eV feature must be assigned to a $3e_{2u}$ -like final state. However, given the previous discussion of this feature, it seems unlikely that a peak associated with this final state would have such a large intensity, especially considering that the comparable transitions in the C 1s XAS spectra are relatively minor features.

The 711.4 eV feature is also well represented by the calculation. The larger peak, which was associated with the C-H final state of the substituted Cp ring, is found at 711.6 eV. There is also a faint shoulder on the high-energy side of the feature in the measured spectrum, suggesting that it may be the result of two non-degenerate

transitions. The shelf-like feature around 713 eV is associated with the $2p_{3/2}$ ionization threshold.⁵⁷

The calculated spectra, as presented, do not provide an explanation for the prominent shoulder on the low-energy side of the main resonance. There are numerous possible explanations for this feature, located at 708.5 eV. It is possible that the relative energy scales of the calculated spectra are not, as is assumed, correct in their relation to each other. If this is the case, then the feature may simply be the result of transitions from separate, non-degenerate $2p_{3/2}$ orbitals into common $4e_{1g}'$ and $4e_{1g}''$ orbitals. It is also possible that the splitting is due to an intermolecular field effect. Previous models of solid-state Fe 2p XAS spectra using atomic multiplet methods have shown significant alteration in the spectral features in this energy range as the crystal field parameter is varied.^{81,82} It is unknown, however, how this effect would translate to molecular solids.

9.5. Radiation Damage

Recent studies have shown that amino acid complexes can be damaged by irradiation with soft X-rays.^{69,70} In this experiment, steps have been taken to minimize any possible effects of radiation damage, including limiting the time in which the samples are exposed to radiation and limiting the intensity of the radiation. To show that such steps are justified, the effect of high-intensity X-rays was examined by first measuring a C 1s XAS spectrum of Fc-Pro₁-OBz, then increasing the intensity of the incident radiation by opening the monochromator entrance and exit slits. After five minutes of irradiation, the slits were restored to their previous sizes, and the spectrum was remeasured. Both XAS spectra are shown in Figure 9.22, and the effect of the radiation is clear.

Generally, the main spectral features have become broader upon irradiation, with the 285.5 eV feature displaying a significant increase in intensity on the low-energy side. This observation is consistent with the observations of Zubavichus *et al.*, who attributed this effect to deprotonization of the carbon sites in the amino acids, causing an increase in the number of C=C and C=N double bonds.^{69,70} The higher-energy

features also become less prominent under irradiation, suggesting that the bonds with which they are associated, primarily the C=O bonds and ferrocene-related structures, are decreasing in concentration.

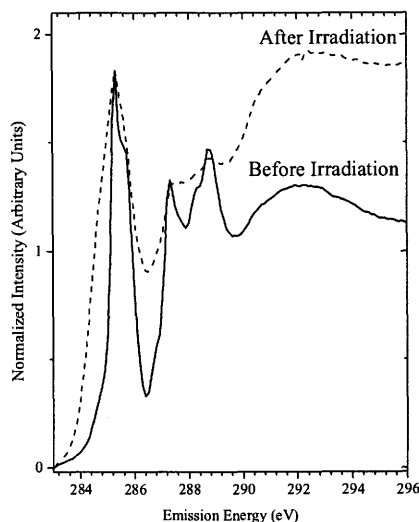


Figure 9.22. The C 1s XAS spectra of Fc-Pro₁-OBz before (solid line) and after (dashed line) exposure to high-intensity soft X-rays, showing the effects of radiation damage. Both spectra were measured at Beamline 8.0.1 at the ALS.

The studies of radiation damage in amino acids have been concerned only with the monomers; there have been no formal studies of the effect of soft X-rays on peptidic materials. Our data suggest that radiation damage may have caused a change in the structures of the samples measured at Beamline 8.0.1. Evidence for this effect is seen in the character of the 285.5 eV feature, which has two distinct peaks associated with benzene and ferrocene. These peaks are seen with exceptional clarity, which unfortunately suggests that they are the result of free ferrocene and benzene molecules, rather than those same molecules as part of a larger structure.

In an attempt to minimize the effects of radiation damage on the samples, absorption measurements were performed at Beamline 6.3.2. As it is a bending magnet, rather than an undulator, that produces the synchrotron radiation at Beamline 6.3.2, it was expected that the effects of irradiation would be minimized when measurements were performed there, due to the lower flux (see Sections 2.1 and 2.2). The quality of the data obtained and the agreement with the theoretical spectra suggest that this was the

case. In addition, many XAS spectra were measured over the same energy range twice in rapid succession, once with increasing excitation energy and once with decreasing excitation energy. This process was performed both to check for any potential effects of radiation damage and also to identify and correct for charging effects.

As is shown in Figure 9.23, the direction of the scan did not have any noticeable effect on the measured spectrum. The relative intensities are virtually identical in all cases, and most importantly, the shape of the main resonance at 285.5 eV is unaffected. If radiation damage were indeed having a significant effect on the XAS spectra, this feature would be expected to be broader in the bottom spectrum, the measurement performed with decreasing excitation energy, than in the initial spectrum. This is clearly not the case, as there is no noticeable difference in the shape of the two features, even when one is plotted directly atop the other. In Figure 9.23 a small vertical offset was added to allow the spectra to be compared. The elapsed time between the two measurements of the 285.5 eV resonance (~ 7 minutes) is well within the time frame in which Zubavichus *et al.* observed noticeable radiation damage.^{69,70} The spectra of other materials were also studied in this way, with the same results as were seen in the Fc-Pro₁-OBz spectra.

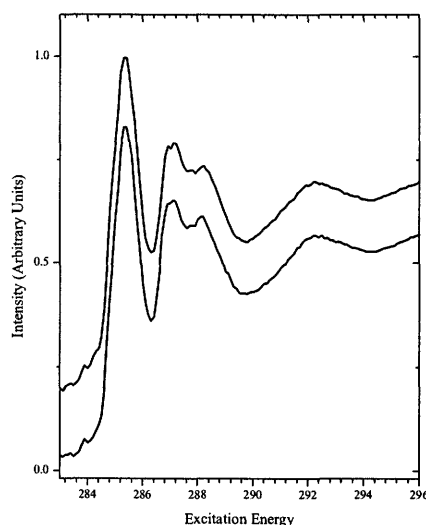


Figure 9.23. The C 1s XAS spectrum of Fc-Pro₁-OBz measured with increasing (top) and decreasing (bottom) excitation energy at Beamline 6.3.2. A small vertical offset is added to differentiate the spectra.

10. XES AND RIXS SPECTRA

Soft X-ray emission spectra must necessarily be measured using high-intensity radiation, in this case the undulator radiation at Beamline 8.0.1 at the ALS. Unfortunately, exposing organic materials such as amino acids to this sort of radiation causes damage to the sample, and therefore the measured spectra may not provide a true indication of the occupied density of states of the material. In addition, emission measurements cannot be performed at Beamline 6.3.2, and so a true, complimentary set of XAS and XES measurements could not be obtained. As a result of these difficulties, the spectra in this section will be analyzed as if they were produced by emission from the separate components of the Fc-peptide complexes, rather than the complex as a whole. Despite this qualification, it will be shown that the emission data are in agreement with the conclusions drawn from the XAS spectra regarding the assignment of various features.

Previously published experiments have studied the soft X-ray emission of glycine monolayers^{40,64,65,83-85} and benzene,^{36,84,86-92} allowing comparisons to be made with the data collected in this experiment. Due to the previously mentioned concerns about the sample integrity, along with the broadness of the emission features and the large number of overlapping contributions, the analysis of the XES data cannot, in this case, lead to any strong conclusions.

10.1. C K_{α} Emission

The carbon K_{α} resonant inelastic X-ray scattering (RIXS) spectra of Fc-Pro₁-OBz are shown in Figure 10.1. All spectra were measured with large entrance and exit slits (100 μ m and 150 μ m respectively) and an acquisition time of 300 seconds. The spectra are dominated by the large, broad fluorescence features centred near 278 eV, and also

exhibit a sharp feature at higher energy. This feature, referred to as the elastic peak, tracks the change in the excitation energy and is due to a combination of simple reflection of the incoming radiation and the decay of the excited electron back into its original core hole.

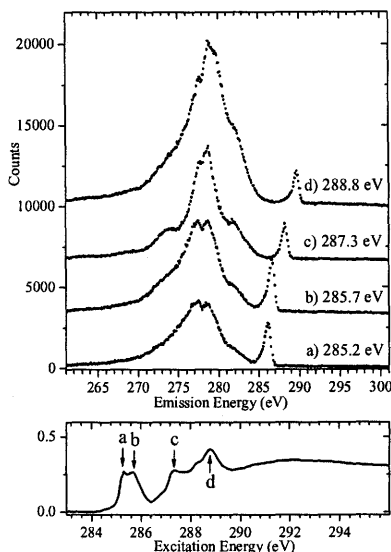


Figure 10.1. The C K α RIXS spectra of Fc-Pro₁-OBz (upper panel). The excitation energy for each spectrum is shown to the right of the main resonance, and the location of each excitation energy is indicated by an arrow on the XAS spectrum (lower panel).

Inspection of the RIXS spectra shows that there is no discernible difference between spectra *a* and *b*, which were intended to correspond to the resonant excitations into the benzene π^* and ferrocene $4e_{1g}$ orbitals, respectively. This lack of differentiation does not suggest that the valence densities of states of the two components are the same; rather it is a result of insufficient resolving power and the overlap of the features in the XAS spectra. There are also questions about spectrum *d*, prompted by the confusion regarding the origin of the 288.8 eV feature in the XAS spectra. It is likely due to transitions into a carbonyl π^* orbital, but the origin of this orbital is unknown.

To verify the above assumption, the spectrum of Fc-COOH was subtracted from spectrum *c*, with the expected result that the remaining intensity would correspond to

the benzene emission. The intensities of the two spectra were normalized to a common value at 282.0 eV. While normalizing the spectra in this way does introduce some uncertainty into the analysis, examination of previously published spectra suggests that it will not introduce a significant bias into the analysis. The location of the intensity normalization was chosen because it is well above the energy of the benzene emission that has been previously reported, by Skytt *et al.*⁹⁰ for example, and so it was assumed that the intensity contributions in this region could be attributed to other sites. The two spectra involved in the manipulation, as well as the spectrum showing the difference between them, are shown in Figure 10.2. The last spectrum clearly exhibits a two peak structure, similar to the benzene spectrum measured by Skytt *et al.*⁹⁰ In agreement with these previously published spectra; the separation between the two features is approximately 3 eV.

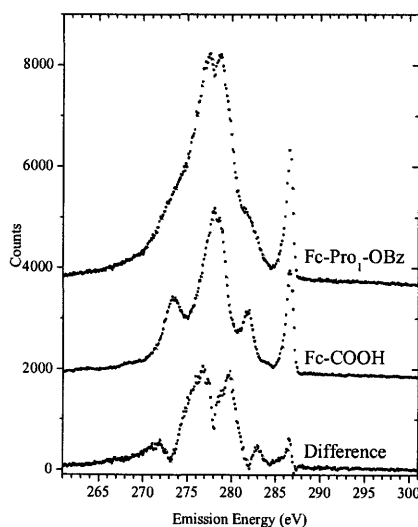


Figure 10.2. C K α RIXS spectra of Fc-Pro₁-OBz and Fc-COOH. The bottom spectrum is the difference between the two normalized spectra.

Despite the above difficulties, comparison of spectrum *c*, corresponding to excitations into a $3e_{2u}$ -like orbital of the ferrocene, with spectrum *b* allows a degree of site-

selectivity to be introduced into the analysis. Spectrum *c* bears a strong resemblance to the spectrum of Fc-COOH[†], supporting the assumption that the majority of the emission originates from the ferrocene in this case. The spectral contributions of the ferrocene also appear in spectrum *b*, although they are significantly broader and less distinct compared to spectrum *c*. There is also a much larger contribution of the feature around 277.6 eV in the former spectrum. Since it appears that spectrum *c* is produced by the superposition of benzene and ferrocene emission features, these spectral differences are likely the result of the benzene contribution.

To verify the above assumption, the spectrum of Fc-COOH was subtracted from spectrum *c*, with the expected result that the remaining intensity would correspond to the benzene emission. The intensities of the two spectra were normalized to a common value at 282.0 eV. While normalizing the spectra in this way does introduce some uncertainty into the analysis, examination of previously published spectra suggests that it will not introduce a significant bias into the analysis. The location of the intensity normalization was chosen because it is well above the energy of the benzene emission that has been previously reported, by Skytt *et al.*⁹⁰ for example, and so it was assumed that the intensity contributions in this region could be attributed to other sites. The two spectra involved in the manipulation, as well as the spectrum showing the difference between them, are shown in Figure 10.2. The last spectrum clearly exhibits a two peak structure, similar to the benzene spectrum measured by Skytt *et al.*⁹⁰ In agreement with these previously published spectra, the separation between the two features is approximately 3 eV.

[†] The comparison of the C K_α RIXS spectra of Fc-Pro₁-OBz and Fc-COOH is contained in Appendix D.

11. DENSITY OF STATES CALCULATIONS

In addition to the simulation of XAS spectra, StoBe has been used to calculate the occupied and unoccupied densities of electronic states. Because they do not involve a core hole and do not involve the calculation of oscillator strengths, these calculations are much easier to perform than the XAS calculations included in the previous sections. As a result the density of states of Fc-Pro₃-OBz could be calculated and compared to that of Fc-Pro₂-OBz, where this is not possible with the XAS calculations. This is an extremely important advancement, because the addition of the third proline residue coincided with the abrupt change in redox potential that was observed in cyclic voltammetry studies.⁴ The DOS calculations are extremely valuable to the analysis of the electronic behaviour of these materials.

Like the XAS calculations, the density of states for each site in the molecule can be computed separately. These calculations give a direct representation of the relative energy positions of the orbitals, without the influence of the core hole or the need to interpret the features as term values. The unperturbed density of unoccupied states cannot be directly measured, and so the XAS analysis is a vital complement to these calculations as it provides verification of the accuracy of the DOS calculations. Because the XAS calculations are based on perturbed DOS results, the close agreement that was found between the experimental and theoretical spectra suggests that the unperturbed DOS calculations provide an accurate portrayal of the ground-state electronic structure of the molecule.

The StoBe DOS output can be displayed in graphical form, similar to the XAS spectra, but on the binding energy scale. To provide a more visual representation of the orbitals, complementary calculations have been performed using Spartan,⁹³ which is also a DFT program, although the calculations are much less rigorous. It is nevertheless a useful tool, as it allows 3-dimensional models of the molecule to be

drawn with the orbital plots overlaid. The results of the two programs generally are in agreement in terms of the locations of the orbitals, although the energy scales do not match. As the calculations performed by StoBe are much more rigorous, they will be assumed to be the more accurate model; the results of the Spartan calculations will be used only to provide visual aides.

11.1. Fc-Pro₂-OBz Density of States

Figure 11.1 shows the unoccupied carbon DOS of Fc-Pro₂-OBz as calculated using StoBe. The density is presented as a series of site-resolved contributions in order to show the spatial extent of some of the orbitals. The individual contributions are displayed in the order described by Figure 9.7.

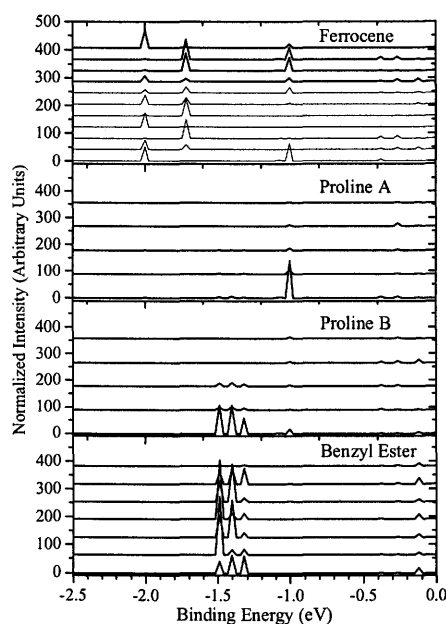


Figure 11.1. The site-resolved carbon density of unoccupied states of Fc-Pro₂-OBz, calculated using StoBe. Each plot represents the contribution of an individual atom to the overall DOS, and the sites are arranged according to their position in the molecule.

The orbital located at -1.998 eV is the lowest unoccupied molecular orbital (LUMO) of the system; in this case it is the lower-energy of the two $4e_{1g}$ -like orbitals of the ferrocene. Figure 11.1 shows that the LUMO does not have any contributions from

carbon atoms beyond C11, the site that is associated with the substituent carbon. Note that the vertical scales are set such that the DOS of Proline A and Proline B are magnified 2.5 times with respect to the other two panels.

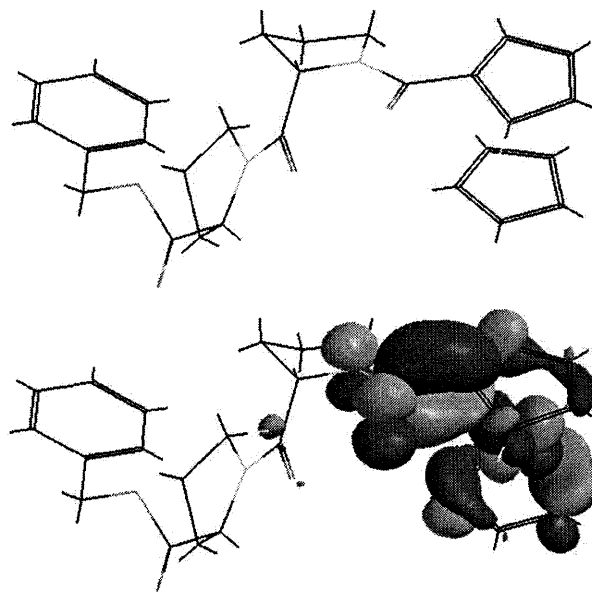


Figure 11.2. The LUMO of Fc-Pro₂-OBz as calculated by Spartan (bottom). The wireframe structure of the molecule is shown above as a reference.

The splitting of the $4e_{1g}$ orbital is clearly apparent in Figure 11.1. The $4e_{1g}'$ orbital, which contains a contribution from the substituent site C11, is the LUMO, while the $4e_{1g}''$ orbital that has the character of the unsubstituted ferrocene has a slightly higher energy, at -1.720 eV. The physical shape of the LUMO that was calculated using Spartan is shown in Figure 11.2. The two different shades used to draw the orbital represent the positive and negative portions of the wave function, and the boundary of the orbital is located at the default probability amplitude of 0.032. There is a slight disagreement between the Spartan and StoBe calculations; the former suggests that there is a contribution to the orbital from the carbonyl located at the peptide bond, while StoBe does not show this. Despite this small disagreement, however, the Spartan picture provides a valuable visual interpretation of the LUMO. It will shortly

be shown that Figure 11.2 accurately represents the contributions from the other elements, namely the O1 and N1 sites.

The orbital that is found at -1.0 eV in Figure 11.1 is also of interest. This feature is actually due to two closely spaced orbitals (-1.074 eV and -0.9998 eV), representing the $3e_{2u}$ -like orbitals seen in the XAS spectra. The change in the spacing between the orbitals seen in the XAS spectra can be attributed to the presence of the core hole, which has been shown to produce this type of behaviour in aromatic ring structures.^{77,90} Figure 11.1 clearly shows that these orbitals have contributions not just from the ferrocene and its immediate attachment (C11), but also throughout the peptide and into the benzyl ester. The density of states calculations confirm what was inferred from the term values of the XAS data, and suggests that this orbital may be extremely important in the transfer of electrons from donor to acceptor. It should also be noted that the order of the $3e_{2u}$ -like orbitals appears to change under the influence of the core hole. The higher-energy feature in Figure 11.1 appears to correspond to the $3e_{2u}'$ feature, as it has a significant contribution from the C11 site. Although reordering of orbitals is not expected to occur in the presence of a core hole,³⁹ the separation of the Cp rings may allow this to occur.

Having discussed the pertinent details of the site-resolved unoccupied carbon DOS, the carbon sites can now be combined according to their location for ease of display. The plots labeled 'Ferrocene,' 'Proline A,' etc. in Figure 11.3 are composed of the sums of the individual carbon contributions, divided by the number of carbon atoms involved. The oxygen sites are numbered as shown in the inset in Figure 9.13, and the nitrogen sites follow the numbering scheme described in Section 9.3.2, with the index increasing with the distance of the site from the ferrocene. Figure 11.3 is arranged such that it provides a spatially-resolved representation of the total DOS of Fc-Pro₂-OBz. If read from top to bottom, the figure maps the changes in the DOS upon going from the electron-donating Fe atom toward the electron-accepting benzyl ester.

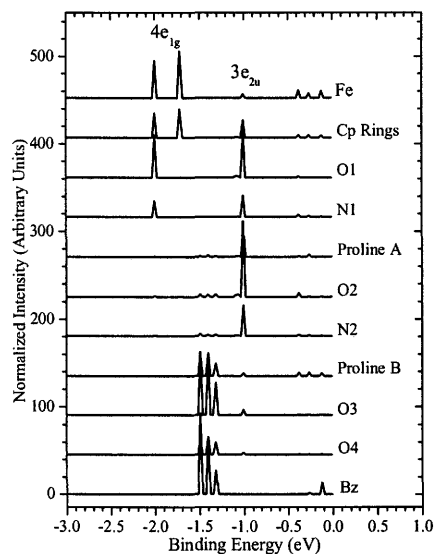


Figure 11.3. The unoccupied DOS of Fc-Pro₂-OBz, calculated using StoBe. All components are displayed separately, and the plots are arranged according to their corresponding position on the molecule. A vertical offset is added for clarity.

An important conclusion that can be drawn from Figure 11.3 is that the $3e_{2u}'$ orbital has contributions from the oxygen and nitrogen sites as well as from the carbon sites. The significance of this observation is that the $3e_{2u}$ orbital is shown to provide an uninterrupted pathway for electron transfer along the peptide, removing the need for electrons to hop from one site to another or to tunnel through a potential barrier.

While it is true that the benzyl ester sites do not contribute to the $3e_{2u}'$ orbital, this does not necessarily mean that the electron cannot come to rest on it. The orbital is being proposed as a pathway for the electron transfer, not as a final location for the transferred electron. The orbital extends all the way to the O4 site, more than far enough to overlap with the locations of the unoccupied benzene orbitals. Therefore it is easy to envision an electron in the higher-energy $3e_{2u}'$ orbital decaying into a lower-lying orbital, such as the three that are located at -1.49 eV, -1.40 eV, and -1.31 eV in the lower spectra in Figure 11.3.

The highest-energy orbitals shown in Figure 11.3 are located between -0.5 eV and 0 eV. These orbitals correspond to the features around 711.4 eV in the Fe XAS spectra

seen in Figure 9.21. In Section 9.4, the features in this region were attributed to transitions into final states associated with the C-H σ^* orbitals of the Cp rings. The DOS calculations provide corroboration of this theory, as the orbitals in question are mainly located on the Fe and Cp sites. In order to better understand the Fe contributions to these orbitals, the symmetry-resolved DOS is shown in Figure 11.4. The p -type symmetry contribution is excluded from the graph, as there is no such contribution in this region.

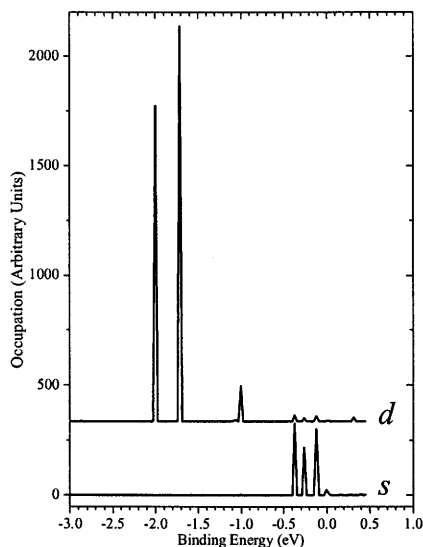


Figure 11.4. The s and d contributions to the Fe density of states of Fc-Pro₂-OBz, calculated using StoBe.

As expected, the major contribution at the energies associated with the $4e_{1g}$ - and $3e_{2u}$ -like orbitals is from the d -type orbitals. The higher-energy region, however, is dominantly s -type, confirming the deduction made in Section 9.4 that these orbitals are derived from the unoccupied Fe 4s orbitals. In order to further probe the d contribution in this region, the DOS can be further resolved into x^2 , xy , xz , y^2 , yz , and z^2 contributions. The latter five plots are shown in Figure 11.5; there was found to be no x^2 contribution. The region involved with the C-H σ^* orbitals is magnified by a factor of one hundred in order to ease the analysis. It is obvious from Figure 11.5 that all of

the unoccupied 3d orbitals in some way contribute to the DOS of each molecular orbital in the ferrocene; the only exception involves the absence of an xy contribution to the $4e_{1g}'$ LUMO. Under magnification, it is seen that there are four molecular orbitals in the C-H σ^* region, all of which have contributions from the 3d and 4s orbitals. The major contributions to all four come from the off-axis orbitals, which given the geometry of the system are more likely to interact with the Cp rings.

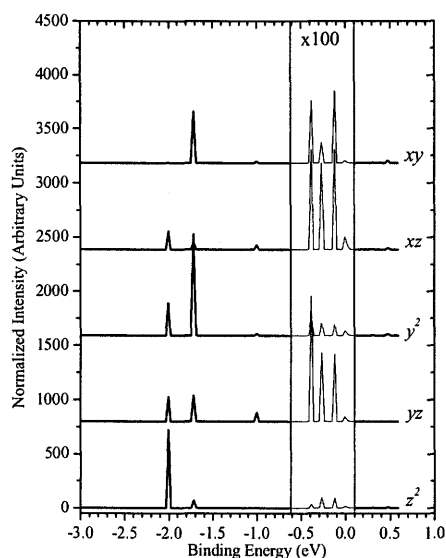


Figure 11.5. The contributions of the individual 3d orbitals to the unoccupied Fc-Pro₂-OBz DOS, as calculated using StoBe. The region from -0.6 eV to 0.1 eV is magnified 100 times, and a vertical offset is added for clarity.

All four of the orbitals in the -0.5 to 0 eV region were modeled using Spartan and are shown in Figure 11.6. Visually, the orbitals seem to have little in common, but close examination reveals that they are all associated with the C-H bonds.

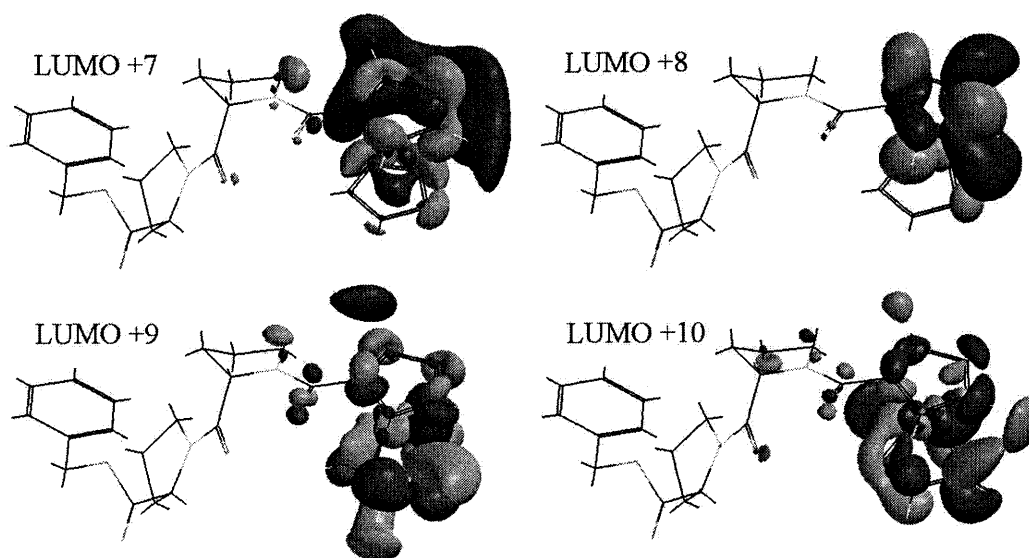


Figure 11.6. The C-H σ^* orbitals of Fc-Pro₂-OBz as calculated using Spartan. The numbering system is a reference to the number of orbitals between the one in question and the LUMO (i.e. LUMO +7 is the eighth unoccupied orbital).

11.2. Fc-Pro₃-OBz Density of States

The Fc-Pro₂-OBz density of states calculations have clarified and confirmed much of the information that was gleaned from the XAS and XES spectra. To this point, however, none of the information that has been discovered is able to explain the unusual electronic behaviour of the Fc-Pro_x-OBz samples. The addition of the third proline residue to the peptide chain does not have any unexpected effects on the experimental XAS spectra. Fortunately, the DOS calculations provide a representation of the unperturbed electronic structure, and these calculations may provide the information that is needed to understand this unique electronic behaviour.

The unoccupied DOS of Fc-Pro₃-OBz is shown in Figure 11.7 in much the same format as the Fc-Pro₂-OBz DOS was presented in Figure 11.3. Rather than performing a complete analysis of the Fc-Pro₃-OBz calculations, it is more informative to focus on the areas in which these calculations differ from the Fc-Pro₂-OBz DOS. For example, the DOS associated with the ferrocene and the two adjacent proline residues closely

resemble those of the Fc-Pro₂-OBz ferrocene and the proline that is adjacent to it. The only significant difference is a uniform shift of approximately 0.4 eV toward higher energy, with the peak assignments remaining unchanged.

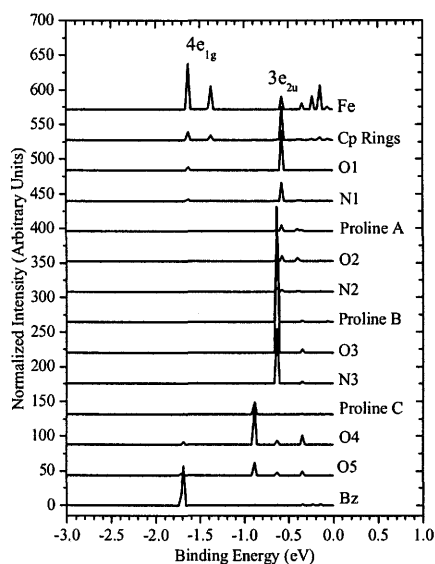


Figure 11.7. The component-resolved unoccupied DOS of Fc-Pro₃-OBz, as calculated using StoBe. Plots are arranged according to their location in the molecule, and a vertical offset is added for clarity.

The major differences between the two calculated densities of states are seen when comparing the benzyl esters and their adjacent proline residues. The most drastic difference is that the LUMO in Fc-Pro₃-OBz is located on the benzyl ester, rather than the ferrocene. The site-resolved DOS of the ester is shown in Figure 11.8, where it is apparent that the main peak is actually composed of two non-degenerate orbitals. The DOS contribution to sites C28 and C31 is mostly from the lower-energy (-1.70 eV) orbital, while the other sites have a more significant contribution from the higher-energy (-1.68 eV) orbital.

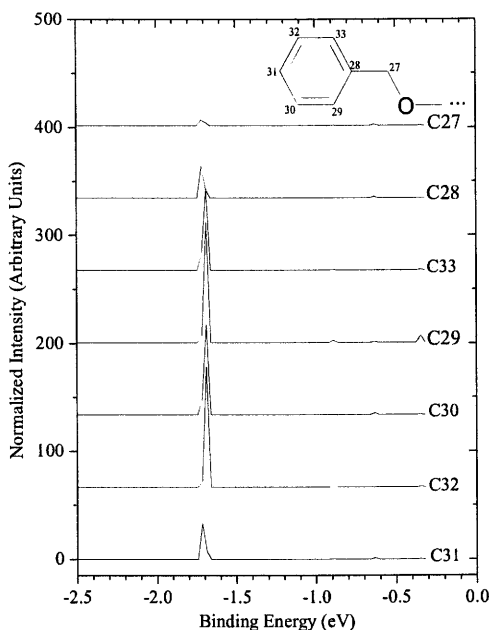


Figure 11.8. The unoccupied DOS of the benzyl ester sites in Fc-Pro₃-OBz as calculated using StoBe. The position of each site in the molecule is labeled on the inset, and a vertical offset is added.

In order to better understand the form of the LUMO and LUMO +1 orbitals in Fc-Pro₃-OBz, they were modeled using Spartan. Both orbitals are shown in Figure 11.9, and there is a strong agreement between the diagrams and the results of the StoBe calculations. The form of these Fc-Pro₃-OBz orbitals can best be understood by comparing them to the orbitals of a substituted benzene ring. Spartan was used to calculate the electronic structure of toluene (C₆H₅-CH₃, a benzene ring with a CH₃ substituent), and the two lowest unoccupied molecular orbitals of that structure closely resemble those in Figure 11.9. The toluene orbitals are shown in Appendix E.

The similarity between the Fc-Pro₃-OBz orbitals and those of toluene suggest that the benzyl ester in the former molecule is isolated from the rest of the system and that the major influence on its electronic structure is the substituent C atom. In contrast, the benzyl ester in Fc-Pro₂-OBz is in a higher-energy state, with the first benzene orbitals at the LUMO +2, LUMO +3, and LUMO +4 locations. The difference in electronic structure consists of more than a shift to higher energy, however. The LUMO +3 and LUMO +4 orbitals seem to be somewhat analogous to the toluene orbitals, although

there are small differences in the shapes of the orbitals. The general character of the orbitals is in agreement. Conversely, the lowest-energy unoccupied MO of Fc-Pro₂-OBz does not resemble any of the toluene orbitals; the closest analogue is the Fc-Pro₃-OBz LUMO +4 orbital. The results of the two DFT programs disagree as to the spatial extent of this orbital; as was mentioned previously, the more rigorous StoBe calculations will be assumed to be correct in this case.

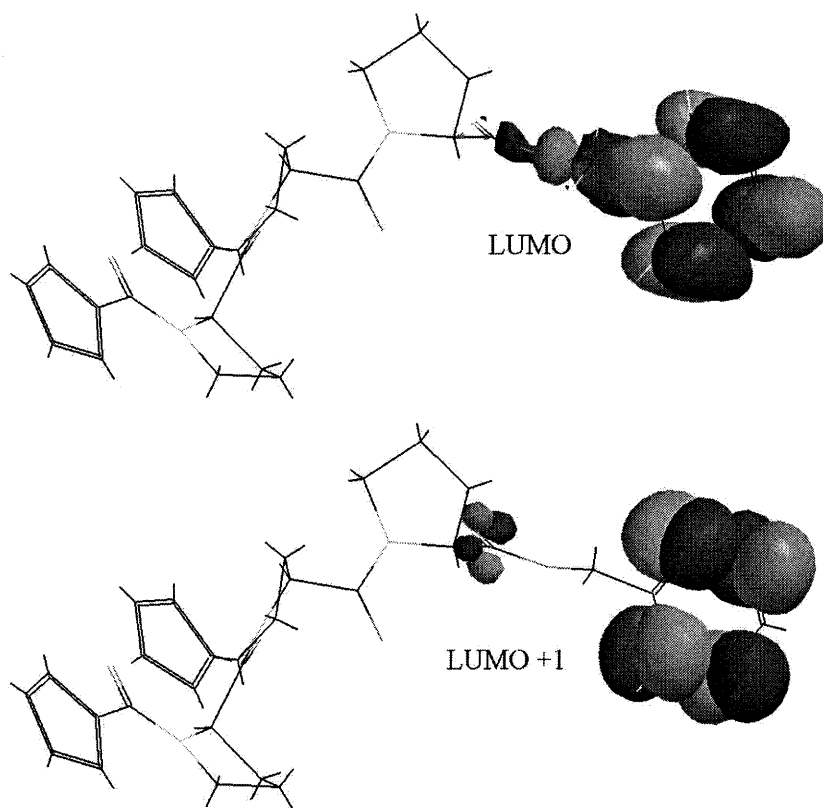


Figure 11.9. The LUMO and LUMO+1 orbitals of Fc-Pro₃-OBz calculated using Spartan.

The two orbitals that are being compared can be seen at -1.49 eV in Figure 11.3 (the Fc-Pro₂-OBz LUMO +2) and at -0.89 eV in Figure 11.7 (the Fc-Pro₃-OBz LUMO +4 orbital). Note that the contribution to the latter orbital from the benzene, as well as the sites N3 and O3 is very small; the vertical scale of Figure 11.7 does not allow these contributions to be seen. The benzene contribution is more visible in Figure 11.9,

where it is apparent that the orbital has contributions from C29, C31, and C32 only. The Spartan calculation also shows minor contributions from three carbon sites, although only C29 is common between the two.

The plots suggest that the two orbitals extend into the peptide structure in much the same way, with contributions from the two adjacent proline residues in both cases. The Spartan plots of the orbitals are very similar to each other, especially in the regions with the largest contributions. Unfortunately, due to the complexity of the orbitals, a two-dimensional rendering such as those shown in Figure 11.6 would convey very little information, and so a written description of the important properties must suffice. Both orbitals have a generally π^* -like character throughout and have significant contributions from the carbonyl group that is adjacent to the benzyl ester.

Before progressing further, it is important to eliminate one possible explanation for the differences in electronic structure. While it is true that the bonds in the benzene ring of Fc-Pro₂-OBz are longer than those of either toluene or Fc-Pro₃-OBz, possibly due to intermolecular interaction, this difference is not great enough (on the order of 0.01 Å) to significantly affect the final electronic structure. In order to quickly confirm this assumption, Spartan was used to calculate the electronic structure of a toluene molecule with bond lengths identical to the Fc-Pro₂-OBz benzene ring; the orbitals that were produced were indistinguishable from those produced by the initial toluene calculation.

Having thus eliminated the possibility that the observed changes in the orbitals are the result of intermolecular effects, it is apparent that the electronic structure of the electron-accepting portion of the Fc-Pro_x-OBz samples is affected by its distance from the electron-donating ferrocene molecule. This conclusion is further supported by the Spartan simulation of the electronic structure of Fc-Pro₄-OBz, which also places the LUMO and LUMO +1 orbitals on the benzyl ester, rather than on the ferrocene. As it is a rather large molecule, the results of the Spartan simulation could not be confirmed using StoBe; convergence of the SCF calculations could not be achieved.

The absorption spectrum of a substance is, as was discussed earlier, closely related to its unoccupied density of states. Comparing the results of the two types of calculations for Fc-Pro₂-OBz suggests that the molecular orbitals undergo a major reorganization under the influence of the core hole. This effect suggests that any influence of the extended structure attached to the benzyl ester is overwhelmed when the local environment is perturbed by the appearance of a core hole. In support of this observation, it should be noted that the calculated and experimental XAS spectra bear a strong resemblance to the unoccupied density of states of the benzyl ester in Fc-Pro₃-OBz, which was assumed to have little influence from the ferrocene. Significantly, the term values of the lowest-energy Fc-Pro₂-OBz XAS features are slightly higher than those associated with excitations into the 4e_{1g}' orbital associated with the ferrocene. The difference in term values suggest that the LUMO of the transition state of Fc-Pro₂-OBz is located on the benzene rings, as it is in the larger peptidic materials.

12. SUMMARY AND CONCLUSIONS

A combined experimental and theoretical analysis of the electronic structures of a series of modified helical peptides has been presented. Soft X-ray absorption and emission measurements were performed at Beamlines 6.3.2 and 8.0.1 at the ALS synchrotron at Lawrence Berkeley National Lab. This study represents the first such examination of peptides that have been modified by the attachment of electroactive molecules. All previous studies have been concerned with the analysis of smaller, unmodified peptides (≤ 3 amino acid residues) or monomers. A summary of the samples and edges that were examined in previous studies is tabulated in Appendix F.

The density functional theory program StoBe was used to simulate the XAS spectra of Fc-Pro₂-OBz, as well as the ground state electronic structures of Fc-Pro₂-OBz and Fc-Pro₃-OBz. Excellent agreement with the measured spectra was found, and a great deal of information was inferred when the two types of data are compared. The calculated spectra were analyzed site-specifically in order to better understand the various contributions to the overall spectra. This study is one of the first known examples of this type of analysis,⁹⁴ and provides an indication of the power of this technique. The analysis of the carbon 1s XAS spectra is especially aided by this site-specific analysis, due to the large number of contributing transitions.

The following sections will briefly describe the findings of each portion of the analysis.

12.1. Conclusions from the Experimental XAS Spectra

High-quality XAS spectra of all elements in the molecules; C, N, O, and Fe, were presented in Section 9. The C 1s XAS spectra (Section 9.1.1) reveal that the degeneracy of the ferrocene 3e_{2u} orbitals is broken due to the presence of the

substituent. Previous studies suggested that this was likely the case, but were unable to find evidence that the splitting had occurred.^{57,72} Also, the feature associated with the amino acid carbonyl π^* orbitals was shown to increase in intensity as a function of the number of residues in the peptide.

The individual contributions of the carbonyl sites and the benzyl ester oxygen atom were identified in the O 1s XAS spectra (Section 9.2.1). The spectra were dominated by the transitions into the carbonyl π^* orbitals, with the features evolving in much the same as was observed in the C 1s XAS spectra. Both the C 1s and O 1s XAS spectra confirmed that the transition energy of the carbonyl π^* resonance peak is strongly, and to an extent predictably, influenced by the electronegativity of the surrounding environment, less so in the oxygen spectra than in the carbon spectra.⁷⁶

A distinct pre-edge feature was seen in all N 1s XAS spectra (Section 9.3.1), suggesting that the single-bonded nitrogen atoms gained a large degree of π^* character as a result of the overlapping of their 2p orbitals with the carbonyl π^* orbitals.⁵⁸ Although all nitrogen atoms in these molecules occupied nearly equivalent nearest-neighbour environments, this prominent feature was found at a lower energy in the spectrum of Fc-Pro₁-OBz than in the spectra of the larger molecules. This shift in energy showed that the nitrogen character of the nitrogen orbitals is dependent on the long-range structure of the molecule. The main peak in the N 1s XAS spectrum of Fc-Pro₁-OBz was associated with the N-terminus of the peptide, which was influenced by its proximity to the ferrocene. It was observed that the spectra of the larger peptides were dominated by a higher-energy peak that was characteristic of the peptide bond, although the lower-energy N-terminus feature appeared as a shoulder.

Examination of the Fe 2p XAS spectra (Section 9.4) supported the general conclusions of previous studies, namely that the electronic structure of ferrocene is affected only by the identity of the immediate substituent, and not by the size or identity of the extended structure to which it is attached.^{57,73,79,80} All of the samples, having a carbonyl group attached to the Cp rings, had similar spectra. The only noticeable difference was

caused by the decrease in the concentration of Fe that occurs as larger peptides are attached.

12.2. Conclusions from the Calculated XAS Spectra

Further analysis of the Fe electronic structure was made possible by the StoBe simulations of the 2p XAS spectra. Although significant problems were encountered with these calculations, some important conclusions were drawn from the results. The calculations confirmed the origin of the $4e_{1g}$ and $3e_{2u}$ orbitals seen in the C 1s XAS spectra. In addition, the transitions that contribute to the prominent feature seen at 711.4 eV in the measured spectra were found to have term values that closely correspond to those of the C-H σ^* transitions in the C 1s XAS spectra. This observation led to the reassignment of this peak, which had previously been assumed to be associated with a $3e_{2u}$ final state.^{57,79}

Confirmation of the analyses of the measured O 1s and N 1s XAS spectra was achieved by site-specific analysis of their calculated spectra (Sections 9.2.2 and 9.3.2 respectively). The relative, and in the case of the N 1s XAS, absolute, positions of the calculated peaks corresponded closely with the features seen in the measured spectra. Simulating the spectra using StoBe allowed the individual contributions to some of the broad features in the measured spectra to be examined.

The splitting of the $4e_{1g}$ -like and $3e_{2u}$ -like orbitals of the ferrocene was more easily observed in the calculated C 1s XAS spectra than in the measured spectra. Site-specific analysis allowed the orbitals to be characterized. The two non-degenerate $4e_{1g}$ -like orbitals were seen to have contributions from both the substituted and the unsubstituted Cp rings. It was proposed that this dual contribution was linked to the origin of the $4e_{1g}$ orbitals, which are closely related to the Fe 3d orbitals. If the substituent causes a significant change in the characteristics of these orbitals, this change would likely be reflected in the C 1s spectra of both the substituted and unsubstituted Cp sites.

Contrarily, the spectral contributions of the two $3e_{2u}$ -like final states were strongly associated with a particular Cp ring. Peaks associated with the lower-energy transition, associated with the orbital denoted by $3e_{2u}'$, were seen mostly in the spectra of the sites on the substituted ring, while the transitions into the higher-energy orbital, $3e_{2u}''$, were largely restricted to the unsubstituted ring. This difference in behaviour, as compared to the $4e_{1g}$ -like orbitals, was attributed to the association of the $3e_{2u}$ orbitals with the Cp π^* orbitals. The effect of the substituent would be felt more strongly by the ring to which it is attached, compared to the unsubstituted Cp ring.

Transitions into the $3e_{2u}'$ orbital were not confined to the ferrocene, but were present in many of the spectra of the extended peptide structure. This was the first evidence that the $3e_{2u}'$ orbital represented a major contribution to a delocalized orbital that could play an important role in electron transfer along the peptide. Further corroboration of this theory was provided by the ground state density of states calculations.

12.3. Conclusions from DOS Calculations

Insight into the unperturbed electronic structure of Fc-Pro₂-OBz and Fc-Pro₃-OBz is provided by the StoBe DOS calculations (Section 11). The analysis of these calculations confirmed many of the conclusions that were drawn from the XAS spectra, particularly those regarding the $3e_{2u}$ -like orbitals. The DOS calculations may also have provided an explanation of the change in the electron transfer characteristics of the peptide upon addition of a third proline residue. Like the calculated XAS spectra, the large part of the analysis of the DOS calculations was performed site-specifically.

The appropriateness of reassigning the 711.4 eV Fe 2p XAS feature was confirmed by the DOS calculations. Symmetry-resolved DOS showed that the orbitals associated with the final states of these transitions have a primarily *s*-like contribution, rather than the *d*-like final state that would be characteristic of a $3e_{2u}$ -like orbital. The carbon

DOS confirmed that the orbitals in question are involved in the C-H bonding of the Cp rings.

The two non-degenerate $4e_{1g}$ -like orbitals were shown to have approximately equal contributions from the ferrocene C sites, in agreement with the analysis of the C 1s XAS spectra. It was seen that neither orbital extends very far from the ferrocene, as opposed to the $3e_{2u}$ -like orbitals, which are part of a highly delocalized network. These orbitals were seen to have similar character in both Fc-Pro₂-OBz and Fc-Pro₃-OBz. The $3e_{2u}$ -like orbitals extend well into the peptide structure, having DOS contributions from all residues, including the nitrogen and oxygen sites. This electronic structure strongly suggests that these orbitals may play a key role in electron transfer along the peptide. If a path for the electrons can be provided by a conduction orbital, it removes the need for a hopping or tunneling explanation for electron transfer.

The motivation for this study of modified peptides has its basis in the unusual reduction-oxidation behaviour that was observed in the Fc-Pro_x-OBz series using cyclic voltammetry measurements.⁴ As was discussed earlier (Section 6), the addition of the third proline residue to the peptide causes a significant decrease in the potential that is required to remove an electron from the ferrocene and place it on the benzyl ester. It was theorized that if this unusual behaviour could be understood, insight into the mechanisms behind the transfer of electrons through peptides and other organic materials could be obtained. Although the $3e_{2u}$ -based orbital that was discovered in this study seems to provide a likely explanation of the general transfer characteristics, it does not explain the comparative ease with which the Fc-Pro₃-OBz molecule undergoes the redox reaction. However, a possible explanation of this phenomenon was suggested by comparison of the calculated DOS of Fc-Pro₂-OBz and Fc-Pro₃-OBz.

The DOS of these two molecules showed that the unoccupied orbitals of the electron acceptor, the benzyl ester, were drastically affected by the increase in the size of the peptide. In the plots of the Fc-Pro₃-OBz DOS, the two lowest-energy orbitals of the benzyl ester were found at slightly lower energies than the $4e_{1g}$ -like orbitals. In this

case, the benzene orbitals represented the LUMO and LUMO+1 orbitals of the molecule. This was not the case in the Fc-Pro₂-OBz DOS, where the benzyl ester orbitals were found at much higher energy; the analogues of the previously discussed orbitals were found at the LUMO+3 and LUMO+4 locations. It seems likely that the transfer of an electron will be easier to achieve if the energy of the accepting orbital is low- in the case of Fc-Pro₃-OBz, the transfer will proceed 'downhill,' in contrast to the case of Fc-Pro₂-OBz

The orbitals in the benzyl ester of Fc-Pro₃-OBz closely resembled the ground state of a substituted benzene ring that was not attached to an extended structure. This observation suggests that the extended peptide structure, and likely the electroactive ferrocene molecule, had a significant effect on the benzyl ester. Previous examinations of the results of cyclic voltammetry measurements suggested that the ferrocene could 'sense' the addition of the third residue in the peptide chain.⁴ The current study suggests that this is not the case, rather it appears that the benzyl ester can sense the presence of the distant ferrocene until the third proline residue is added and the distance becomes too great.

12.4. Summary

The combination of experimental soft X-ray spectroscopy with modern DFT techniques has proven to be a powerful one. This study has provided one of the most ambitious analyses of large organic molecules ever to employ these techniques. A great wealth of information about the peptidic materials under examination was accrued. It is hoped that this study will increase the understanding of the electronic properties of organic materials in general.

REFERENCES

1. I. Bertini, *Bioinorganic chemistry* (University Science Books, Mill Valley, Calif., 1994).
2. H. Kraatz, J. Lusztyk, and G. Enright, *INORGANIC CHEMISTRY* **36**, 2400-2405 (1997).
3. L. Lin, A. Berces, and H. Kraatz, *JOURNAL OF ORGANOMETALLIC CHEMISTRY* **556**, 11-20 (1998).
4. H. Kraatz, D. Leek, A. Houmam, G. Enright, J. Lusztyk, and D. Wayner, *JOURNAL OF ORGANOMETALLIC CHEMISTRY* **589**, 38-49 (1999).
5. P. Saweczko and H. Kraatz, *COORDINATION CHEMISTRY REVIEWS* **192**, 185-198 (1999).
6. Y. Xu, P. Saweczko, and H. Kraatz, *JOURNAL OF ORGANOMETALLIC CHEMISTRY* **637**, 335-342 (2001).
7. H. Kraatz and M. Galka, *PROBING OF PROTEINS BY METAL IONS AND THEIR LOW-MOLECULAR-WEIGHT COMPLEXES* **38**, 385-409 (2001).
8. D. Attwood, *Soft x-rays and extreme ultraviolet radiation* (Cambridge, New York, 1999).
9. J. Jia, T. Callcott, J. Yurkas, A. Ellis, F. Himpsel, M. Samant, J. Stöhr, D. Ederer, J. Carlisle, E. Hudson, L. Terminello, D. Shuh, and R. Perera, *REVIEW OF SCIENTIFIC INSTRUMENTS* **66**, 1394-1397 (1995).
10. www.als.lbl.gov, *High Resolution and Flux for Materials and Surface Science: Beamline 8.0.1* (2005).
11. www.als.lbl.gov, *Soft X-Ray Fluorescence (SXF) Spectrometer: Beamline 8.0.1* (2005).
12. www.cxro.lbl.gov, *Calibration and Standards Beamline 6.3.2 at the ALS* (2005).
13. G. Mahan, *PHYSICAL REVIEW B* **21**, 1421-1431 (1980).
14. M. Krause, *JOURNAL OF PHYSICAL AND CHEMICAL REFERENCE DATA* **8**, 307-327 (1979).

15. *X-ray data booklet; Vol. 1*, edited by A. C. Thompson and D. Vaughan (Lawrence Berkeley National Laboratory, Berkeley, 2001).
16. [www.cxro.lbl.gov, Optical_Constants/Atten2.Html](http://www.cxro.lbl.gov/Optical_Constants/Atten2.Html), (2005).
17. B. Henke, E. Gullikson, and J. Davis, *ATOMIC DATA AND NUCLEAR DATA TABLES* **54**, 181-342 (1993).
18. T. Calcott, in *Vacuum ultraviolet spectroscopy ii; Vol. 32*, edited by J. A. R. Samson and D. L. Ederer (Academic Press, San Diego, 1998), p. xv, 307 p.
19. C. J. Cramer, *Essentials of computational chemistry: Theories and models* (J. Wiley, West Sussex, England; New York, 2002).
20. P. Hohenberg and W. Kohn, *PHYSICAL REVIEW* **136**, B864 (1964).
21. W. Kohn and L. Sham, *PHYSICAL REVIEW* **140**, A1133 (1965).
22. S. Chretien and D. R. Salahub, in *Atomic clusters and nanoparticles*, edited by C. G. E. Al. (New York, 2001), p. 105-160.
23. A. P. French and E. F. Taylor, *An introduction to quantum physics*, 1st ed. (Norton, New York, 1978).
24. F. Schwabl, *Advanced quantum mechanics* (Springer, Berlin; New York, 1999).
25. J. C. Slater, *PHYSICAL REVIEW* **81**, 385-390 (1951).
26. J. Perdew and Y. Wang, *PHYSICAL REVIEW B* **33**, 8800-8802 (1986).
27. V. Sahni, J. Gruenebaum, and J. Perdew, *PHYSICAL REVIEW B* **26**, 4371-4377 (1982).
28. J. Perdew, *PHYSICAL REVIEW LETTERS* **55**, 1665-1668 (1985).
29. J. Perdew, *PHYSICAL REVIEW B* **33**, 8822-8824 (1986).
30. A. Becke, *PHYSICAL REVIEW A* **38**, 3098-3100 (1988).
31. K. Hermann, L. G. M. Pettersson, M. E. Casida, C. Daul, A. Goursot, A. Koester, E. Proynov, A. St-Amant, D. R. Salahub., and H. D. Contributing Authors: V. Carravetta, N. Godbout, J. Guan, C. Jamorski, M. Leboeuf, V. Malkin, O. Malkina, M. Nyberg, L. Pedocchi, F. Sim, L. Triguero, and A. Vela, StoBe Software, *StoBe-demon version 2.1*, (2005).
32. D. R. Salahub, M. E. Castro, and E. I. Proynov, in *Relativistic and electron correlation effects in molecules and solids; Vol. 318*, edited by G. L. Malli (Plenum Press, New York, 1994), p. 411-445.

33. S. Huzinaga and J. Andzelm, *Gaussian basis sets for molecular calculations* (Elsevier, Amsterdam; New York, 1984).
34. B. Dunlap, J. Connolly, and J. Sabin, *JOURNAL OF CHEMICAL PHYSICS* **71**, 3396-3402 (1979).
35. S. J. Leon, *Linear algebra with applications*, 6th ed. (Prentice Hall, Upper Saddle River, N.J., 1998).
36. L. Triguero, L. Pettersson, and H. Agren, *JOURNAL OF PHYSICAL CHEMISTRY A* **102**, 10599-10607 (1998).
37. C. Kolczewski, R. Püttner, O. Plashkevych, H. Agren, V. Staemmler, M. Martins, G. Snell, A. Schlachter, M. Sant'anna, G. Kaindl, and L. Pettersson, *JOURNAL OF CHEMICAL PHYSICS* **115**, 6426-6437 (2001).
38. K. Hermann and L. Pettersson, *Documentation for StoBe2005 (version 2.1)* (2005).
39. J. Stöhr, *NEXAFS Spectroscopy* (Springer-Verlag, Berlin, 1996).
40. M. Nyberg, M. Odellius, A. Nilsson, and L. Pettersson, *JOURNAL OF CHEMICAL PHYSICS* **119**, 12577-12585 (2003).
41. W. Kutzelnigg, U. Fleischer, and M. Shindler, in *NMR-Basic principles and progress; Vol. 23* (Springer-Verlag, New York, 1990), p. 165.
42. L. Pettersson, Personal Communication, (2004).
43. F. Appoh, T. Sutherland, and H. Kraatz, *JOURNAL OF ORGANOMETALLIC CHEMISTRY* **689**, 4669-4677 (2004).
44. I. Bediako-Amoa, T. Sutherland, C. Li, R. Silerova, and H. Kraatz, *JOURNAL OF PHYSICAL CHEMISTRY B* **108**, 704-714 (2004).
45. M. Galka and H. Kraatz, *CHEMPHYSICHEM* **3**, 356-+ (2002).
46. I. Bediako-Amoa, R. Silerova, and H. Kraatz, *CHEMICAL COMMUNICATIONS*, 2430-2431 (2002).
47. H. Kraatz, *MACROMOLECULAR SYMPOSIA* **196**, 39-44 (2003).
48. A. Moewes, J. Macnaughton, R. Wilks, J. Lee, S. Wettig, H. Kraatz, and E. Kurmaev, *JOURNAL OF ELECTRON SPECTROSCOPY AND RELATED PHENOMENA* **137-40**, 817-822 (2004).
49. M. Baker, H. Kraatz, and J. Quail, *NEW JOURNAL OF CHEMISTRY* **25**, 427-433 (2001).

50. L. G. Farrugia, *Ortep-3 for windows*, (1997).
51. A. Augustsson, M. Herstedt, J. Guo, K. Edstrom, G. Zhuang, P. Ross, J. Rubensson, and J. Nordgren, *PHYSICAL CHEMISTRY CHEMICAL PHYSICS* **6**, 4185-4189 (2004).
52. J. Carlisle, E. Shirley, E. Hudson, L. Terminello, T. Callcott, J. Jia, D. Ederer, R. Perera, and F. Himpsel, *PHYSICAL REVIEW LETTERS* **74**, 1234-1237 (1995).
53. V. Fomichev and M. Rumsh, *JOURNAL OF PHYSICS AND CHEMISTRY OF SOLIDS* **29**, 1015-& (1968).
54. J. Denlinger, *Title* (unpublished),
55. V. Lusvardi, M. Barteau, J. Chen, J. Eng, B. Fruhberger, and A. Teplyakov, *SURFACE SCIENCE* **397**, 237-250 (1998).
56. J. Bearden, *REVIEWS OF MODERN PHYSICS* **39**, 78-& (1967).
57. A. Wen, E. Ruhl, and A. Hitchcock, *ORGANOMETALLICS* **11**, 2559-2569 (1992).
58. J. Boese, A. Osanna, C. Jacobsen, and J. Kirz, *JOURNAL OF ELECTRON SPECTROSCOPY AND RELATED PHENOMENA* **85**, 9-15 (1997).
59. Y. Zubavichus, M. Zharnikov, A. Schaporenko, and M. Grunze, *JOURNAL OF ELECTRON SPECTROSCOPY AND RELATED PHENOMENA* **134**, 25-33 (2004).
60. G. Cooper, M. Gordon, D. Tulumello, C. Turci, K. Kaznatcheev, and A. Hitchcock, *JOURNAL OF ELECTRON SPECTROSCOPY AND RELATED PHENOMENA* **137-40**, 795-799 (2004).
61. V. Carravetta, O. Plashkevych, and H. Agren, *JOURNAL OF CHEMICAL PHYSICS* **109**, 1456-1464 (1998).
62. L. Yang, O. Plashkevych, O. Vahtras, V. Carravetta, and H. Agren, *JOURNAL OF SYNCHROTRON RADIATION* **6**, 708-710 (1999).
63. K. Kaznachejev, A. Osanna, C. Jacobsen, O. Plashkevych, O. Vahtras, and H. Agren, *JOURNAL OF PHYSICAL CHEMISTRY A* **106**, 3153-3168 (2002).
64. J. Hasselström, O. Karis, M. Weinelt, N. Wassdahl, A. Nilsson, M. Nyberg, L. Pettersson, M. Samant, and J. Stöhr, *SURFACE SCIENCE* **407**, 221-236 (1998).

65. M. Nyberg, J. Hasselström, O. Karis, N. Wassdahl, M. Weinelt, A. Nilsson, and L. Pettersson, *JOURNAL OF CHEMICAL PHYSICS* **112**, 5420-5427 (2000).
66. M. Tanaka, K. Nakagawa, T. Koketsu, A. Agui, and A. Yokoya, *JOURNAL OF SYNCHROTRON RADIATION* **8**, 1009-1011 (2001).
67. M. Gordon, G. Cooper, C. Morin, T. Araki, C. Turci, K. Kaznatcheev, and A. Hitchcock, *JOURNAL OF PHYSICAL CHEMISTRY A* **107**, 6144-6159 (2003).
68. B. Messer, C. Cappa, J. Smith, K. Wilson, M. Gilles, R. Cohen, and R. Saykally, *JOURNAL OF PHYSICAL CHEMISTRY B* **109**, 5375-5382 (2005).
69. Y. Zubavichus, O. Fuchs, L. Weinhardt, C. Heske, E. Umbach, J. Denlinger, and M. Grunze, *RADIATION RESEARCH* **161**, 346-358 (2004).
70. Y. Zubavichus, M. Zharnikov, A. Shaporenko, O. Fuchs, L. Weinhardt, C. Heske, E. Umbach, J. Denlinger, and M. Grunze, *JOURNAL OF PHYSICAL CHEMISTRY A* **108**, 4557-4565 (2004).
71. E. Ruhl, C. Heinzl, H. Baumgartel, and A. Hitchcock, *CHEMICAL PHYSICS* **169**, 243-257 (1993).
72. E. Ruhl and A. Hitchcock, *JOURNAL OF THE AMERICAN CHEMICAL SOCIETY* **111**, 5069-5075 (1989).
73. A. Hitchcock, A. Wen, and E. Ruhl, *CHEMICAL PHYSICS* **147**, 51-63 (1990).
74. A. Hitchcock, P. Fischer, A. Gedanken, and M. Robin, *JOURNAL OF PHYSICAL CHEMISTRY* **91**, 531-540 (1987).
75. A. Hitchcock, S. Urquhart, and E. Rightor, *JOURNAL OF PHYSICAL CHEMISTRY* **96**, 8736-8750 (1992).
76. S. Urquhart and H. Ade, *JOURNAL OF PHYSICAL CHEMISTRY B* **106**, 8531-8538 (2002).
77. R. Püttner, C. Kolczewski, M. Martins, A. Schlachter, G. Snell, M. Sant'anna, J. Viefhaus, K. Hermann, and G. Kaindl, *CHEMICAL PHYSICS LETTERS* **393**, 361-366 (2004).
78. J. Francis and A. Hitchcock, *JOURNAL OF PHYSICAL CHEMISTRY* **96**, 6598-6610 (1992).
79. A. Hitchcock, A. Wen, and E. Ruhl, *JOURNAL OF ELECTRON SPECTROSCOPY AND RELATED PHENOMENA* **51**, 653-660 (1990).

80. P. Dowben, D. Driscoll, R. Tate, and N. Boag, *ORGANOMETALLICS* **7**, 305-308 (1988).
81. F. De Groot, J. Fuggle, B. Thole, and G. Sawatzky, *PHYSICAL REVIEW B* **42**, 5459-5468 (1990).
82. G. Van Der Laan and I. Kirkman, *Journal of Physics: Condensed Matter* **4**, 4189-4204 (1992).
83. A. Nilsson, N. Wassdahl, M. Weinelt, O. Karis, T. Wiell, P. Bennich, J. Hasselström, A. Föhlisch, J. Stöhr, and M. Samant, *APPLIED PHYSICS A-MATERIALS SCIENCE & PROCESSING* **65**, 147-154 (1997).
84. A. Nilsson, J. Hasselström, A. Föhlisch, O. Karis, L. Pettersson, M. Nyberg, and L. Triguero, *JOURNAL OF ELECTRON SPECTROSCOPY AND RELATED PHENOMENA* **110**, 15-39 (2000).
85. J. Hasselstrom, O. Karis, M. Nyberg, L. Pettersson, M. Weinelt, N. Wassdahl, and A. Nilsson, *JOURNAL OF PHYSICAL CHEMISTRY B* **104**, 11480-11483 (2000).
86. L. Pettersson, H. Agren, Y. Luo, and L. Triguero, *SURFACE SCIENCE* **408**, 1-20 (1998).
87. L. Triguero, Y. Luo, L. Pettersson, H. Agren, P. Vaterlein, M. Weinelt, A. Föhlisch, J. Hasselström, O. Karis, and A. Nilsson, *PHYSICAL REVIEW B* **59**, 5189-5200 (1999).
88. L. Triguero, A. Föhlisch, P. Vaterlein, J. Hasselström, M. Weinelt, L. Pettersson, Y. Luo, H. Agren, and A. Nilsson, *JOURNAL OF THE AMERICAN CHEMICAL SOCIETY* **122**, 12310-12316 (2000).
89. J. Nordgren, L. Selander, L. Pettersson, R. Brammer, M. Backstrom, C. Nordling, and H. Agren, *PHYSICA SCRIPTA* **27**, 169-171 (1983).
90. P. Skytt, J. Guo, N. Wassdahl, J. Nordgren, Y. Luo, and H. Agren, *PHYSICAL REVIEW A* **52**, 3572-3576 (1995).
91. H. Agren, Y. Luo, F. Gelmukhanov, J. Guo, P. Skytt, N. Wassdahl, and J. Nordgren, *PHYSICA B* **209**, 105-107 (1995).
92. J. Guo and J. Nordgren, *JOURNAL OF ELECTRON SPECTROSCOPY AND RELATED PHENOMENA* **110**, 105-134 (2000).
93. *Spartan '04*, Wavefunction Inc., (2004).
94. J. Macnaughton, A. Moewes, and E. Kurmaev, *JOURNAL OF PHYSICAL CHEMISTRY B* **109**, 7749-7757 (2005).

APPENDIX A: STOBE INPUT FILES

The StoBe input files for the calculation of the C 1s XAS spectra of the C1 sites in Fc-Pro2-OBz and Fc-COOH are shown below. The header describes which files are to be included and allows a title to be added. Below the header is the list of the x,y,z coordinates of the atoms in the molecule, as well as identifying labels and their atomic number. The coordinates are followed by the description of the parameters used in the calculation, and by the list of the basis sets that are employed in the calculation. The last lines describe the output files.

```
#!/bin/csh -f
ln -s ../Basis/baslib.new6 fort.3
ln -s ../Basis/symbasis.new fort.4
cat >help.inp <</.
title
FcPro2, C1s C1 XAS
nosy
cartesian angstrom
Fe1 -3.63048000 -1.68374000 2.11586000 26.0
O1 -0.07370000 -0.22979000 3.01454000 8.0
O2 -0.15994000 0.78200000 -0.37724000 8.0
O3 1.23218000 4.16065000 -1.81127000 8.0
O4 2.67642000 2.40268000 -1.59726000 8.0
N1 0.09198000 -1.57272000 1.20163000 7.0
N2 1.56675000 1.61825000 0.78370000 7.0
C2 -2.33829000 -3.22839000 2.55797000 4.0
C3 -2.54821000 -1.09806000 3.79537000 4.0
C4 -3.53736000 -3.33000000 3.34867000 4.0
C5 -3.59726000 -2.14752000 4.09577000 4.0
C6 -5.45654000 -0.87287000 1.65064000 4.0
C7 -4.37248000 0.06289000 1.39245000 4.0
C8 -3.56903000 -0.52013000 0.44500000 4.0
C9 -4.08249000 -1.73463000 0.12139000 4.0
C10 -5.19522000 -2.02576000 0.88390000 4.0
C11 -0.55304000 -1.19088000 2.40511000 4.0
C12 3.83289000 0.02184000 -5.52536000 4.0
C13 2.70158000 -0.77620000 -5.39957000 4.0
C14 3.98640000 1.14270000 -4.71733000 4.0
C15 1.72452000 -0.45496000 -4.46359000 4.0
C16 3.00933000 1.46394000 -3.78135000 4.0
C17 1.87904000 0.66548000 -3.65561000 4.0
```

C18	3.20104000	2.72943000	-2.85962000	4.0
C19	1.32138000	2.93577000	0.21446000	4.0
C20	-0.35142000	-2.59742000	0.22678000	4.0
C21	1.63806000	3.29028000	-1.15360000	4.0
C22	0.41291000	-2.19298000	-1.04400000	4.0
C23	1.68326000	-1.63183000	-0.48237000	4.0
C24	0.82663000	0.54175000	0.41017000	4.0
C25	1.16945000	-0.82558000	0.78829000	4.0
C26	2.20814000	3.85196000	1.21557000	4.0
C27	3.31440000	2.87345000	1.57419000	4.0
C28	2.72994000	1.52729000	1.71071000	4.0
C1	-1.74083000	-1.95686000	2.91604000	6.0
H1	-2.33182520	-0.14404562	4.23938881	1.0
H2	-4.43744595	-1.93005066	4.75799160	1.0
H3	4.45386158	-0.09466501	-6.43011015	1.0
H4	2.47814733	-1.52563050	-6.18110913	1.0
H5	-4.21922322	-4.16183451	3.42411129	1.0
H6	4.76963810	1.89878810	-4.93360614	1.0
H7	1.04254177	1.03690942	-3.02751288	1.0
H8	2.69969637	3.60129239	-3.26648947	1.0
H9	4.26190091	2.94161190	-2.76172097	1.0
H10	1.57252849	4.12274663	2.05144223	1.0
H11	-1.92839979	-3.96187589	1.88448127	1.0
H12	3.86594581	3.19352104	2.45680077	1.0
H13	2.33972680	1.28231976	2.69577051	1.0
H14	-6.26541425	-0.71950701	2.35263502	1.0
H15	1.95606812	-0.89466947	1.53481946	1.0
H16	-4.25871071	1.03051281	1.86164551	1.0
H17	3.41753165	0.74172609	1.41529038	1.0
H18	4.07358824	2.89472468	0.79654845	1.0
H19	0.73036725	-0.92252204	-4.55993627	1.0
H20	-1.43190797	-2.57755974	0.14304978	1.0
H21	0.30526564	3.21502140	0.46936554	1.0
H22	-5.79373078	-2.92430570	0.85184490	1.0
H23	-0.06442685	-3.59421737	0.56245373	1.0
H24	2.54522339	4.76285770	0.73387241	1.0
H25	2.37060215	-2.39264816	-0.12604177	1.0
H26	-2.65032794	-0.09467284	0.04999116	1.0
H27	-3.64182608	-2.42343622	-0.59094844	1.0
H28	0.56757868	-3.03420711	-1.71145686	1.0
H29	-0.14282817	-1.43226928	-1.57912307	1.0
H30	2.23791167	-0.99065525	-1.15914317	1.0

end

runtype start

scftype direct

potential nonlocal be88 pd86

grid fine

multiplicity 1

charge 0

maxcycles 700

econvergence 0.000001

dconvergence 0.000001

dmixing mdens 0.06

diis off

orbi 5d

fsym scfocc excited


```

#!/bin/csh -f
ln -s ../../Basis/baslib.new6 fort.3
ln -s ../../Basis/symbasis.new fort.4
cat >help.inp <</.
title
FcCOOH, C1s C1 XAS
nosy
cartesian angstrom
Fe1 -0.21329 0.61060 0.34202 26.0
O1 -0.24764 -2.76720 -1.11032 8.0
O2 1.90025 -2.17636 -1.38382 8.0
C2 1.04224 0.67214 -1.27208 4.0
C3 -1.14081 -0.07976 -1.33590 4.0
C4 -1.15934 1.33715 -1.32532 4.0
C5 0.18728 1.80681 -1.27860 4.0
C6 -1.25315 1.29623 1.96927 4.0
C7 -1.23634 -0.12432 1.96503 4.0
C8 0.11624 -0.55461 1.99338 4.0
C9 0.95080 0.60241 2.01459 4.0
C10 0.09574 1.75718 1.99994 4.0
C11 0.72560 -1.88351 -1.27176 4.0
C1 0.23243 -0.49676 -1.30643 6.0
H1 -2.02893 1.84441 1.95445 1.0
H2 1.89867 0.58616 1.95274 1.0
H3 -2.00069 -0.68949 1.94597 1.0
H4 0.37720 2.66454 2.00926 1.0
H5 0.41436 -1.45701 1.99788 1.0
H6 -1.93729 1.88298 -1.34569 1.0
H7 -1.89893 -0.65099 -1.35889 1.0
H8 0.46317 2.71555 -1.25632 1.0
H9 1.99333 0.69071 -1.24856 1.0
H10 0.08180 -3.53331 -1.01188 1.0
end
runtype start
scftype direct
potential nonlocal be88 pd86
grid fine
multiplicity 1
charge 0
maxcycles 2000
econvergence 0.000001
dconvergence 0.000001
dmixing mdens 0.06
diis off
orbi 5d
fsym scfocc excited
alfa 49
beta 49
sym 1
alfa 49 1 8 0.5
beta 49 0
end
mulliken on
xray xas
remthreshold 1.D-6
end

```

nomolden
shrt
end
A-IRON (5,5;5,5)
A-OXYGEN (5,2;5,2)
A-OXYGEN (5,2;5,2)
A-CARBON (5,2;5,2)
A-HYDROGEN (5,1;5,1)
O-IRON (63321/531*/311+)
O-OXYGEN (7111/411/1*)
O-OXYGEN (7111/411/1*)
O-CARBON(+4) (311/211/1)
O-CARBON iii_iglo
O-HYDROGEN (311/1)
P-CARBON(+4) (3,1:8,0)
P-CARBON(+4) (3,1:8,0)
P-CARBON(+4) (3,1:8,0)
P-CARBON(+4) (3,1:8,0)
P-CARBON(+4) (3,1:8,0)

APPENDIX B: SITE-RESOLVED STOBE C 1S XAS OF FC-PRO₂-OBZ

The calculated StoBe C 1s XAS spectra of Fc-Pro₂-OBz are shown below. Each site is displayed separately, and the plots are grouped according to their location in the molecule.

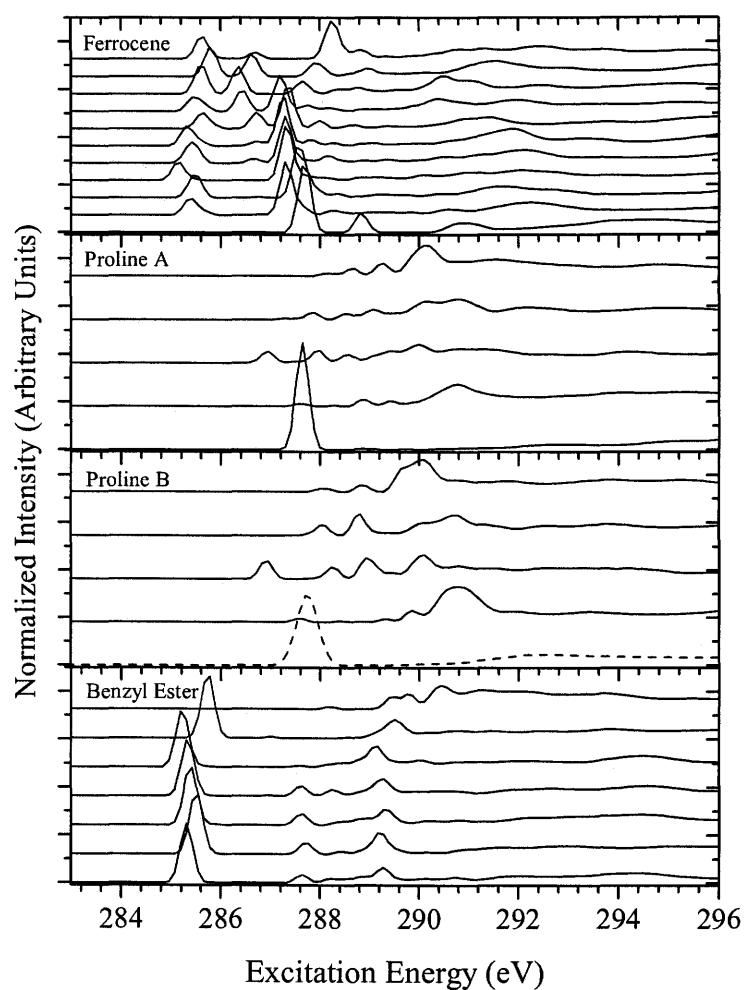


Figure A.1 Site-resolved StoBe C 1s XAS of Fc-Pro₂-OBz

APPENDIX C: TERM VALUES OF STOBE C 1S XAS FEATURES

Table A.1 Site-resolved term values for ferrocene C 1s XAS

Site	Core Level (eV)	Feature (eV)	Term Value (eV)	Assignment
C1	291.19	286.00	3.99	4e _{1g} ''
C4	290.88	285.66	4.02	
C5	291.16	285.89	4.07	
C6	290.90	285.59	4.11	
C8	290.66	285.49	3.97	
C10	290.88	285.66	4.02	
C1	291.19	286.71	3.28	3e _{2u} '
C2	291.21	286.59	3.42	
C3	290.96	286.36	3.40	
C4	290.88	286.36	3.32	
C5	291.16	286.71	3.26	
C6	290.90	286.71	3.00	
C7	290.82	286.71	2.91	
C9	290.91	286.71	3.00	
C4	290.88	287.17	2.50	
C5	291.16	287.41	2.56	
C6	290.90	287.29	3.61	
C7	290.82	287.29	3.53	
C8	290.66	287.29	3.37	
C9	290.91	287.52	3.39	
C10	290.88	287.29	3.59	
C2	291.21	287.87	2.14	Cp' C-H σ*
C3	290.96	287.64	2.12	
C4	290.88	287.76	1.92	
C5	291.16	287.99	1.97	
C6	290.90	288.34	1.36	
C7	290.82	288.22	1.39	
C8	290.66	288.11	1.35	
C9	290.91	288.34	1.37	
C10	290.88	288.22	1.46	

Table A.2 Site-resolved term values for benzene C 1s XAS

Site	Core Level (eV)	Feature (eV)	Term Value (eV)	Assignment ^a
C23	291.32	287.76	2.37	σ -valence+Rydberg
C24	290.89	287.64	2.05	
C25	291.05	287.52	2.32	
C26	291.11	287.64	2.27	
C27	291.17	287.76	2.21	
C28	291.05	287.64	2.21	
C23	291.32	288.57	1.55	σ -valence+Rydberg
C24	290.89	288.11	1.58	
C25	291.05	288.22	1.62	
C26	291.11	288.34	1.57	
C27	291.17	288.46	1.51	
C28	291.05	288.22	1.62	
C23	291.32	289.51	0.62	π^* b _{2g} +Rydberg
C24	290.89	289.16	0.53	
C25	291.05	289.28	0.57	
C26	291.11	289.39	0.52	
C27	291.17	289.28	0.69	
C28	291.05	289.28	0.57	

^aassignments based on those given by Püttner *et al.*¹¹ for benzene

APPENDIX D: FC-PRO₁-OBZ AND FC-COOH C K_α RIXS

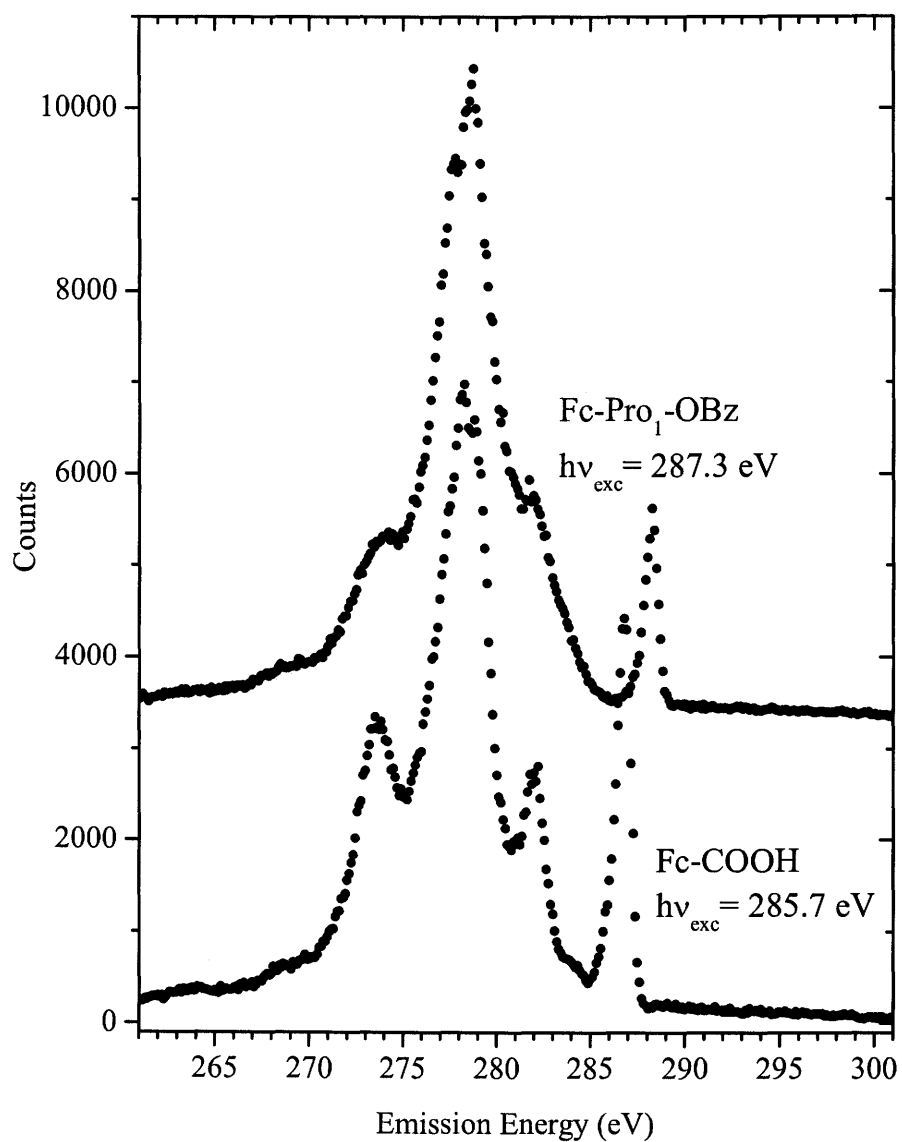


Figure A.2 Comparison of the C K_α RIXS spectra of Fc-Pro₁-OBz and Fc-COOH

APPENDIX E: SPARTAN REPRESENTATIONS OF MOLECULAR ORBITALS

The ferrocene $3e_{2u}$ orbital is shown below, followed by representations of the toluene LUMO and LUMO+1 orbitals. The wire-frame representations of both molecules are included for reference. Single atoms are not shown in these models, but the iron atom in ferrocene is located in the usual location between the Cp rings. It is seen in the figure below that the Fe does not contribute to the $3e_{2u}$ orbital.

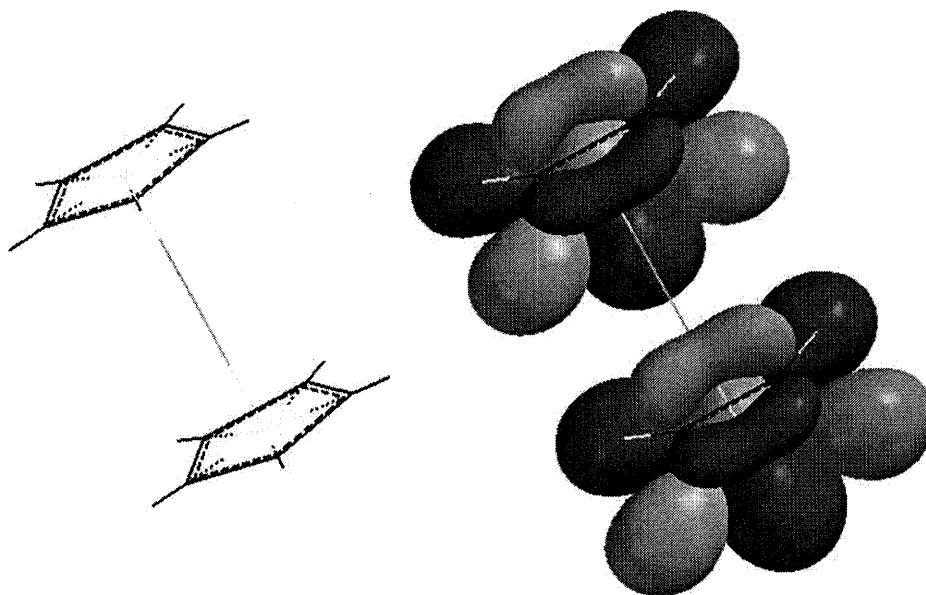


Figure A.3 A $3e_{2u}$ orbital of gaseous ferrocene

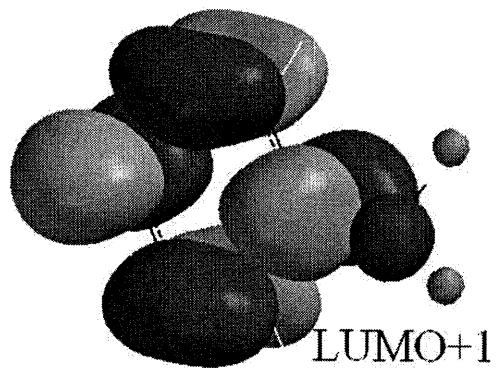
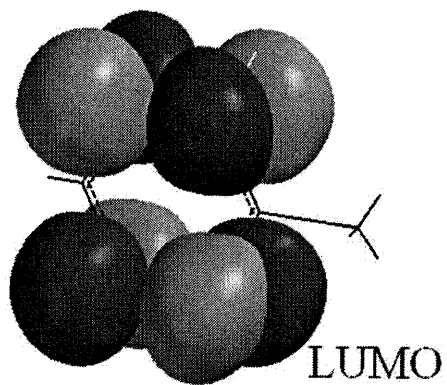
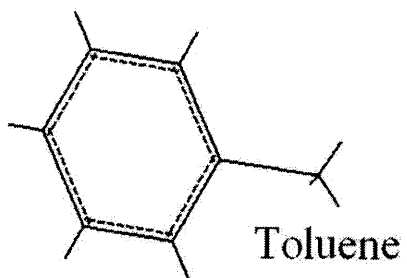


Figure A.4 The LUMO and LUMO+1 orbitals of toluene

APPENDIX F: SUMMARY OF PREVIOUS STUDIES

The table below summarizes the soft X-ray spectroscopy studies of amino acids and peptides that have previously been published. In many cases, the results contained in these papers were used as a basis for comparison in the present study.

Table A.3 Overview of previous XAS and XES studies of amino acids

Author	C 1s	N 1s	O 1s
Boese <i>et al.</i> ⁵⁸	Gly, Phe, His, Tyr, Trp, Arginine		
Carravetta <i>et al.</i> ⁶¹	Gly, Phe, His, Tyr, Trp		
Hasselström <i>et al.</i> ^{64,85}	Gly	Gly	Gly
Yang <i>et al.</i> ⁶²	Gly, Ala, Cys, Ser, Val, Phe, His	Gly, Ala, Cys, Ser, Val, Phe, His	Gly, Ala, Cys, Ser, Val, Phe, His
Nyberg <i>et al.</i> ^{40,65}	Gly	Gly	Gly
Tanaka <i>et al.</i> ⁶⁶			Gly, L- α -Ala, β -Ala, L-Ser, L-Asp, L-Tyr
Kaznacheev <i>et al.</i> ⁶³	Gly, Ala, Val, Leu, Ile, Ser, Thr, Cys, Met, Asp, Glu, Asn, Gln, Lys, Arg, Phe, Trp, Tyr, His		
Gordon <i>et al.</i> ⁶⁷	Gly, Gly ₂ , Gly ₃	Gly, Gly ₂ , Gly ₃	Gly, Gly ₂ , Gly ₃
Cooper <i>et al.</i> ⁶⁰	Gly, Gly ₂ , Ala, Phe	Gly, Gly ₂	Gly, Gly ₂
Zubavichus <i>et al.</i> ^{59,69,70}	(Phe, Tyr) ⁷⁰ (Ala, Ser, Cys, Asn) ⁶⁹ (Gly, Gly ₂ , Gly ₃) ⁵⁹	(Phe, Tyr) ⁷⁰ (Ala, Ser, Cys, Asn) ⁶⁹ (Gly, Gly ₂ , Gly ₃) ⁵⁹	(Phe, Tyr) ⁷⁰ (Ala, Ser, Cys, Asn) ⁶⁹ (Gly, Gly ₂ , Gly ₃) ⁵⁹
Messer <i>et al.</i> ⁶⁸	Gly	Gly	Gly